

Die approbierte Originalversion dieser Dissertation ist an der Hauptbibliothek der Technischen Universität Wien aufgestellt (<http://www.ub.tuwien.ac.at>).

The approved original version of this thesis is available at the main library of the Vienna University of Technology (<http://www.ub.tuwien.ac.at/englweb/>).



TECHNISCHE
UNIVERSITÄT
WIEN
Vienna University of Technology

DISSERTATION

Photon exchange and Decoherence in Neutron Interferometry

ausgeführt zum Zwecke der Erlangung des akademischen Grades eines
Doktors der technischen Wissenschaften unter der Leitung von

em. o. Prof. Dipl.-Ing. Dr. Helmut Rauch

E141 - Atominstitut

eingereicht an der Technischen Universität Wien
Fakultät für Physik

von

Dipl.-Ing. Georg Sulyok

Matrikelnummer 9926007
Jacquingasse 51/7, A-1030 Wien

Wien, am 23. November 2011

Abstract

The general subject of the present work concerns the action of time-dependent, spatially restricted magnetic fields on the wave function of a neutron. Special focus lies on their application in neutron interferometry.

For arbitrary time-periodic fields, the corresponding Schrödinger equation is solved analytically. It is then shown, how the occurring exchange of energy quanta between the neutron and the modes of the magnetic field appears in the temporal modulation of the interference pattern between the original wavefunction and the wavefunction altered by the magnetic field. By Fourier analysis of the time-resolved interference pattern, the transition probabilities for all possible energy transfers are deducible. Experimental results for fields consisting of up to five modes are presented. Extending the theoretical approach by quantizing the magnetic field allows deeper insights on the underlying physical processes. For a coherent field state with a high mean photon number, the results of the calculation with classical fields is reproduced.

By increasing the number of field modes whose relative phases are randomly distributed, one approaches the noise regime which offers the possibility of modelling decoherence in the neutron interferometer. Options and limitations of this modelling procedure are investigated in detail both theoretically and experimentally. Noise sources are applied in one or both interferometer path, and their strength, frequency bandwidth and position to each other is varied. In addition, the influence of increasing spatial separation of the neutron wave packet is examined, since the resulting Schrödinger cat-like states play an important role in decoherence theory.

Kurzfassung

Übergeordneter Gegenstand der vorliegenden Arbeit ist die Wirkung zeitabhängiger, räumlich beschränkter Magnetfelder auf die Wellenfunktion eines Neutrons mit spezieller Berücksichtigung ihrer Anwendung in der Neutronen-Interferometrie.

Für beliebig zeitperiodische Felder wird die entsprechende Schrödingergleichung analytisch gelöst. Es wird gezeigt, wie der dabei auftretende Austausch von Energiequanten zwischen dem Neutron und den Moden des Magnetfeldes anhand der zeitlichen Modulation des Interferenzbildes von ungestörter und vom Magnetfeld veränderter Wellenfunktion bestimmt werden kann. Durch Fourieranalyse des zeitaufgelösten Interferenzmusters lassen sich die Übergangswahrscheinlichkeiten für alle möglichen Energietransfers bestimmen. Messergebnisse für Felder, die bis zu fünf Moden beinhalten, werden präsentiert. Ein erweiterter theoretischer Ansatz, in dem auch das Feld quantisiert wird, gewährt zusätzliche Einblicke in die zugrunde liegenden physikalischen Vorgänge und führt für den kohärenten Feldzustand mit hoher mittlerer Photonenzahl wieder auf die Resultate der Rechnung mit klassischen Feldern.

Wird die Anzahl der im Magnetfeld vorkommenden Frequenzen, deren relative Phasenlage völlig zufällig zueinander ist, weiter erhöht, bewegt man sich in Richtung Rauschfelder. Mit ihnen kann man Dekohärenz im Neutroneninterferometer modellieren. Theoretisch und experimentell wird gezeigt, auf welche Weise diese Modellierung zu verstehen ist, welche Möglichkeiten sie bietet und wo ihre Grenzen liegen. Die Untersuchungen beziehen sich dabei auf Rauschquellen in einem oder beiden Interferometerpfaden, auf die Stärke und den Frequenzbereich der Rauschfelder, ihre Lage zueinander und auf den Einfluss der räumlichen Trennung der Neutronen-Wellenpakete. Letzteres führt auf die sogenannten Schrödingerschen Katzenzustände, die aufgrund ihrer makroskopischen Abmessungen in der Dekohärenztheorie eine besondere Rolle spielen.

Acknowledgements

First of all, I want to thank my supervisor Prof. Helmut Rauch who gave me the opportunity to work as PhD-student in the neutron interferometry group in Vienna. He also allowed me great latitude in developing and pursuing my own ideas and thus making this thesis more than just a contract work for me.

Since I graduated in the purely theoretical field of phenomenological high energy physics, the success of this work would have been impossible without the assistance of my colleagues Jürgen Klepp, Stephan Sponar, Hartmut Lemmel, and Yuji Hasegawa who helped me realizing the experiments at the institute Laue-Langevin in Grenoble. In this context, I also want to mention Matthias Baron whose preliminary works on noise induced dephasing have been essential for my investigations related to this matter.

I also enjoyed numerous, fruitful discussions on theoretical issues throughout my PhD-studies with Katharina Durstberger-Rennhofer and Prof. Johann Summhammer. For the special topics of field quantization and path integrals, I benefitted from the profound skills of Stephan Nimmrichter and Iva Brezinova respectively who I got to know during the Vienna doctoral program on complex quantum systems (CoQuS).

Special thanks go to Prof. Wolfgang Herfort who unhesitatingly provided his mathematical knowledge in solving differential equations, especially for formal details that are not present in the education of a physicists.

Last but not least, I'm indebted to Eva Haberl and Robert Bergmann for their help in overcoming all logistic and bureaucratic barriers whose complexity sometimes seems to exceed the one of quantum theory.

This work was funded by the Vienna doctoral program on complex quantum systems (CoQus) of the Austrian Science Fund (FWF), by the FWF project P18943 and by the PhD program of the Central European Neutron Initiative (CENI).

Contents

1	Introduction	1
2	Energy exchange in a time-dependent magnetic field	5
2.1	Schrödinger equation with a classical field	6
2.1.1	Single mode case	8
2.1.2	Conservation of momentum and energy	12
2.1.3	Generalisation to arbitrary number of field modes	17
2.2	Experimental verification	21
2.2.1	Polarized neutrons	21
2.2.2	Unpolarized neutrons	30
2.3	Experimental results	33
2.3.1	Single mode magnetic field	33
2.3.2	Magnetic field with two modes	43
2.3.3	Magnetic field with three modes	51
2.3.4	Magnetic field with five modes	53
2.4	Quantized field treatment	55
2.5	Phaseshift picture	68
3	Modelling Decoherence with magnetic noise fields	71
3.1	Density matrix formalism in quantum mechanics	71
3.2	Physics of composite systems	72
3.3	Open quantum systems	76
3.4	Density matrix formalism for the IFM	77
3.4.1	Experimental verification	84
3.4.2	Momentum modulation measurements	90
3.4.2.1	Theory	90
3.4.2.2	Experiment	93
4	Finite mode number noise	101
4.1	Noise generation with random phases	101
4.2	Alternative noise generation	110

CONTENTS

5	Conclusion and Outlook	113
A	Error propagation for Discrete Fourier Transformations	117
	Bibliography	123

1

Introduction

Without exaggeration, one can say that, together with the theory of relativity, quantum mechanics has changed the physicist's view of the world at the beginning of the twentieth century. Fundamental concepts of the former, often called "classical" physics, like the rigorous distinction between particles and waves or the principle of complete determinism, had to be abandoned in order to explain the phenomena observed on the microscopic scale. The impact of these scientific findings was not limited to the physicist's community, all nature sciences and even the humanities have been influenced by the development of quantum theory.

Due to the often counter-intuitive predictions of quantum mechanics, at least schematically simple experiments are invaluable to enhance the understanding of quantum mechanical principles. In this context, the Mach-Zehnder interferometer plays a key role.

Originally invented for light [Zeh1891, Mac1892], a collimated beam is split up by a semipermeable mirror in two spatially separated parts that are then reflected again to pass a second semipermeable mirror behind which two detectors are placed. If the beam was split up coherently, i.e. if it takes both paths at the same time and not exclusively one or the other, a continuous change of the optical path length in one beam path causes the intensity to oscillate between the two detectors. The fact that interferometers could also be implemented for massive particles, like electrons [DG1927, MJ1959], neutrons [RTB1974], and recently even atoms and molecules with high mass numbers [Ber1997, ANVA⁺1999] is therefore a beautiful demonstration of their wave properties. The superposition principle, one of the main features of quantum mechanics, is thus also valid for massive particles.

For neutrons, this demonstration was achieved by using monolithic silicon perfect crystals. Since their lattice plane distances are comparable to the wavelength of thermal neutrons, diffraction takes place and the silicon plates can be used as mirrors and beam splitters to build up the interferometer [RP1978]. This

1. INTRODUCTION

technique was used before for X-rays [BH1965] of similar wavelength. Due to the low velocity of thermal neutrons in comparison to the speed of light it is not sufficient to ensure fixed positions of the plates by cutting them out of a single ingot, but also suppression of vibrations and temperature-induced lattice fluctuations is necessary and was first achieved at the TRIGA MARK reactor in Vienna [RTB1974].

Once a stable interferometric setup has been installed, the coherent superposition can be exploited to investigate the quantum behaviour of the involved particle, since every operation in one path of the interferometer has an effect on the interference pattern. Interacting with all four fundamental forces, the neutron can be manipulated by nuclear [RTB1974], magnetic [RZB+1975], electric [COK+1989] or gravitational [COW1975] potentials.

If the interacting potential is time-dependent a change of the neutron's energy is to be expected. If the energy shift is larger than the initial energy width direct observation is possible and has been measured for very cold neutrons impinging on a vibrating surface [FGRG1996] and for neutrons in an oscillating magnetic field that is in resonance with an orthogonally aligned guide field [ABR1981]. For energy exchanges that are not directly observable in the energy spectrum the interferometer's sensitivity to smallest phase shifts can be exploited to indirectly verify the energy transfer. The method was theoretically described [Sum1993] and also experimentally demonstrated [SHK+1995] for thermal neutrons exposed to oscillating magnetic fields.

As mentioned above, the interferometer serves as a tool to demonstrate the coherence of massive particle beams. In some way or the other, for all kinds of particles this demonstration can only be achieved if the setup is sufficiently isolated from its environment. Therefore, by inducing controlled disturbances the loss of coherence can be studied as well, i.e. the interferometer is also a tool to test predictions of decoherence theory [Zur2003, Zur1991]. Decoherence theory exactly deals with the problem of open quantum systems that can no longer be considered isolated. The combined evolution of the system and its environment and the extraction of the system's state from it enables the understanding of physical processes inexplicable for isolated systems. In particular, it is so far the most intuitive and commonly accepted explanation for the transition from the quantum to the classical behaviour of physical objects [JZK+2003, BP2002].

For electrons, this transition could be observed by coupling the electrons to electron and phonon gas inside a semi-conducting plate [SH2007]. In atom interferometry, the beam was exposed to a laser field in order to study loss of coherence [CHL+1995]. For C60-molecules, collision with background gases was used as source for decoherence [HUB+2003].

To model decoherence in the neutron interferometer, one has to use the result of [SAI1990] stating that the loss of coherence can also be described by statisti-

cally distributed phase accumulations of the interfering waves. Via the magnetic dipole interaction described by the Zeeman-Hamiltonian these phases can be attached in the neutron interferometer by applying magnetic noise fields inducing decoherence [SHK⁺2010].

This work deals with the action of time-dependent magnetic fields in the neutron interferometer. It thus covers both the topics of energy/photon exchange and noise induced decoherence. In both cases, the neutron passes a finite region with a time-dependent magnetic field.

In chapter 2.1, we investigate the most simple case, namely a field sinusoidally oscillating in a fixed direction parallel to a guide field. We treat the field classically and solve the corresponding Schrödinger equation analytically.

After investigating the conservation of energy and momentum (section 2.1.2), we generalize to the case of a field arbitrarily oscillating in a fixed direction. That means, the magnetic field signal can now consist of an arbitrary high, countable number of modes with random relative phases.

In sec.2.2, we show how the calculations can be verified in an interferometric setup and then present the measurement results in sec.2.3.

In sec.2.4, we extend our theoretical model by performing quantization of the magnetic field. The Schrödinger equation of the composite quantum system consisting of neutron and magnetic field is analytically solvable. After presenting the general solution, the correspondence to the classical calculation in case of a coherent field state is discussed in detail.

To complete the theoretical approaches, we also show a semiclassical calculation relying on the Glauber eikonal approximation for path integrals (sec.2.5).

In the next chapter, we turn to the issue of modelling decoherence with magnetic fields. Therefore, we recapitulate the main ingredients necessary for understanding decoherence theory. We start with the density matrix formalism in quantum mechanics (sec.3.1), proceed with physics of composite quantum systems (sec.3.2), apply the results to open quantum systems (sec.3.3), and finally arrive at the density matrix formalism for the neutron interferometer (sec.3.4).

Equipped with this theoretical background, we can now investigate the action of magnetic noise fields on the interferogram and interpret the experimental results in the framework of decoherence theory (sec.3.4.1). Noise is applied in one or both interferometer arms, its strength and frequency bandwidth are varied. In sec.3.4.2, the separation width of the neutron wave packets is increased and the effects on the interference pattern that is shifted to momentum space are examined.

In the last chapter (chap.4), we build the bridge between the energy/photon exchange and the decoherence chapters by showing that magnetic fields with a finite number of modes can be used to model a noise signal and therefore cause loss of coherence in the interferometer.

1. INTRODUCTION

In fig.1.1, a simplified outline is depicted.

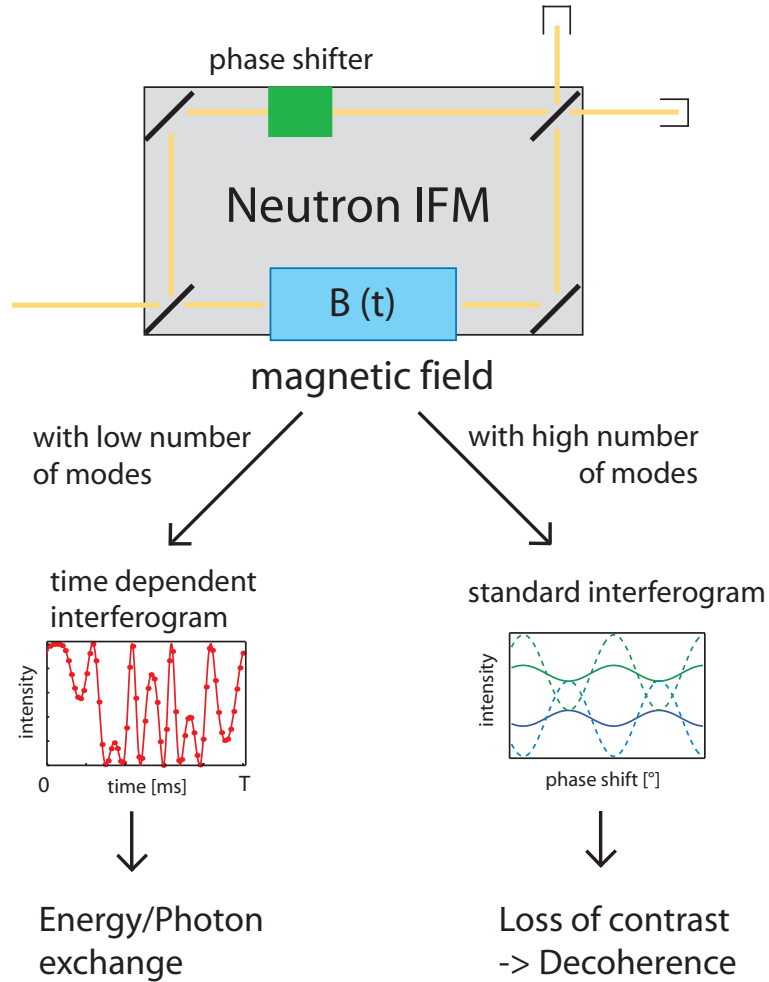


Figure 1.1: Graphical outline of the present work: a spatially finite, time dependent magnetic field is placed in the neutron interferometer (IFM). The effects on the neutron wave function are determined from the interference pattern. For magnetic signals consisting of only a few modes, energy/photon exchange can be derived from Fourier transformation of the time-dependent interferogram. The transition to a high number of modes (i.e. noise) leads to decoherence that can be investigated for varying parameters (signal strength, frequency bandwidth, wave packet separation,...).

2

Energy exchange in a time-dependent magnetic field

If a neutron passes a spatially restricted, time-dependent magnetic field emission and absorption of energy take place. For a sinusoidally varying classical magnetic field the Schrödinger equation has already been solved [Sum1993, HR1982] and the transition amplitudes for various energy transfers have been measured [SHK⁺1995]. For strong magnetic fields, the energy transfer can be directly determined, as done for example in [ABR1981, WBR1988] with high energy resolution spectrometers. For weaker fields, the interferometer's sensitivity to smallest phaseshifts can be exploited to indirectly verify the exchange of energy between the neutron and the magnetic field. In [Sum1993, SHK⁺1995], both cases of an orthogonal and of a parallel arrangement of the static field component and the time-dependent part of the field are discussed. The orthogonal arrangement is closely related to the Jaynes-Cummings model [JC1963] that is very common in quantum optics. The static field defines two different potential energy levels depending on the spin orientation. In case of resonance, the oscillating field leads to a spin flip. A quantum field theoretical treatment of this process shows that the spin flip is accompanied by the exchange of a photon between particle and field. In the case of parallel orientation of the static field component and the oscillating one, no resonant spin flip occurs. Nevertheless, energy exchange between the time dependent field and the neutron happens. The transferred energy leads to a change of the neutron's kinetic energy, i.e. its momentum. This energy transfer can be measured with the help of time-resolved interferometry [SHK⁺1995]. An exact quantum field theoretical treatment of this physical process is still missing.

In this chapter, we want to extend the theoretical and experimental investigations of the parallel field configuration. Therefore, we recapitulate the calculation for the classical single mode field and then generalize by allowing an arbitrary number of frequencies to be contained in the time-dependent field (sec.2.1). In

2. ENERGY EXCHANGE IN A TIME-DEPENDENT MAGNETIC FIELD

section 2.2 we show how the results of the calculations can be verified in an interferometric setup. In section 2.3, we present measurements performed with unpolarized neutrons in an interferometer. In chapter 2.4, the magnetic field is quantized, so that the energy exchange can be properly explained on the fundamental level of exchanged photons.

2.1 Schrödinger equation with a classical field

The quantum mechanical behaviour of spin- $\frac{1}{2}$ particles like the neutron is governed by the Dirac equation [Dir1928], resulting in a four component spinor wave function. For thermal neutrons (velocity $v \approx 2000$ m/s), relativistic effects can be neglected and the Dirac equation is well approximated by the Pauli equation [Pau1927]. Its solutions are two-component spinors, i.e. spin-up and spin-down component of the particle (no anti-particle exists, pair production can practically not happen for such low kinetic energies). In presence of an external magnetic field, the Pauli equation for the uncharged neutron is given by the kinetic term and the Zeeman interaction

$$-\frac{\hbar}{i} \frac{\partial}{\partial t} \psi(x, t) = \left(\frac{p^2}{2m} + \mu \vec{\sigma} \vec{B} \right) \psi(x, t) \quad (2.1)$$

where $\vec{\sigma} = (\sigma_x, \sigma_y, \sigma_z)$ denote the common Pauli matrices generating the $SU(2)$ spin group and μ stands for the neutron's magnetic dipole moment. The Pauli equation can be considered to be the Schrödinger equation for non-relativistic spin- $\frac{1}{2}$ particles.

We focus on the case where the spatially restricted, time-dependent field oscillates parallel to the static component and both are chosen to point in z-direction.

$$\vec{B}(\vec{r}, t) = \begin{pmatrix} 0 \\ 0 \\ B_0 + B(t) \cdot (\Theta(x) - \Theta(x - L)) \end{pmatrix}$$

As indicated by the Heavyside step-function Θ , the time-dependent field is confined to the region $0 \leq x < L$. Since we are interested in the behaviour of the neutron when it passes the time-dependent field, we only consider the x -dependency of the wavefunction¹. The Schrödinger equation for the two-component neutron spinor ψ in this region thus reads

$$-\frac{\hbar}{i} \frac{\partial}{\partial t} \psi(x, t) = \left[-\frac{\hbar^2}{2m} \frac{\partial^2}{\partial x^2} + \begin{pmatrix} \mu(B_0 + B(t)) & 0 \\ 0 & -\mu(B_0 + B(t)) \end{pmatrix} \right] \psi(x, t)$$

¹This can be done formally correct by a solving the differential equation with a product ansatz $\psi(x, y, z, t) = X(x) \cdot Y(y) \cdot Z(z) \cdot T(t)$ and then focussing only on $\psi(x, 0, 0, t) \equiv \psi(x, t)$

2.1 Schrödinger equation with a classical field

It can be seen that the two components of the neutron spinor stay uncoupled and the Schrödinger equation can be solved separately for each of them. This also holds outside the field region where only the static field B_0 is present. The one-dimensional Schrödinger equation for each component of the neutron spinor corresponds to the problem of a time dependent potential barrier (see fig.2.1). It can be solved by determining the wave function in the three different regions

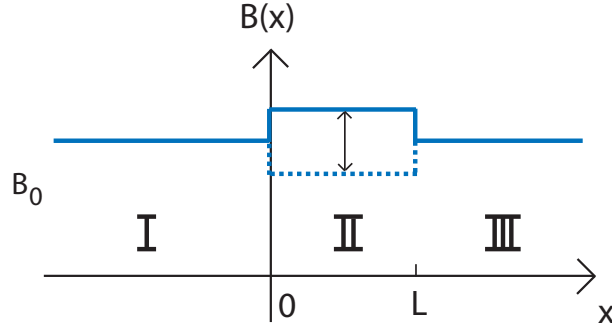


Figure 2.1: Spatial characteristics of the magnetic field potential, in region II the field is varying in time

separately and then applying appropriate matching conditions. The Hamiltonian for each region reads

$$\hat{H}_I = -\frac{\hbar^2}{2m} \frac{\partial^2}{\partial x^2} + \mu\sigma_z B_0, \quad x < 0 \quad (2.2)$$

$$\hat{H}_{II} = -\frac{\hbar^2}{2m} \frac{\partial^2}{\partial x^2} + \mu\sigma_z (B_0 + B(t)), \quad 0 \leq x < L \quad (2.3)$$

$$\hat{H}_{III} = -\frac{\hbar^2}{2m} \frac{\partial^2}{\partial x^2} + \mu\sigma_z B_0, \quad x \geq L \quad (2.4)$$

where σ_z is now just a number taking the values $+1$ (-1) for the spin-up (spin-down) component. In the further, we only perform the calculation for the spin-up component, but still denote it with ψ for simplicity's sake. The result for the down spin component can be obtained by just replacing every μ with $-\mu$. For thermal neutrons, it can be assumed that the kinetic energy of the incoming neutron is much larger than the potentials generated by the magnetic fields ($\hbar^2 k_0^2 / 2m \gg \mu(B_0 + B(t))$) and therefore, reflection can be neglected in region I and the ansatz for the incident plane wave reads

$$\psi_I(x, t) = e^{i\tilde{k}_0 x} e^{-i\omega_0 t}, \quad \tilde{k}_0 = \left(k_0^2 - \frac{2m}{\hbar^2} \mu B_0 \right)^{1/2}, \quad \omega_0 = \frac{\hbar k_0^2}{2m} \quad (2.5)$$

2. ENERGY EXCHANGE IN A TIME-DEPENDENT MAGNETIC FIELD

In region II, a superposition of plane waves has to be combined with a time-dependent phase containing the primitive of $B(t)$ to solve the time-dependent Schrödinger equation (eq.2.3). The general solution reads

$$\psi_{II}(x, t) = e^{-i\frac{\mu}{\hbar} \int B(t') dt'} \int c_{II}(k) e^{i\tilde{k}x} e^{-i\omega(k)t} dk \quad (2.6)$$

with

$$\tilde{k} = \left(k^2 - \frac{2m}{\hbar^2} \mu B_0 \right)^{1/2}, \quad \omega(k) = \frac{\hbar k^2}{2m} \quad (2.7)$$

In region III, the neutron propagates freely (apart from a constant shift due to B_0) and thus, the wave function is given in general by

$$\psi_{III}(x, t) = \int c_{III}(k) e^{i\tilde{k}x} e^{-i\omega(k)t} dk, \quad \tilde{k} = \left(k^2 - \frac{2m}{\hbar^2} \mu B_0 \right)^{1/2}, \quad \omega(k) = \frac{\hbar k^2}{2m} \quad (2.8)$$

These ansatzes, together with the matching conditions at $x = 0$ and $x = L$

$$\psi_I(0, t) = \psi_{II}(0, t) \quad , \quad \psi'_I(0, t) = \psi'_{II}(0, t) \quad (2.9)$$

$$\psi_{II}(L, t) = \psi_{III}(L, t) \quad , \quad \psi'_{II}(L, t) = \psi'_{III}(L, t), \quad (2.10)$$

solve the Schrödinger equation and analytic expressions for the wave function can be found for time-periodic magnetic potentials $B(t)$.

2.1.1 Single mode case

The most simple case of a periodic potential consists of only one frequency:

$$B(t) = B_1 \cos(\omega_1 t + \varphi_1) \quad (2.11)$$

Then, the overall time-dependent phase in eq.2.6 reads

$$\frac{\mu}{\hbar} \int B(t) dt = \alpha_1 \sin(\omega_1 t + \varphi_1), \quad \alpha_1 \equiv \frac{\mu B_1}{\hbar \omega_1} \quad (2.12)$$

With the help of the Jacobi-Angers expansion

$$e^{iz \sin \phi} = \sum_{n=-\infty}^{+\infty} J_n(z) e^{in\phi} \quad (2.13)$$

2.1 Schrödinger equation with a classical field

the phase factor can be rewritten which allows the determination of the constants $c(k)$ in eq.2.6 from the matching condition eq.2.9 by equating coefficients of $e^{i\omega t}$:

$$\begin{aligned}
\psi_I(0, t) &= \psi_{II}(0, t) \\
e^{-i\omega_0 t} &= e^{-i\frac{\mu B_1}{\hbar\omega_1} \sin(\omega_1 t + \varphi_1)} \int c_{II}(k) e^{-i\omega(k)t} dk \\
e^{-i\omega_0 t} e^{i\alpha_1 \sin(\omega_1 t + \varphi_1)} &= \int c_{II}(k) e^{-i\omega(k)t} dk \\
\sum_{n=-\infty}^{+\infty} J_n(\alpha_1) e^{in\varphi_1} e^{-i(\omega_0 - n\omega_1)t} &= \int c_{II}(k) e^{-i\omega(k)t} dk \\
\sum_{n=-\infty}^{+\infty} (-1)^n J_n(\alpha_1) e^{-in\varphi_1} e^{-i(\omega_0 + n\omega_1)t} &= \int c_{II}(k) e^{-i\omega(k)t} dk \\
\Rightarrow c_{II}(k) &= \sum_{n=-\infty}^{+\infty} (-1)^n J_n(\alpha_1) e^{-in\varphi_1} \delta(k - k_n) \tag{2.14}
\end{aligned}$$

where

$$k_n = \left(k_0^2 + \frac{2m}{\hbar} n\omega_1 \right)^{1/2} \tag{2.15}$$

whence follows

$$\omega(k_n) = \frac{\hbar k_n^2}{2m} = \frac{\hbar}{2m} \left(k_0^2 + \frac{2m}{\hbar} n\omega_1 \right) = \omega_0 + n\omega_1 \equiv \omega_n \tag{2.16}$$

Inserting the explicit form of $c_{II}(k)$ in the general ansatz for region II (eq.2.6) yields (also to be found in [Sud2001])

$$\psi_{II}(x, t) = e^{-i\alpha_1 \sin(\omega_1 t + \varphi_1)} \sum_{n=-\infty}^{+\infty} J_n(\alpha_1) (-1)^n e^{-in\varphi_1} e^{i\tilde{k}_n x} e^{-i\omega_n t} \tag{2.17}$$

with

$$\omega_n = \omega_0 + n\omega_1; \quad \tilde{k}_n = \left(k_0^2 - \frac{2m}{\hbar^2} \mu B_0 + \frac{2m}{\hbar} n\omega_1 \right)^{1/2} \tag{2.18}$$

Note, that due to the special form of the Jacobi-Angers expansion of the time-dependent phase factor, the matching condition could be fulfilled already with a discrete sum over equidistant k -values. The second condition in eq.2.9 containing the derivative of ψ is satisfied by the $c_{II}(k)$ obtained from the first condition because $m\omega_1/\hbar k_0 = \omega_1/v_0$ can be neglected against k_0 . This would not be valid

2. ENERGY EXCHANGE IN A TIME-DEPENDENT MAGNETIC FIELD

if k_n appeared in the exponent, but in the derivative of ψ it occurs as a prefactor (a similar argumentation was used for example in [GGK1994]).

$$\begin{aligned}
\psi'_{II}(0, t) &= e^{-i\alpha_1 \sin(\omega_1 t + \varphi_1)} \sum_{n=-\infty}^{+\infty} i\tilde{k}_n J_n(\alpha_1) (-1)^n e^{-in\varphi_1} e^{-i\omega_n t} \\
&= e^{-i\alpha_1 \sin(\omega_1 t + \varphi_1)} e^{-i\omega_0 t} \sum_{n=-\infty}^{+\infty} i\tilde{k}_n J_n(\alpha_1) e^{in(\omega_1 t + \varphi_1)} \\
&\simeq e^{-i\alpha_1 \sin(\omega_1 t + \varphi_1)} e^{-i\omega_0 t} i\tilde{k}_0 \sum_{n=-\infty}^{+\infty} J_n(\alpha_1) e^{in(\omega_1 t + \varphi_1)} \\
&= e^{-i\omega_0 t} i\tilde{k}_0 = \psi'_I(0, t)
\end{aligned}$$

At $x = L$, the expression for ψ_{II} (eq.2.17) has to be matched with the general ansatz for region III (eq.2.8). Again, we use the Jacobi-Angers expansion (eq.2.13). All occurring sums run from $-\infty$ to $+\infty$.

$$\begin{aligned}
\psi_{III}(L, t) &= \psi_{II}(L, t) \\
\dots &= e^{-i\alpha_1 \sin(\omega_1 t + \varphi_1)} \sum_n J_n(\alpha_1) (-1)^n e^{-in\varphi_1} e^{i\tilde{k}_n L} e^{-i\omega_n t} \\
\dots &= \sum_m J_m(-\alpha_1) e^{im(\omega_1 t + \varphi_1)} \sum_n J_n(\alpha_1) (-1)^n e^{-in\varphi_1} e^{i\tilde{k}_n L} e^{-i\omega_n t} \\
\dots &= \sum_{n,m} (-1)^{n+m} J_n(\alpha_1) J_m(\alpha_1) e^{-i(n-m)\varphi_1} e^{i\tilde{k}_n L} e^{-i\omega_{n-m} t} \\
\dots &= \sum_{l,m} (-1)^l J_{l+m}(\alpha_1) J_m(\alpha_1) e^{-il\varphi_1} e^{i\tilde{k}_{l+m} L} e^{-i\omega_l t} \\
\int c_{III}(k) e^{i\tilde{k}L} e^{-i\omega(k)t} dk &= \sum_{l,m} (-1)^l J_{l+m}(\alpha_1) J_m(\alpha_1) e^{-il\varphi_1} e^{i\tilde{k}_{l+m} L} e^{-i\omega_l t} \quad (2.19)
\end{aligned}$$

Equating coefficients of $e^{-i\omega t}$ shows that $c_{III}(k)$ must have the form

$$c_{III}(k) = \sum_l c_{III,l} \cdot \delta(k - k_l), \quad k_l^2 = (k_0^2 + \frac{2m}{\hbar} l\omega_1) \quad (2.20)$$

so that

$$\omega(k_l) = \frac{\hbar k_l}{2m} = \frac{\hbar}{2m} (k_0^2 + \frac{2m}{\hbar} l\omega_1) = \omega_0 + l\omega_1 = \omega_l \quad (2.21)$$

Inserting the special form of $c_{III}(k)$ (eq.2.20) in eq.2.19 leads to

$$c_{III,l} = (-1)^l e^{-il\varphi_1} \sum_m J_{l+m}(\alpha_1) J_m(\alpha_1) e^{i(\tilde{k}_{l+m} - \tilde{k}_l)L} \quad (2.22)$$

2.1 Schrödinger equation with a classical field

Due to the high kinetic energy of the incoming neutron compared to the magnetic potentials we may expand

$$\tilde{k}_n = \left(k_0^2 - \frac{2m}{\hbar^2} \mu B_0 + \frac{2m}{\hbar} n \omega_1 \right)^{1/2} \simeq k_0 - \frac{m}{\hbar^2 k_0} \mu B_0 + \frac{m}{\hbar k_0} n \omega_1 \quad (2.23)$$

$$\implies (\tilde{k}_l - \tilde{k}_n) L \simeq (l - n) \omega_1 \frac{mL}{\hbar k_0} = (l - n) \omega_1 T \quad (2.24)$$

where T denotes the neutron's time of flight through the field region. This leads to

$$c_{III,l} = (-1)^l e^{-il\varphi_1} \sum_m J_{l+m}(\alpha_1) J_m(\alpha_1) e^{im\omega_1 T} \quad (2.25)$$

The sum can be further evaluated by using Graf's addition theorem for Bessel functions [AS1964].

$$J_n(w) e^{in\chi} = \sum_{k=-\infty}^{+\infty} J_{n+k}(u) J_k(v) e^{ik\gamma} \quad (2.26)$$

If $u, v \in \mathbb{R}^+$ and $0 \leq \gamma \leq \pi$ there exists a geometrical relationship between the parameters u, v, w, γ , and χ (see fig.2.2). In our case, $\alpha_1 = \mu B_1 / \hbar \omega_1$ is negative,

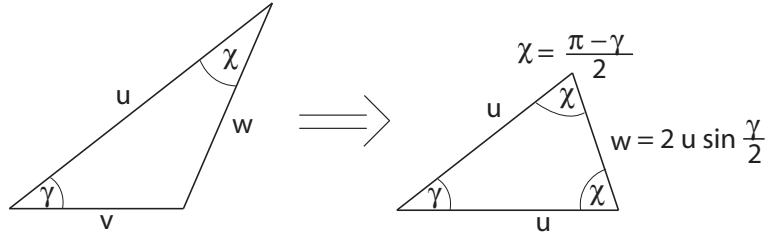


Figure 2.2: The geometrical relation for the parameters in Graf's addition theorem, if $u, v \in \mathbb{R}^+$ and $0 \leq \gamma \leq \pi$ for general and equal-sided triangles.

because $\mu < 0$. We therefore have to apply the identity $J_n(x) = (-1)^n J(-x)$ to be able to use the geometrical relation from which we deduce in our case where $u = v = -\alpha_1$ and $\gamma = \omega_1 T$ that $w = -2\alpha_1 \sin \omega_1 T / 2$ and $\chi = (\pi - \omega_1 T) / 2$. Inserting these expressions in eq.2.25 and performing the summation according to Graf's addition theorem yields

$$\begin{aligned} c_{III,l} &= (-1)^l e^{-il\varphi_1} (-1)^{l+2m} \sum_m J_{l+m}(-\alpha_1) J_m(-\alpha_1) e^{im\omega_1 T} \\ c_{III,l} &= e^{-il\varphi_1} J_l(-2\alpha_1 \sin \frac{\omega_1 T}{2}) e^{il(\pi - \omega_1 T)/2}, \quad |(-1)^l| = e^{-il\pi}, \\ c_{III,l} &= e^{-il\varphi_1} J_l(2\alpha_1 \sin \frac{\omega_1 T}{2}) e^{-il(\omega_1 T + \pi)/2} \end{aligned} \quad (2.27)$$

2. ENERGY EXCHANGE IN A TIME-DEPENDENT MAGNETIC FIELD

Now, the coefficient $c_{III}(k)$ in the general ansatz (eq.2.8) is determined and the final result for ψ_{III} reads

$$\psi_{III}(x, t) = \sum_{n=-\infty}^{+\infty} J_n(2\alpha_1 \sin \frac{\omega_1 T}{2}) e^{-in\eta_1} e^{i\tilde{k}_n x} e^{-i\omega_n t} \quad (2.28)$$

with

$$\omega_n = \omega_0 + n\omega_1, \quad \tilde{k}_n^2 = k_0^2 - \frac{2m}{\hbar^2}\mu B_0 + \frac{2m}{\hbar}n\omega_1, \quad \eta_1 = \varphi_1 + \frac{\omega_1 T + \pi}{2} \quad (2.29)$$

The result (eq.2.28) shows that the incoming plane wave with wave vector k_0 and energy $\hbar\omega_0$ is coherently split up into a superposition of plane waves whose energies are given by the initial energy $\hbar\omega_0$ plus an integer multiple of the frequency of the applied magnetic field $n\hbar\omega_1$. Thus, the energy transfer effected by passing the time-dependent magnetic field is quantized and the modulus of the transition amplitude for the exchange of an energy amount $n\hbar\omega_1$ between neutron and field is given by the Bessel function of n -th order. The probabilities for emission and absorption of the same amount of energy are equal. A seemingly obvious interpretation of this result would be that the neutron exchanges n photons of frequency $\hbar\omega_1$ with the magnetic field. We will discuss that conclusion in detail in sec.2.4. From the argument of the Bessel function, we deduce that increasing the field amplitude B_1 leads to a higher probability of exchanging large amounts of energy. For $\omega_1 T = 2n\pi$, all amplitudes for energy exchanges vanish. The neutron exactly experiences integer multiples of the oscillation period and yet no resulting energy transfer can remain. Note, that the transition amplitudes become equal for different time of flights T_1 and T_2 if $\omega_1(T_1 - T_2) = 2n 2\pi$, thus obeying the 4π -spinor symmetry [RZB⁺1975].

2.1.2 Conservation of momentum and energy

The fact, that the transition probabilities for emission and absorption are equal suggests that the expectation values for energy and momentum after passing the field stay unchanged. To calculate the expectation values in regions I and III, one has to define the scalar product in a sense, that the set of plane wave forms an orthonormal basis. In region I we thus define¹

$$\langle \phi | \psi \rangle \equiv \lim_{R \rightarrow \infty} \frac{1}{R} \int_{-R}^0 \phi^*(x, t) \psi(x, t) dx \quad (2.30)$$

¹This definition strongly resembles the limits occurring in the theory of "almost periodic functions" [Boh1925]. The possibility of defining "almost orthogonal" function in a similar sense may be an interesting subject for further, more mathematically oriented investigations.

2.1 Schrödinger equation with a classical field

yielding for two different plane waves

$$\langle k|k' \rangle = \lim_{R \rightarrow \infty} \frac{1}{R} \int_{-R}^0 e^{-ikx+i\omega_k t} e^{ik'x-i\omega_{k'} t} dx \quad (2.31)$$

$$= e^{i(\omega_k - \omega_{k'})t} \lim_{R \rightarrow \infty} \frac{1}{R} \int_{-R}^0 e^{-i(k-k')x} dx \quad (2.32)$$

$$= e^{i(\omega_k - \omega_{k'})t} \lim_{R \rightarrow \infty} \frac{1}{R} \frac{i}{k-k'} \left(1 - e^{i(k-k')R}\right) \quad (2.33)$$

$$= e^{i(\omega_k - \omega_{k'})t} \delta_{k,k'} = \delta_{k,k'} \quad (2.34)$$

For $k \neq k'$, the limit is zero because the imaginary exponent leads to a purely oscillating behaviour and can thus not compensate for the increasing divisor R . To prove the result for the case $k = k'$, we start from the defining eq.2.30

$$\begin{aligned} \langle k|k \rangle &= \lim_{R \rightarrow \infty} \frac{1}{R} \int_{-R}^0 e^{-ikx+i\omega_k t} e^{ikx-i\omega_k t} dx \\ &= \lim_{R \rightarrow \infty} \frac{1}{R} \int_{-R}^0 1 \cdot dx = \lim_{R \rightarrow \infty} \frac{1}{R} \cdot R = \lim_{R \rightarrow \infty} 1 = 1 \end{aligned}$$

Now, we can calculate the expectation value of the momentum in region I:

$$\langle \psi_I | \hat{p} | \psi_I \rangle = \lim_{R \rightarrow \infty} \frac{1}{R} \int_{-R}^0 \psi_I^*(x, t) \frac{\hbar}{i} \frac{\partial}{\partial x} \psi_I(x, t) \quad (2.35)$$

$$= \lim_{R \rightarrow \infty} \frac{1}{R} \int_{-R}^0 e^{-ik_0 x} \frac{\hbar}{i} \frac{\partial}{\partial x} e^{ik_0 x} dx = \hbar k_0 \equiv p_0 \quad (2.36)$$

As expected for a plane wave with wave vector k_0 , the momentum is $\hbar k_0$, the definition of the scalar product (eq.2.30) was therefore reasonable. Now we turn to region III where we define the scalar product in a similar way

$$\langle \phi | \psi \rangle \equiv \lim_{R \rightarrow \infty} \frac{1}{R-L} \int_L^R \phi^*(x, t) \psi(x, t) dx = \lim_{R \rightarrow \infty} \frac{1}{R} \int_L^R \phi^* \psi dx \quad (2.37)$$

2. ENERGY EXCHANGE IN A TIME-DEPENDENT MAGNETIC FIELD

Hence, we get for the expectation value of the momentum for the state ψ_{III} using the abbreviations defined in eq.2.29

$$\begin{aligned}
\langle \psi_{III} | \hat{p} | \psi_{III} \rangle &= \lim_{R \rightarrow \infty} \frac{1}{R} \int_L^R \psi_{III}^*(x, t) \frac{\hbar}{i} \frac{\partial}{\partial x} \psi_{III}(x, t) dx \\
&= \lim_{R \rightarrow \infty} \frac{1}{R} \int_L^R \sum_n J_n e^{in\eta_1} e^{-ik_n x} e^{i\omega_n t} \times \\
&\quad \frac{\hbar}{i} \frac{\partial}{\partial x} \sum_m J_m e^{-im\eta_1} e^{ik_m x} e^{-i\omega_m t} dx \\
&= \lim_{R \rightarrow \infty} \frac{1}{R} \int_L^R \sum_{n,m} J_n J_m e^{i(n-m)\eta_1} e^{-i(k_n - k_m)x} e^{i(\omega_n - \omega_m)t} \hbar k_m dx \\
&= \sum_{n,m} J_n J_m e^{i(n-m)\eta_1} e^{i(\omega_n - \omega_m)t} \hbar k_m \lim_{R \rightarrow \infty} \frac{1}{R} \int_L^R e^{-i(k_n - k_m)x} dx \\
&= \sum_{n,m} J_n J_m e^{i(n-m)\eta_1} e^{i(\omega_n - \omega_m)t} \hbar k_m \delta_{nm} \\
&= \sum_n J_n^2 \hbar k_n \cong \hbar k_0 \sum_n J_n^2 + \hbar \frac{\omega}{v_0} \sum_n n J_n^2 = \hbar k_0
\end{aligned}$$

In the last line, we have expanded the k -vector in the usual way and then used the identity $\sum_n J_n^2 = 1$, valid for summation from $-\infty$ to $+\infty$. The second second term vanishes due to the relation $J_n^2 = J_{-n}^2$. The expectation value of the momentum is thus equal before and after passing the field region, as expected for a harmonically oscillating potential. Note, that we have omitted the constant shift due to the static field B_0 . It can be taken into account without changing the calculation by just using \tilde{k}_0 (for exact definition see eq.2.5) instead of k_0 . To calculate the probability distribution of the momentum, we write the states in the Heisenberg picture, i.e. we can omit the time dependence and use Dirac-notation instead of position space representation

$$|\psi_I\rangle = |k_0\rangle, \quad |\psi_{III}\rangle = \sum_n J_n e^{-in\eta_1} |k_n\rangle \quad (2.38)$$

In this way, the calculation of the momentum distribution $P(k)$ can be performed more transparent

$$P_I(k) = |\langle \psi_I | k \rangle|^2 = |\langle k_0 | k \rangle|^2 = |\delta_{k_0, k}|^2 = \delta_{k_0, k} \quad (2.39)$$

$$P_{III}(k) = |\langle \psi_{III} | k \rangle|^2 = \left| \sum_n J_n e^{in\eta_1} \langle k_n | k \rangle \right|^2 \quad (2.40)$$

$$= \left| \sum_n J_n e^{in\eta_1} \delta_{k_n, k} \right|^2 = J_n^2 \delta_{k_n, k} \quad (2.41)$$

2.1 Schrödinger equation with a classical field

The momentum distribution has thus changed after passing the oscillating magnetic field (see fig.2.3), but the expectation value stays the same.

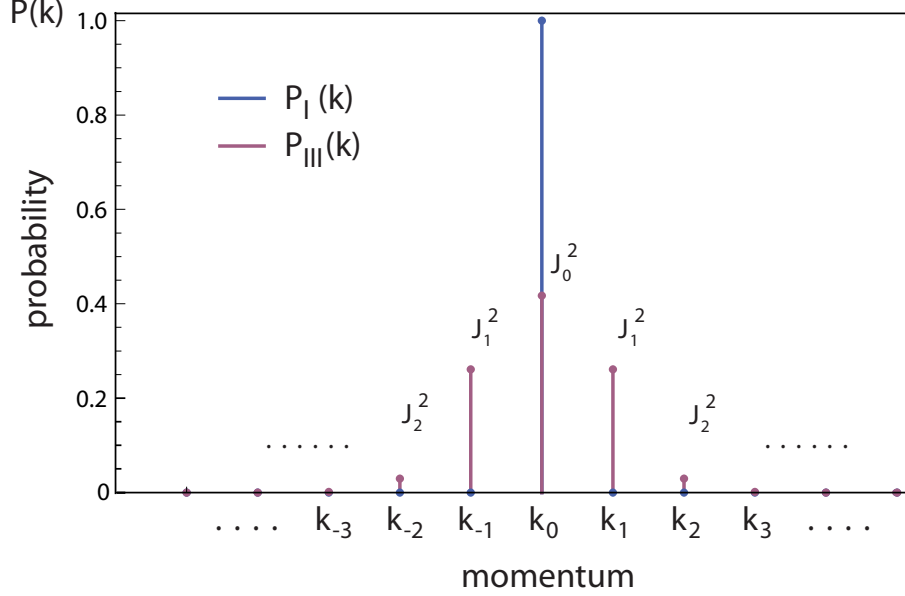


Figure 2.3: The momentum distributions $P_I(k) = |\langle \psi_I | k \rangle|^2$ and $P_{III}(k) = |\langle \psi_{III} | k \rangle|^2$. Only discrete amounts of kinetic energy/momentum are exchanged. k_n corresponds to an exchange of $n\hbar\omega$. The probabilities for absorption and emission of the same amount of energy are equal. The strength of the magnetic field is chosen in a way that the argument of the Bessel functions equals 1.25.

The calculation of the total energy E_{tot} works quite analogously

$$\langle \psi_I | E_{tot} | \psi_I \rangle = \lim_{R \rightarrow \infty} \frac{1}{R} \int_{-R}^0 \psi_I^*(x, t) \left(-\frac{\hbar}{i} \frac{\partial}{\partial t} \right) \psi_I(x, t) dx \quad (2.42)$$

$$= \lim_{R \rightarrow \infty} \frac{1}{R} \int_{-R}^0 e^{-i(\bar{k}_0 x - \omega_0 t)} \left(-\frac{\hbar}{i} \frac{\partial}{\partial t} \right) e^{i(\bar{k}_0 x - \omega_0 t)} dx \quad (2.43)$$

$$= \hbar\omega_0 \lim_{R \rightarrow \infty} \frac{1}{R} \int_{-R}^0 e^{-i(\bar{k}_0 x - \omega_0 t)} e^{i(\bar{k}_0 x - \omega_0 t)} dx \quad (2.44)$$

$$= \hbar\omega_0 \lim_{R \rightarrow \infty} \frac{1}{R} \int_{-R}^0 1 \cdot dx = \hbar\omega_0 \quad (2.45)$$

For ψ_{III} we need

$$-\frac{\hbar}{i} \frac{\partial}{\partial t} \psi_{III}(x, t) = \sum_n \hbar\omega_n J_n(\beta_1) e^{-in\eta_1} e^{i\bar{k}_n x} e^{-i\omega_n t}$$

2. ENERGY EXCHANGE IN A TIME-DEPENDENT MAGNETIC FIELD

to calculate

$$\begin{aligned}
\langle \psi_{III} | E_{tot} | \psi_{III} \rangle &= \lim_{R \rightarrow \infty} \frac{1}{R} \int_{-R}^0 \psi_{III}^*(x, t) \left(-\frac{\hbar}{i} \frac{\partial}{\partial t} \right) \psi_{III}(x, t) dx \\
&= \lim_{R \rightarrow \infty} \frac{1}{R} \int_{-R}^0 \sum_m J_m e^{im\eta_1} e^{-i\tilde{k}_m x} e^{i\omega_m t} \times \\
&\quad \sum_n \hbar\omega_n J_n e^{-in\eta_1} e^{i\tilde{k}_n x} e^{-i\omega_n t} dx \\
&= \sum_{n,m} \hbar\omega_n J_n J_m e^{-i(n-m)\eta_1} e^{-i(n-m)\omega_1 t} \times \\
&\quad \lim_{R \rightarrow \infty} \frac{1}{R} \int_{-R}^0 e^{i(\tilde{k}_n - \tilde{k}_m)x} dx \\
&= \sum_{n,m} \hbar\omega_n J_n J_m e^{-i(n-m)\eta_1} e^{-i(n-m)\omega_1 t} \delta_{n,m} \\
&= \sum_n \hbar\omega_n J_n^2 = \hbar\omega_0 \sum_n J_n^2 + \hbar\omega_1 \sum_n n J_n^2 = \hbar\omega_0
\end{aligned}$$

The total energy after passing the magnetic field is conserved as well. For completeness's sake, we also give the expectation values of the kinetic energy.

$$\begin{aligned}
\langle \psi_I | E_{kin} | \psi_I \rangle &= \langle \psi_I | \frac{\hat{p}^2}{2m} | \psi_I \rangle = \\
&= \lim_{R \rightarrow \infty} \frac{1}{R} \int_{-R}^0 \psi_I^*(x, t) \left(-\frac{\hbar^2}{2m} \frac{\partial^2}{\partial x^2} \right) \psi_I(x, t) dx \\
&= \lim_{R \rightarrow \infty} \frac{1}{R} \int_{-R}^0 e^{-i(\tilde{k}_0 x - \omega_0 t)} \left(-\frac{\hbar^2}{2m} \frac{\partial^2}{\partial x^2} \right) e^{i(\tilde{k}_0 x - \omega_0 t)} dx \\
&= \frac{\hbar^2 \tilde{k}_0^2}{2m} = \frac{\hbar^2 k_0^2}{2m} - \mu B_0 = \hbar\omega_0 - \mu B_0
\end{aligned}$$

In region III we have

$$-\frac{\hbar^2}{2m} \frac{\partial^2}{\partial x^2} \psi_{III}(x, t) = \sum_n \frac{\hbar^2 \tilde{k}_n^2}{2m} J_n(\beta_1) e^{-in\eta_1} e^{i\tilde{k}_n x} e^{-i\omega_n t}$$

2.1 Schrödinger equation with a classical field

leading to

$$\begin{aligned}
\langle \psi_{III} | E_{kin} | \psi_{III} \rangle &= \lim_{R \rightarrow \infty} \frac{1}{R} \int_{-R}^0 \psi_{III}^*(x, t) \left(-\frac{\hbar^2}{2m} \frac{\partial^2}{\partial x^2} \right) \psi_{III}(x, t) dx \\
&= \lim_{R \rightarrow \infty} \frac{1}{R} \int_{-R}^0 \sum_m J_m e^{im\eta_1} e^{-i\tilde{k}_m x} e^{i\omega_m t} \times \\
&\quad \sum_n \frac{\hbar^2 \tilde{k}_n^2}{2m} J_n e^{-in\eta_1} e^{i\tilde{k}_n x} e^{-i\omega_n t} dx \\
&= \sum_{n,m} \frac{\hbar^2 \tilde{k}_n^2}{2m} J_n J_m e^{-i(n-m)\eta_1} e^{-i(n-m)\omega_1 t} \times \\
&\quad \lim_{R \rightarrow \infty} \frac{1}{R} \int_{-R}^0 e^{i(\tilde{k}_n - \tilde{k}_m)x} dx \\
&= \sum_{n,m} \frac{\hbar^2 \tilde{k}_n^2}{2m} J_n J_m e^{-i(n-m)\eta_1} e^{-i(n-m)\omega_1 t} \cdot \delta_{n,m} \\
&= \sum_n \frac{\hbar^2 \tilde{k}_n^2}{2m} J_n^2 = \frac{\hbar^2 k_0^2}{2m} \sum_n J_n^2 - \mu B_0 \sum_n J_n^2 + \hbar \omega_1 \sum_n n J_n^2 \\
&= \hbar \omega_0 - \mu B_0
\end{aligned}$$

The kinetic energy is conserved and equals total energy minus the potential energy arising from the static field.

2.1.3 Generalisation to arbitrary number of field modes

The results for the single mode field can be generalized to a time dependent field consisting of an arbitrary, countable number of frequencies whose ratio is a rational number, i.e. an arbitrary periodic field

$$B(t) = \sum_{i=1}^N B_i \cos(\omega_i t + \varphi_i) \quad (2.46)$$

The periodicity of $B(t)$ is given by greatest common denominator ω_g of the occurring frequencies ω_i . The calculation consists basically of the same steps due to the possibility of factorization of a sum in an exponent. To obtain a compact

2. ENERGY EXCHANGE IN A TIME-DEPENDENT MAGNETIC FIELD

notation we will use vectors and scalar products in the form

$$\begin{aligned}\vec{n} &= (n_1, n_2, \dots, n_N), \quad \vec{\omega} = (\omega_1, \omega_2, \dots, \omega_N), \dots \\ \vec{n}\vec{\varphi} &= n_1\varphi_1 + n_2\varphi_2 + \dots + n_N\varphi_N, \dots \\ c_{\vec{n}} &= c_{n_1, n_2, \dots, n_N} \\ \sum_{\vec{n}} &= \sum_{n_1, n_2, \dots, n_N}\end{aligned}$$

In region I, we have the same wavefunction ψ_I as in eq.2.5, i.e. a single plane wave with wave vector k_0 . In region II, the time-dependent phase factor (see eq.2.6) changes according to the altered magnetic field (eq.2.46).

$$e^{-i\frac{\mu}{\hbar} \int dt' B(t')} = e^{-i \sum_{i=1}^N \alpha_i \sin(\omega_i t + \varphi_i)}, \quad \alpha_i \equiv \frac{\mu B_i}{\hbar \omega_i} \quad (2.47)$$

The matching condition at $x = 0$ therefore reads

$$\begin{aligned}\psi_I(0, t) &= \psi_{II}(0, t) \\ e^{-i\omega_0 t} &= e^{-i \sum_{i=1}^N \alpha_i \sin(\omega_i t + \varphi_i)} \int c_{II}(k) e^{-i\omega(k)t} dk \\ e^{-i\omega_0 t} e^{i \sum_{i=1}^N \alpha_i \sin(\omega_i t + \varphi_i)} &= \int c_{II}(k) e^{-i\omega(k)t} dk\end{aligned}$$

We can now use the Jacobi-Angers expansion to rewrite the exponent

$$\begin{aligned}\sum_{\vec{n}=-\infty}^{+\infty} J_{-n_1}(\alpha_1) \dots J_{-n_N}(\alpha_N) e^{-i\vec{n}\vec{\varphi}} e^{-i(\omega_0 - \vec{n}\vec{\omega})t} &= \int c_{II}(k) e^{-i\omega(k)t} dk \\ \Rightarrow c_{II}(k) &= \sum_{n_1, \dots, n_N=-\infty}^{+\infty} J_{-n_1}(\alpha_1) \dots J_{-n_N}(\alpha_N) e^{-i\vec{n}\vec{\varphi}} \delta(k - k_{\vec{n}})\end{aligned} \quad (2.48)$$

where

$$k_{\vec{n}} = \left(k_0^2 + \frac{2m}{\hbar} \vec{n}\vec{\omega} \right)^{1/2} \quad (2.49)$$

whence follows

$$\omega(k_{\vec{n}}) = \frac{\hbar k_{\vec{n}}^2}{2m} = \frac{\hbar}{2m} \left(k_0^2 + \frac{2m}{\hbar} \vec{n}\vec{\omega} \right) = \omega_0 + \vec{n}\vec{\omega} \equiv \omega_{\vec{n}} \quad (2.50)$$

Inserting the explicit form of $c_{II}(k)$ (eq.2.48) valid for arbitrary periodic fields in the general ansatz for region II (eq.2.6) yields

$$\begin{aligned}\psi_{II}(x, t) &= e^{-i \sum_{i=1}^N \alpha_i \sin(\omega_i t + \varphi_i)} \times \\ &\quad \sum_{n_1, \dots, n_N=-\infty}^{+\infty} J_{-n_1}(\alpha_1) \dots J_{-n_N}(\alpha_N) e^{-i\vec{n}\vec{\varphi}} e^{i\vec{k}_{\vec{n}}x} e^{-i\omega_{\vec{n}}t}\end{aligned} \quad (2.51)$$

2.1 Schrödinger equation with a classical field

with

$$\omega_{\vec{n}} = \omega_0 + \vec{n}\vec{\omega}; \quad \tilde{k}_{\vec{n}} = \left(k_0^2 - \frac{2m}{\hbar^2} \mu B_0 + \frac{2m}{\hbar} \vec{n}\vec{\omega} \right)^{1/2} \quad (2.52)$$

As already mentioned, the steps of the calculation are in principle the same as in the case of the single-mode field. Above that, one could obviously obtain the results for the single-mode field from the general expressions by simply setting $N = 1$. Nevertheless, it is more comprehensive to explicitly solve the differential equation for the less complex case of the single mode field where the notation is more transparent and one can follow the steps of calculation more easily. When the single-mode case is understood, the extension to the arbitrary number of modes is just a matter of conclusion by analogy.

To perform the matching at $x = L$, we rewrite ψ_{II} with the help of the Jacobi-Angers expansion. Summations over i all run from 1 to N whereas summations over the n_i 's, m_i 's and l_i 's are meant to run from $-\infty$ to $+\infty$.

$$\begin{aligned} \psi_{II}(L, t) &= e^{-i \sum_i \alpha_i \sin(\omega_i t + \varphi_i)} \\ &\quad \sum_{n_1, \dots, n_N} J_{-n_1}(\alpha_1) \dots J_{-n_N}(\alpha_N) e^{-i \vec{n} \vec{\varphi}} e^{i \tilde{k}_{\vec{n}} L} e^{-i \omega_{\vec{n}} t} \\ \dots &= \sum_{m_1, \dots, m_N} J_{m_1}(-\alpha_1) \dots J_{m_N}(-\alpha_N) e^{i \vec{m} (\vec{\omega} t + \vec{\varphi})} \\ &\quad \sum_{n_1, \dots, n_N} J_{-n_1}(\alpha_1) \dots J_{-n_N}(\alpha_N) e^{-i \vec{n} \vec{\varphi}} e^{i \tilde{k}_{\vec{n}} L} e^{-i \omega_{\vec{n}} t} \\ \dots &= \sum_{\vec{n}, \vec{m}} (-1)^{\sum_i n_i + m_i} J_{n_1}(\alpha_1) J_{m_1}(\alpha_1) \dots J_{n_N}(\alpha_N) J_{m_N}(\alpha_N) \\ &\quad e^{-i (\vec{n} - \vec{m}) \vec{\varphi}} e^{i \tilde{k}_{\vec{n}} L} e^{-i \omega_{\vec{n} - \vec{m}} t} \\ \dots &= \sum_{\vec{l}, \vec{m}} (-1)^{\sum_i l_i} J_{m_1 + l_1}(\alpha_1) J_{m_1}(\alpha_1) \dots J_{m_N + l_N}(\alpha_N) J_{m_N}(\alpha_N) \\ &\quad e^{-i \vec{l} \vec{\varphi}} e^{i \tilde{k}_{\vec{m} + \vec{l}} L} e^{-i \omega_{\vec{l}} t} \end{aligned}$$

Comparison with the general solution in region III (eq.2.8) at $x = L$ thus reads

$$\begin{aligned} \int c_{III}(k) e^{i \tilde{k} L} e^{-i \omega(k) t} dk &= \sum_{\vec{l}, \vec{m}} J_{m_1 + l_1}(\alpha_1) J_{m_1}(\alpha_1) \dots J_{m_N + l_N}(\alpha_N) J_{m_N}(\alpha_N) \\ &\quad (-1)^{\sum_i l_i} e^{-i \vec{l} \vec{\varphi}} e^{i \tilde{k}_{\vec{m} + \vec{l}} L} e^{-i \omega_{\vec{l}} t} \end{aligned} \quad (2.53)$$

Equating coefficients of $e^{-i \omega t}$ shows that $c_{III}(k)$ must have the form

$$c_{III}(k) = \sum_{\vec{l}} c_{III, \vec{l}} \cdot \delta(k - k_{\vec{l}}), \quad k_{\vec{l}}^2 = \left(k_0^2 + \frac{2m}{\hbar} \vec{l} \vec{\omega} \right) \quad (2.54)$$

2. ENERGY EXCHANGE IN A TIME-DEPENDENT MAGNETIC FIELD

so that

$$\omega(k_{\vec{l}}) = \frac{\hbar k_{\vec{l}}}{2m} = \frac{\hbar}{2m}(k_0^2 + \frac{2m}{\hbar}\vec{l}\vec{\omega}) = \omega_0 + \vec{l}\vec{\omega} = \omega_{\vec{l}} \quad (2.55)$$

Inserting the special form of $c_{III}(k)$ (eq.2.54) in eq.2.53 and expanding the k-vector like in eq.2.23 leads to

$$c_{III,\vec{l}} = (-1)^{\sum_i l_i} e^{-i\vec{l}\vec{\varphi}} \sum_{\vec{m}} J_{m_1+l_1}(\alpha_1) J_{m_1}(\alpha_1) \dots J_{m_N+l_N}(\alpha_N) J_{m_N}(\alpha_N) e^{i\vec{m}\vec{\omega}L} \quad (2.56)$$

This expression can be fully factorized

$$c_{III,\vec{l}} = \prod_{i=1}^N \left((-1)^{l_i} e^{-il_i\varphi_i} \sum_{m_i=-\infty}^{+\infty} J_{m_i+l_i}(\alpha_i) J_{m_i}(\alpha_i) e^{im_i\omega_i L} \right) \quad (2.57)$$

The summation over the m_i 's can be further evaluated by using Graf's addition theorem (eq.2.26) like in the single-mode field case.

$$c_{III,\vec{l}} = \prod_{i=1}^N \left(e^{-il_i\varphi_i} J_{l_i}(2\alpha_i \sin \frac{\omega_i T}{2}) e^{-il_i(\omega_i T + \pi)/2} \right) \quad (2.58)$$

The general solution in region III can now be written in compact notation as follows

$$\psi_{III}(x, t) = \sum_{\vec{n}} J_{n_1}(\beta_1) \dots J_{n_N}(\beta_N) e^{-i\vec{n}\vec{\eta}} e^{i\vec{k}_{\vec{n}}x} e^{-i\omega_{\vec{n}}t} \quad (2.59)$$

with

$$\omega_{\vec{n}} = \omega_0 + \vec{n}\vec{\omega}, \quad \tilde{k}_{\vec{n}}^2 = k_0^2 - \frac{2m}{\hbar^2} \mu B_0 + \frac{2m}{\hbar} \vec{n}\vec{\omega} \quad (2.60)$$

$$\eta_i = \varphi_i + \frac{\omega_i T + \pi}{2}, \quad \beta_i = 2\alpha_i \sin \frac{\omega_i T}{2} \quad (2.61)$$

One can see that different values of the n_i 's can lead to the same $\omega_{\vec{n}}$, i.e. the same value for $\vec{n}\vec{\omega}$. Thus, all possible combinations of the n_i 's leading to the same $\omega_{\vec{n}}$ contribute to a certain energy exchange $\vec{n}\vec{\omega}$. For example, if some frequencies ω_i contained in the magnetic field signal (eq.2.46) have an integer-number ratio, the situation of no energy transfer can be obtained for all $n_j = 0$, but also for a set of n_i 's containing positive and negative values in a way, that the energy absorption and emission of different frequencies exactly cancel each other.

Again, one has to be careful with the interpretation of the end result (eq.2.59) in the general case of arbitrary frequencies. One could conclude that $J_k(\beta_l)$ means that k photons of frequency ω_l have been transferred between neutron and field. But till now, we are only dealing with classical fields, the formally correct introduction of photons requires the quantization of the magnetic field, as performed in chapter 2.4.

2.2 Experimental verification

2.2.1 Polarized neutrons

The transition amplitudes to different energies derived in section 2.1 and given essentially by combinations of Bessel functions J_n can be measured in an interferometric setup. Therefore we place the time-dependent magnetic field generated by an ac-coil (field length $L = 42$ mm) in one beam path and in the other one we leave the neutrons unchanged (see fig.2.4).

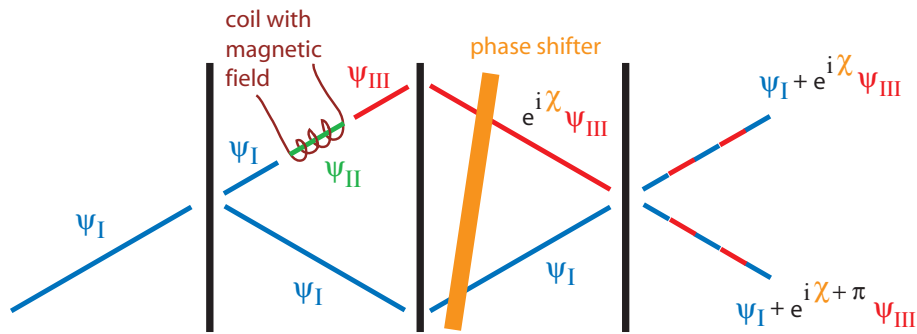


Figure 2.4: Schematic setup for the measurement of the transition amplitudes. Analysis of the time dependent intensity pattern after the third plate resulting from the superposition of ψ_I and ψ_{III} allows the determination of the coefficients of the different plane waves of ψ_{III} , i.e. the transition amplitudes.

After the third interferometer plate the two beams interfere and the normed intensity in the O-beam reads

$$\begin{aligned}
 I_O(x, t) &= \frac{1}{4} |\psi_I(x, t) + e^{i\chi} \psi_{III}(x, t)|^2 \\
 &= \frac{1}{4} (|\psi_I(x, t)|^2 + |\psi_{III}(x, t)|^2 + 2\text{Re} \{ \psi_I^* e^{i\chi} \psi_{III} \}) \\
 &= \frac{1}{2} (1 + \text{Re} \{ \psi_I^* e^{i\chi} \psi_{III} \})
 \end{aligned} \tag{2.62}$$

where χ denotes the phase difference due to the auxiliary phase shifter and ψ_I and ψ_{III} are given by eq.2.5 and eq.2.59 respectively. At first, we want to focus on the case of a single-mode magnetic field. When the explicit forms of ψ_I and

2. ENERGY EXCHANGE IN A TIME-DEPENDENT MAGNETIC FIELD

ψ_{III} are inserted and k_n is expanded like in eq.2.23

$$\begin{aligned}\psi_{III} &= \sum_{n=-\infty}^{+\infty} J_n(\beta_1) e^{-in\eta_1} e^{i\tilde{k}_n x} e^{-i\omega_n t} \\ &\approx e^{i\tilde{k}_0 x} e^{-i\omega_0 t} \sum_{n=-\infty}^{+\infty} J_n(\beta_1) e^{-in\eta_1} e^{in\frac{\omega_1}{v_0} x} e^{-in\omega_1 t} \\ \psi_I &= e^{i\tilde{k}_0 x} e^{-i\omega_0 t} \\ \psi_I^* \psi_{III} &= \sum_{n=-\infty}^{+\infty} J_n(\beta_1) e^{-in\eta_1} e^{in\frac{\omega_1}{v_0} x} e^{-in\omega_1 t}\end{aligned}$$

the intensity reads

$$I_O(x, t) = \frac{1}{2} \left(1 + \text{Re} \left\{ e^{i\chi} \sum_{n=-\infty}^{+\infty} J_n(\beta_1) e^{-in\eta_1} e^{in\frac{\omega_1}{v_0} x} e^{-in\omega_1 t} \right\} \right) \quad (2.63)$$

$$= \frac{1}{2} \left(1 + \text{Re} \left\{ e^{i\chi} \sum_{n=-\infty}^{+\infty} J_n(\beta_1) e^{-in(\omega_1 t + \xi_1)} \right\} \right) \quad (2.64)$$

$$= \frac{1}{2} \left(1 + \text{Re} \left\{ e^{i\chi} e^{-\beta_1 \sin(\omega_1 t + \xi_1)} \right\} \right) \quad (2.65)$$

$$= \frac{1}{2} \left(1 + \cos(\chi - \beta_1 \sin(\omega_1 t + \xi_1)) \right) \quad (2.66)$$

where we used the Jacobi-Angers expansion (eq.2.13) and the abbreviations

$$\beta_1 = 2\alpha_1 \sin \frac{\omega_1 T}{2}, \quad \eta_1 = \varphi_1 + \frac{\omega_1 T + \pi}{2}, \quad \xi_1 = \eta_1 - \frac{\omega_1}{v_0} x, \quad v_0 = \hbar k_0 / m \quad (2.67)$$

From eqs.2.63-2.66, it can be deduced that the intensity pattern has the same periodicity as the magnetic field, i.e. $2\pi/\omega_1$. Above that, the transition amplitudes occurring in ψ_{III} , namely the Bessel functions J_n can be obtained from the Fourier components of the intensity pattern. Therefore, we rewrite the intensity

from the second line (eq.2.64)

$$\begin{aligned}
I_O(x, t) &= \frac{1}{2} + \frac{1}{2} \operatorname{Re} \left\{ e^{i\chi} \sum_{n=-\infty}^{+\infty} J_n(\beta_1) e^{-in(\omega_1 t + \xi_1)} \right\} \\
\dots &= \frac{1}{2} + \frac{1}{2} \sum_{n=-\infty}^{+\infty} J_n(\beta_1) \cos(\chi - n\omega_1 t - n\xi_1) \\
\dots &= \frac{1}{2} + \frac{1}{4} \sum_{n=-\infty}^{+\infty} J_n(\beta_1) (e^{i(\chi - n\omega_1 t - n\xi_1)} + e^{-i(\chi - n\omega_1 t - n\xi_1)}) \\
\dots &= \frac{1}{2} + \frac{1}{4} \sum_{n=-\infty}^{+\infty} J_{-n}(\beta_1) e^{i(\chi + n\omega_1 t + n\xi_1)} + J_n(\beta_1) e^{i(-\chi + n\omega_1 t + n\xi_1)} \\
\dots &= \frac{1}{2} + \frac{1}{4} \sum_{n=-\infty}^{+\infty} (J_n(\beta_1) (-1)^n e^{i\chi} + J_n(\beta_1) e^{-i\chi}) e^{in\xi_1} e^{in\omega_1 t}
\end{aligned}$$

and compare it with the ordinary Fourier decomposition valid for every function with period $2\pi/\omega_1$.

$$I_O(x, t) = \sum_{n=-\infty}^{+\infty} c_n e^{in\omega_1 t}$$

$$\implies c_0 = \frac{1}{2} (1 + J_0(\beta_1) \cos \chi) \quad (2.68)$$

$$c_{2n} = \frac{1}{2} e^{i2n\xi_1} J_{2n}(\beta_1) \cos \chi \quad (2.69)$$

$$c_{2n+1} = -\frac{i}{2} e^{i(2n+1)\xi_1} J_{2n+1}(\beta_1) \sin \chi \quad (2.70)$$

Thus, we can extract the transition amplitudes of ψ_{III} calculated above from the Fourier components of the time-resolved interference pattern of ψ_I and ψ_{III} .

These calculations can of course be generalized to the case of arbitrary periodic magnetic fields (eq.2.46), where ψ_{III} is given by eq.2.59. We again expand the k -vector and obtain ψ_{III} in the form

$$\psi_{III}(x, t) = \sum_{\vec{n}} J_{n_1}(\beta_1) \dots J_{n_N}(\beta_N) e^{-i\vec{n}\vec{\eta}} e^{i\vec{k}_0 x} e^{i\frac{\vec{n}\vec{\omega}}{v_0} x} e^{-i\omega_{\vec{n}} t} \quad (2.71)$$

$$= e^{i\vec{k}_0 x} e^{-i\omega_0 t} \sum_{\vec{n}} J_{n_1}(\beta_1) \dots J_{n_N}(\beta_N) e^{-i\vec{n}\vec{\xi}} e^{-i\vec{\omega}\vec{n} t} \quad (2.72)$$

$$= \psi_I(x, t) \sum_{\vec{n}} J_{n_1}(\beta_1) \dots J_{n_N}(\beta_N) e^{-i\vec{n}\vec{\xi}} e^{-i\vec{\omega}\vec{n} t} \quad (2.73)$$

2. ENERGY EXCHANGE IN A TIME-DEPENDENT MAGNETIC FIELD

where

$$\omega_{\vec{n}} = \omega_0 + \vec{n}\vec{\omega}, \quad \tilde{k}_0^2 = k_0^2 - \frac{2m}{\hbar^2}\mu B_0 \quad (2.74)$$

$$\eta_i = \varphi_i + \frac{\omega_i T + \pi}{2}, \quad \beta_i = 2\alpha_i \sin \frac{\omega_i T}{2}, \quad \xi_i = \eta_i - \frac{\omega_i}{v_0}x \quad (2.75)$$

The intensity then reads

$$I_O(x, t) = \frac{1}{2} + \frac{1}{2} \operatorname{Re} \left\{ e^{i\chi} \sum_{\vec{n}} J_{n_1}(\beta_1) \cdots J_{n_N}(\beta_N) e^{-i\vec{n}(\vec{\xi} + \vec{\omega}t)} \right\} \quad (2.76)$$

$$= \frac{1}{2} \left(1 + \operatorname{Re} \left\{ e^{i\chi} \prod_{i=1}^N \sum_{n_i=-\infty}^{+\infty} J_{n_i}(\beta_i) e^{-in_i(\omega_i t + \xi_i)} \right\} \right) \quad (2.77)$$

$$= \frac{1}{2} \left(1 + \operatorname{Re} \left\{ e^{i\chi} \prod_{i=1}^N e^{-i\beta_i \sin(\omega_i t + \xi_i)} \right\} \right) \quad (2.78)$$

$$= \frac{1}{2} \left(1 + \operatorname{Re} \left\{ e^{i\chi} e^{-i \sum_{i=1}^N \beta_i \sin(\omega_i t + \xi_i)} \right\} \right) \quad (2.79)$$

$$= \frac{1}{2} \left(1 + \cos \left(\chi - \sum_{i=1}^N \beta_i \sin(\omega_i t + \xi_i) \right) \right) \quad (2.80)$$

Again, the period of the intensity is equal to the period of the applied field $B(t)$, i.e the inverse of the greatest common denominator ω_g of the occurring frequencies ω_i . The intensity can therefore be expanded in the Fourier series

$$I_O(x, t) = \sum_{m=-\infty}^{+\infty} c_m(x) e^{im\omega_g t} \quad (2.81)$$

2.2 Experimental verification

whose coefficients can be determined starting from eq.2.76.

$$\begin{aligned}
I_O(x, t) &= \frac{1}{2} \left(1 + \operatorname{Re} \left\{ e^{i\chi} \sum_{\vec{n}} J_{n_1}(\beta_1) \cdot \dots \cdot J_{n_N}(\beta_N) e^{-i\vec{n}(\vec{\xi} + \vec{\omega}t)} \right\} \right) \\
&= \frac{1}{2} \left(1 + \sum_{\vec{n}} J_{n_1}(\beta_1) \cdot \dots \cdot J_{n_N}(\beta_N) \cos(\chi - \vec{n}\vec{\xi} - \vec{\omega}\vec{n}t) \right) \\
&= |\{J_{n_i}\} \equiv J_{n_1}(\beta_1) \cdot \dots \cdot J_{n_N}(\beta_N)| = \\
&= \frac{1}{2} \left(1 + \sum_{\vec{n}} \{J_{n_i}\} \frac{1}{2} (e^{i(\chi - \vec{n}\vec{\xi} - \vec{\omega}\vec{n}t)} + e^{i(-\chi + \vec{n}\vec{\xi} + \vec{\omega}\vec{n}t)}) \right) \\
&= \frac{1}{2} \left(1 + \frac{1}{2} \sum_{\vec{n}} \{J_{n_i}\} e^{i(\chi - \vec{n}\vec{\xi} - \vec{\omega}\vec{n}t)} + \{J_{n_i}\} e^{i(-\chi + \vec{n}\vec{\xi} + \vec{\omega}\vec{n}t)} \right) \\
&= \frac{1}{2} \left(1 + \frac{1}{2} \sum_{\vec{n}} \{J_{-n_i}\} e^{i(\chi + \vec{n}\vec{\xi} + \vec{\omega}\vec{n}t)} + \{J_{n_i}\} e^{i(-\chi + \vec{n}\vec{\xi} + \vec{\omega}\vec{n}t)} \right) \\
&= \frac{1}{2} \left(1 + \frac{1}{2} \sum_{\vec{n}} \{J_{n_i}\} ((-1)^{\sum_i n_i} e^{i\chi} + e^{-i\chi}) e^{i\vec{n}\vec{\xi}} e^{i\vec{\omega}\vec{n}t} \right)
\end{aligned}$$

Comparison with the general expression for the Fourier transformation gives for $m \neq 0$

$$c_m = \frac{1}{4} \sum_{\vec{n}; \vec{n}\vec{\omega} = m\omega_g} J_{n_1}(\beta_1) \cdot \dots \cdot J_{n_N}(\beta_N) ((-1)^{\sum_i n_i} e^{i\chi} + e^{-i\chi}) e^{i\vec{n}\vec{\xi}} \quad (2.82)$$

The summations runs over all combinations of n_i 's where the equality $\vec{n}\vec{\omega} = m\omega_g$ holds. For $m = 0$, the result has to be modified

$$c_0 = \frac{1}{2} + \frac{1}{4} \sum_{\vec{n}; \vec{n}\vec{\omega} = 0} J_{n_1}(\beta_1) \cdot \dots \cdot J_{n_N}(\beta_N) ((-1)^{\sum_i n_i} e^{i\chi} + e^{-i\chi}) e^{i\vec{n}\vec{\xi}} \quad (2.83)$$

In either case, the summand given by a certain combination of n_i 's can be written as

$$2J_{n_1}(\beta_1) \cdot \dots \cdot J_{n_N}(\beta_N) e^{i\vec{n}\vec{\xi}} \cos \chi, \quad \text{if } \sum_i n_i \text{ even} \quad (2.84)$$

$$-2iJ_{n_1}(\beta_1) \cdot \dots \cdot J_{n_N}(\beta_N) e^{i\vec{n}\vec{\xi}} \sin \chi, \quad \text{if } \sum_i n_i \text{ odd} \quad (2.85)$$

To illustrate the general expressions, we will discuss the Fourier expansion of the intensities actually measured for 2-, 3- and 5-mode fields in detail.

2. ENERGY EXCHANGE IN A TIME-DEPENDENT MAGNETIC FIELD

Before, we want to investigate the dependence of the interference pattern from the occurring parameters χ, β_1, ξ_1 and ω_1 in the single-mode field case and thus start from eq.2.66.

$$I_O(x, t) = \frac{1}{2} (1 + \cos(\chi - \beta_1 \sin(\omega_1 t + \xi_1))) \quad (2.86)$$

with

$$\beta_1 = 2\alpha_1 \sin \frac{\omega_1 T}{2}, \quad \xi_1 = \varphi_1 + \frac{\omega_1 T + \pi}{2} - \frac{\omega_1}{v_0} x, \quad v_0 = \hbar k_0 / m \quad (2.87)$$

At first, we vary the phase shifter angle χ for the following neutron and field parameters

$$v_0 = 2060.43 \text{ m/s } (\lambda = 1.92 \text{ \AA}), \quad B_1 = 20 \text{ Gauss}, \\ \omega_1 = 1 \text{ kHz}, \quad T = L/v_0 = 19.4 \mu\text{s}$$

The position coordinate x is fixed, determined by the distance between third interferometer plate and detector. We choose the phase of the magnetic field φ_1 so, that $\xi_1 = \pi$. It can be seen in figs.2.5 and 2.6 that the intensity changes considerably for different values of χ , but the transition amplitudes are unaffected because they are obtained by dividing the Fourier components with $\sin \chi$ and $\cos \chi$ respectively (see eqs.2.70, 2.69). In [SHK⁺1995], various χ -values, i.e. phase shifter positions are used to determine possible experimental differences between emission and absorption amplitudes for the same energy amount.

Changing the phase ξ_1 only causes a shift of the intensity and varying ω_1 mainly rescales the curve on the abscissa. As far as the transition amplitudes are concerned, a variation of the field amplitude B_1 corresponding to a change of β_1 being proportional to B_1 is the most interesting case. With increasing field strength, the interference pattern gets a more and more wiggles. That means that Fourier components belonging to higher frequencies increase as well what goes hand in hand with a higher probability of exchanges of larger amounts of energy between the neutron and the magnetic field. We depict the characteristics of the intensity pattern for $B_1 = 0 - 45$ Gauss ($\chi = \pi/4$, $\omega_1 = 1$ kHz, $\xi_1 = 0$) and the corresponding Fourier transformation in fig.2.7.

If we plot the modulus of a Fourier component belonging to a certain frequency for increasing field strength the Bessel function characteristics becomes visible as predicted by eqs.2.68 - 2.70 (see fig.2.8).

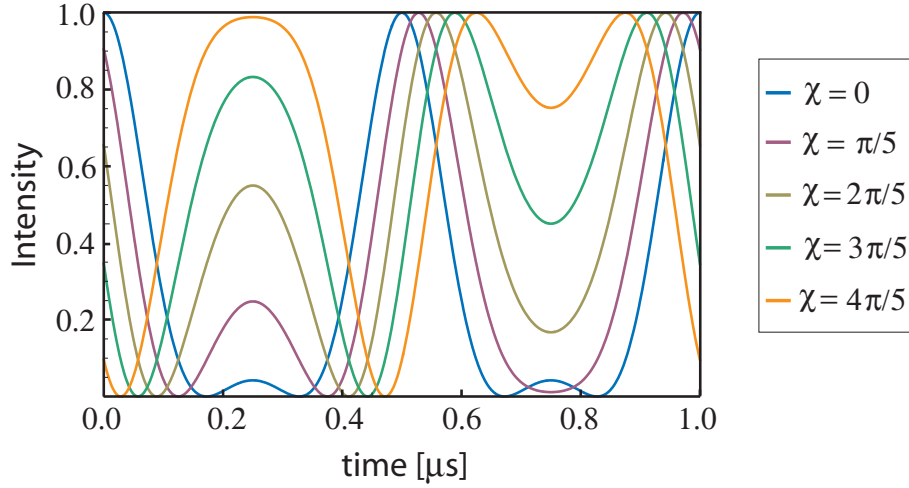


Figure 2.5: The time resolved intensity pattern between ψ_I and ψ_{III} when a single-mode field with $\omega_1 = 1\text{kHz}$, $\xi = \pi$ and $B_1 = 20\text{Gauss}$ is applied for different phase shifter values $\chi = 0 - 4\pi/5$.

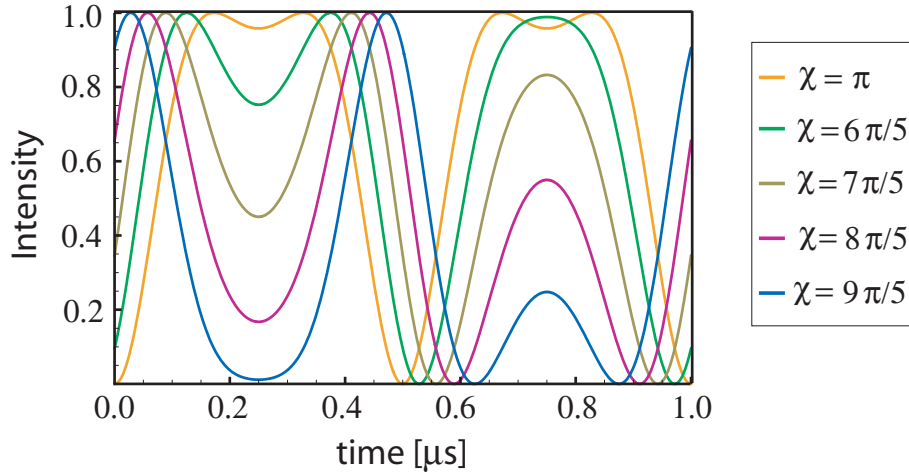


Figure 2.6: The time resolved intensity pattern between ψ_I and ψ_{III} when a single-mode field with $\omega_1 = 1\text{kHz}$, $\xi = \pi$ and $B_1 = 20\text{Gauss}$ is applied for phase shifter values $\chi = \pi - 9\pi/5$.

2. ENERGY EXCHANGE IN A TIME-DEPENDENT MAGNETIC FIELD

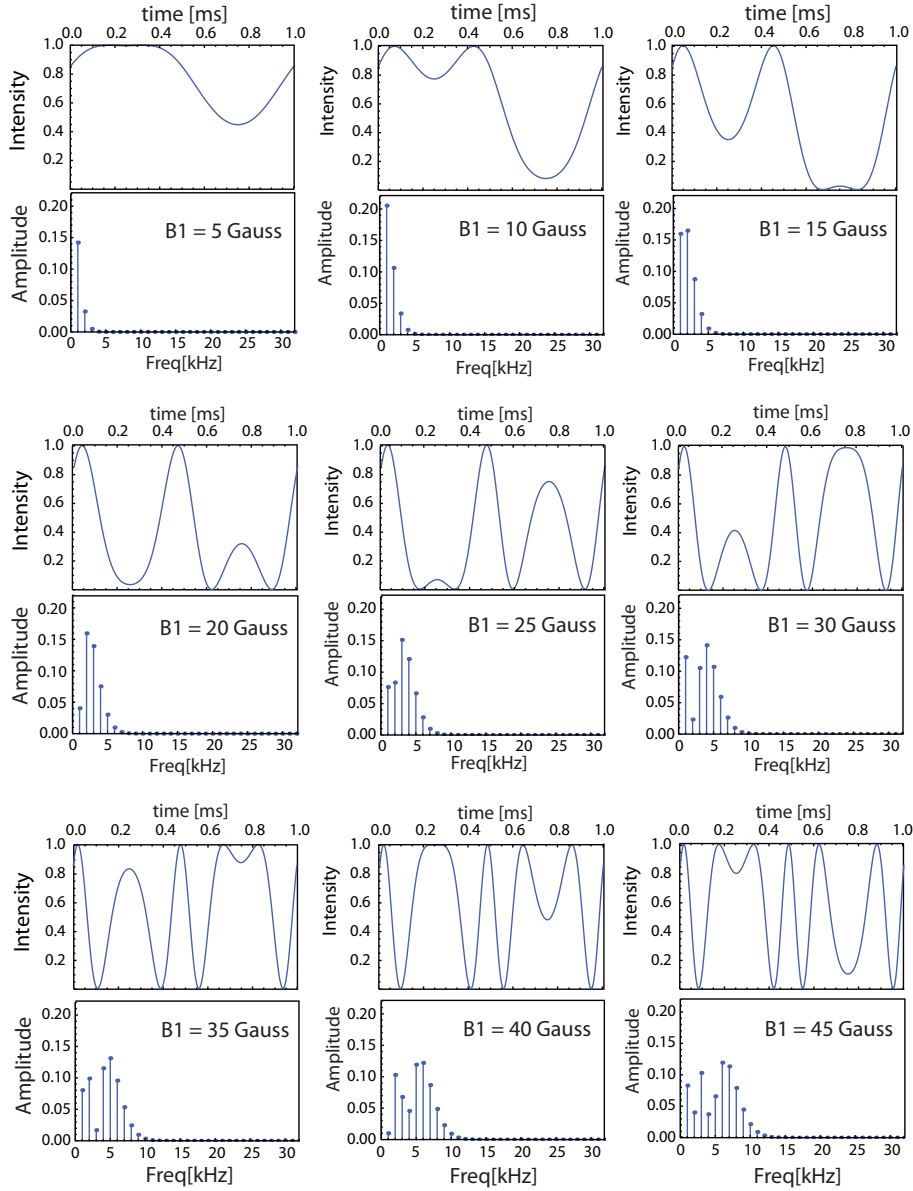


Figure 2.7: The time-dependent intensity pattern in the O-beam when a single-mode field is applied in one interferometer arm ($\omega_1 = 1\text{kHz}$, $\xi = \pi$ and $\chi = \pi/4$) with the corresponding Fourier transform. The field amplitude is varied from 0–45 Gauss showing an increase of Fourier components belonging to higher frequencies, i.e. higher amounts of energy have been transferred between neutron and field.

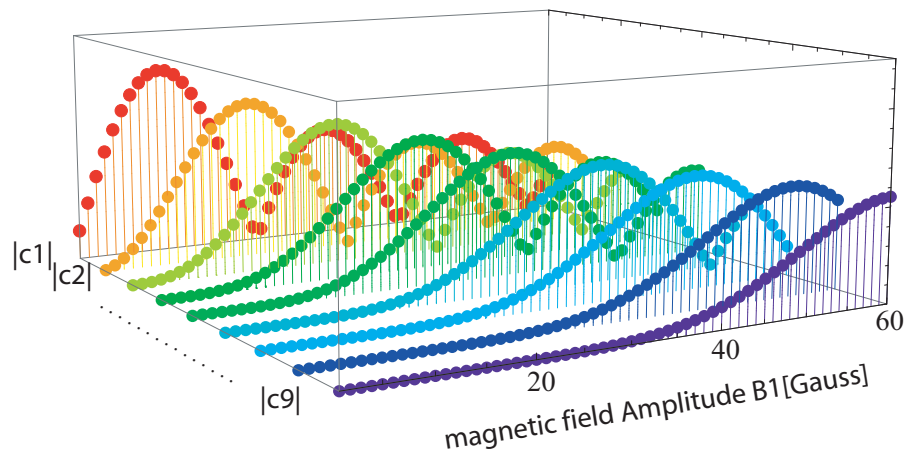


Figure 2.8: Modulus of some Fourier components (c_n is the Fourier component belonging to $(n\hbar\omega_1)$) plotted against the amplitude B_1 of the magnetic field.

2. ENERGY EXCHANGE IN A TIME-DEPENDENT MAGNETIC FIELD

2.2.2 Unpolarized neutrons

It is possible to reduce the effect of the phase shift χ on the form of the intensity pattern (see figs.2.5 and 2.6) by using unpolarized neutrons in the experiment. In this case, the measured intensity results from adding the intensities for the up and down polarized neutrons respectively (the unpolarized neutron beam can always be understood as an incoherent superposition of two beams polarized in opposite direction). The intensity for the down-polarized case is obtained by replacing μ with $-\mu$, i.e. β with $-\beta$ (see calculation in sec.2.1). We start from eq.2.66 to obtain the most compact form for the intensity

$$I_O^{unpol} = \frac{1}{2} (I_O^\uparrow + I_O^\downarrow) \quad (2.88)$$

$$\begin{aligned} &= \frac{1}{4} (1 + \cos(\chi - \beta_1 \sin(\dots))) + \frac{1}{4} (1 + \cos(\chi + \beta_1 \sin(\dots))) \\ &= \frac{1}{2} (1 + \cos \chi \cos(\beta_1 \sin(\omega_1 t + \xi_1))) \end{aligned} \quad (2.89)$$

where we used the addition theorem

$$\cos(\alpha \pm \beta) = \cos \alpha \cos \beta \mp \sin \alpha \sin \beta$$

A change of the interferometer phase χ now only shrinks or expands and mirrors the whole intensity pattern. In addition, near $\chi = 0$ and $\chi = \pi$ the cosine is very smooth and thus, fluctuations of χ have a little effect on the form of the intensity (see fig.2.9). The cosine is an even function and also 2π -periodic and $\cos(x) = \cos(2\pi - x)$ is valid. Therefore, the plots for χ ranging from $\pi - 2\pi$ look the same as the ones for χ ranging from $\pi - 0$.

The intensity patterns for increasing field strengths will be shown in the next section together with the measured points.

Another important difference to the case of polarized neutron can be seen from the Fourier transformation of eq.2.88. Therefore, we rewrite eq.2.89 with the help of the relation

$$\cos(\alpha \sin(\beta)) = \sum_{n=-\infty}^{+\infty} J_{2n}(\alpha) e^{2in\beta} \quad (2.90)$$

giving

$$I_O^{unpol} = \frac{1}{2} \left(1 + \cos \chi \sum_{n=-\infty}^{+\infty} J_{2n}(\beta_1) e^{2in\xi_1} e^{2in\omega_1 t} \right) \quad (2.91)$$

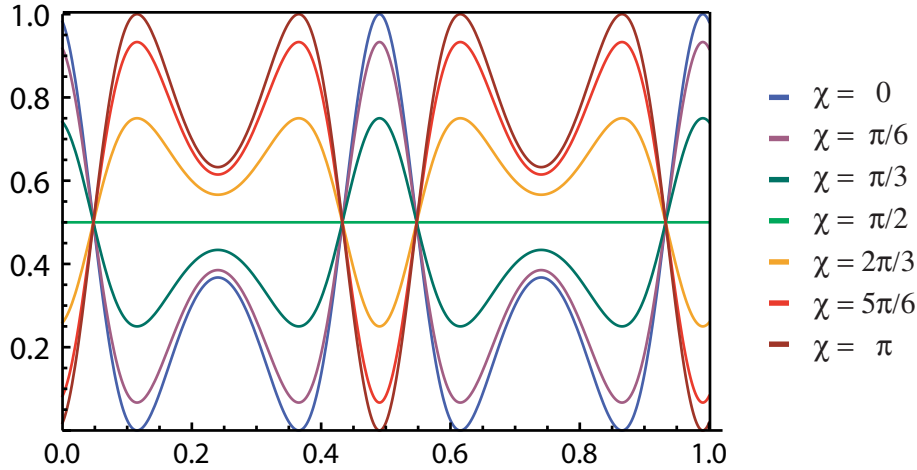


Figure 2.9: The time-resolved intensity pattern in case of unpolarized neutrons for different phase shifter values χ when a single-mode field with $\omega_1 = 1\text{kHz}$, $\xi = \pi$ and $B_1 = 20\text{Gauss}$ is applied.

from which we deduce the Fourier coefficients

$$c_0 = \frac{1}{2} (1 + J_0(\beta_1) \cos \chi) \quad (2.92)$$

$$c_{2n} = \frac{1}{2} e^{i2n\xi_1} J_{2n}(\beta_1) \cos \chi \quad (2.93)$$

$$c_{2n+1} = 0 \quad (2.94)$$

One can see that the even Fourier components vanish (this could already be assumed from the periodicity of the intensity in fig.2.9). As a consequence, we can also only deduce the transition amplitudes for even multiples of $\hbar\omega_1$ from the time-resolved intensity pattern. This is a bit unsatisfying, but, as we will see later, for fields with more modes the restrictions are more complex, so that the use of unpolarized neutrons to verify the theoretical calculations of sec.2.1 is justified. Using unpolarized neutrons, we don't need the guide field B_0 as well which has anyway no influence on the transition amplitudes.

For the arbitrary periodic field we have to insert eq.2.80 into eq.2.88 yielding

$$I_O^{unpol} = \frac{1}{2} \left(1 + \cos \chi \cos \left(\sum_{i=1}^N \beta_i \sin(\omega_i t + \xi_i) \right) \right) \quad (2.95)$$

To get the Fourier coefficient in the case of unpolarized neutrons for an arbitrary

2. ENERGY EXCHANGE IN A TIME-DEPENDENT MAGNETIC FIELD

periodic field, we add the Fourier coefficients of the up- and down-polarized case

$$I_O^{unpol} = \frac{1}{2} (I_O^\uparrow + I_O^\downarrow) \quad (2.96)$$

$$\sum_{m=-\infty}^{+\infty} c_m^{unpol} e^{im\omega_g} = \frac{1}{2} \left(\sum_{m=-\infty}^{+\infty} c_m^\uparrow e^{im\omega_g} + \sum_{m=-\infty}^{+\infty} c_m^\downarrow e^{im\omega_g} \right) \quad (2.97)$$

$$\implies c_m^{unpol} = \frac{1}{2} (c_m^\uparrow + c_m^\downarrow) \quad (2.98)$$

The up-polarized case (c_m^\uparrow) is given by eq.2.82, the down-polarized version (c_m^\downarrow) is obtained by replacing μ with $-\mu$, i.e. β with $-\beta$ resulting in $J_n(\beta) \rightarrow J_n(-\beta) = (-1)^n J_n(\beta)$.

$$c_m^\downarrow = \frac{1}{4} \sum_{\vec{n}; \vec{n}\vec{\omega} = m\omega_g} \{J_{-n_i}\} ((-1)^{\sum_i n_i} e^{i\chi} + e^{-i\chi}) e^{i\vec{n}\vec{\xi}} \quad (2.99)$$

$$c_m^{unpol} = \frac{1}{8} \sum_{\vec{n}; \vec{n}\vec{\omega} = m\omega_g} (\{J_{n_i}\} + \{J_{-n_i}\}) ((-1)^{\sum_i n_i} e^{i\chi} + e^{-i\chi}) e^{i\vec{n}\vec{\xi}} \quad (2.100)$$

The terms in the sum can be further evaluated

$$\begin{aligned} & (\{J_{n_i}\} + \{J_{-n_i}\}) ((-1)^{\sum_i n_i} e^{i\chi} + e^{-i\chi}) = \\ & = \{J_{n_i}\} (1 + (-1)^{\sum_i n_i}) ((-1)^{\sum_i n_i} e^{i\chi} + e^{-i\chi}) = \\ & = \{J_{n_i}\} (((-1)^{\sum_i n_i} + (-1)^{2\sum_i n_i}) e^{i\chi} + (1 + (-1)^{\sum_i n_i}) e^{-i\chi}) = \\ & = \{J_{n_i}\} (((-1)^{\sum_i n_i} + 1) e^{i\chi} + (1 + (-1)^{\sum_i n_i}) e^{-i\chi}) = \\ & = 4\{J_{n_i}\} \cos \chi, \quad \text{if } \sum_i n_i \text{ even} \\ & 0, \quad \text{if } \sum_i n_i \text{ odd} \end{aligned}$$

giving for the Fourier coefficient

$$c_m^{unpol} = \frac{1}{2} \sum_{\substack{\vec{n}; \vec{n}\vec{\omega} = m\omega_g \\ \sum_i n_i \text{ even}}} J_{n_1}(\beta_1) \cdots J_{n_N}(\beta_N) \cos \chi e^{i\vec{n}\vec{\xi}} \quad (2.101)$$

The special case for $m = 0$ the is given by

$$c_0^{unpol} = \frac{1}{2} + \frac{1}{2} \sum_{\substack{\vec{n}; \vec{n}\vec{\omega} = 0 \\ \sum_i n_i \text{ even}}} J_{n_1}(\beta_1) \cdots J_{n_N}(\beta_N) \cos \chi e^{i\vec{n}\vec{\xi}} \quad (2.102)$$

2.3 Experimental results

Now, after having highlighted the connection between the theoretical calculations and the experimental demonstration, we want to turn to the actual measurements. All experiments described here have been performed at the S18 neutron interferometry setup at the high-flux reactor of the Institute Laue-Langevin in Grenoble, France. A silicon perfect crystal monochromator is placed behind a neutron guide to extract neutrons of mean wavelength $\lambda = 1.92 \text{ \AA}$ ($\delta\lambda/\lambda \simeq 0.01$) and a beam cross section of $6 \times 8 \text{ mm}$. The neutrons impinge on the skew-symmetric silicon interferometer under an angle of 30° and the Bragg-condition is fulfilled for the 220-lattice planes. In one arm of the interferometer, a water-cooled AC-coil is placed to generate the rectangular, time-dependent magnetic field. Using unpolarized neutrons, no guide field is needed.

2.3.1 Single mode magnetic field

In the first experiment, the magnetic field contains only one frequency ($\omega_1 = 1\text{kHz}$). This case has already been measured in [SHK+1995] with polarized neutrons. We did all experiments with unpolarized neutrons.

To get the time-resolved interference pattern one synchronizes a counter with the signal period, i.e. 1ms, which is equal to the period of the intensity. This time interval is further divided into 64 channels in which the neutrons are sorted according to their detection time. After a full period the counter is reset to zero. By applying this procedure, the time dependent interference pattern is obtained. Counting and synchronisation were performed with the help of a National Instruments FPGA card (NI PXI-7842R). The time resolution is limited by the detector (He3 under 5 bar) and is given by $\sim 140\text{kHz}$. In figs.2.10 - 2.17 one can see the time-resolved interference pattern for various amplitudes of the oscillating field.

The fit functions used in figs.2.10 - 2.17 are obtained from eq.2.89 by additionally taking background intensity $u = a - b$ and reduced contrast $c = b/a$ into account

$$I_O(x = x_{\text{det}}, t) = a + b \cos(\alpha_1 \sin(\omega_1 t + \gamma_1)) \quad (2.103)$$

Although all its contributions are measurable in principal, the phase ξ_1 has also become a fit parameter called γ_1 because of the unknown exact detector position x_{det} and phase of the magnetic field. Note, that the signal generator only fixes the phase of the current. The $\cos \chi$ -factor is absorbed in the fit parameter b . In α_1 , we fix the value for $T = L/v_0 \simeq 19, 4\mu\text{s}$ and use the field amplitude B_1 as fit parameter. Nevertheless its value has to be related to the field value measured with the gaussmeter. By subtracting the underground and dividing with $2b$, the intensity can be properly normed to lie between 0 and 1. The measured points

2. ENERGY EXCHANGE IN A TIME-DEPENDENT MAGNETIC FIELD

are normed as well and then, their discrete Fourier transformation allows the determination of the transition amplitudes.

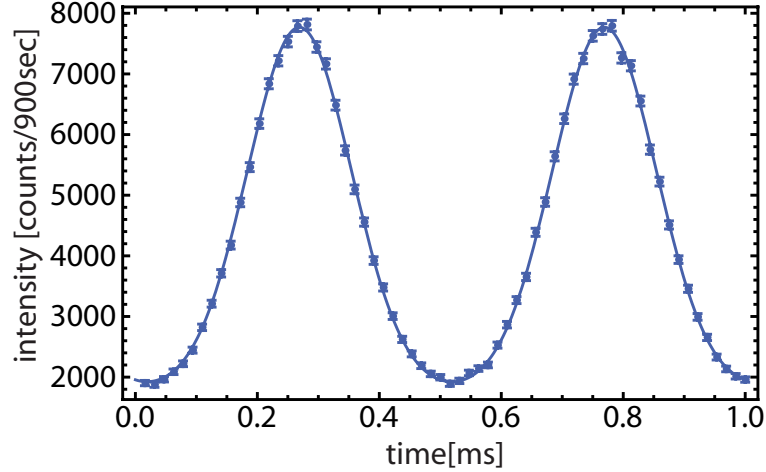


Figure 2.10: The time-resolved interference pattern for $B(t) = B_1 \cos \omega_1 t$ with frequency $\omega_1 = 2\pi \cdot 1\text{kHz}$ and amplitude $B_1 = 14\text{Gauss}$. The fit function is given by eq.2.103.

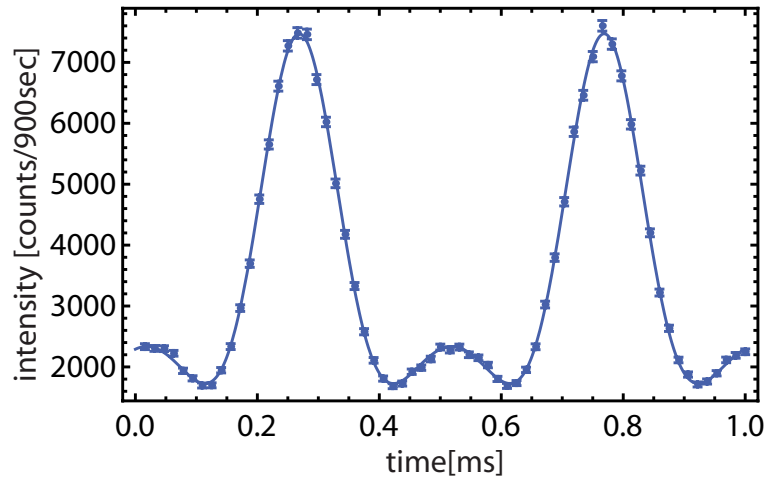


Figure 2.11: The time-resolved interference pattern for $B(t) = B_1 \cos \omega_1 t$ with $\omega_1 = 1\text{kHz}$ and $B_1 = 20\text{Gauss}$. The fit function is given by eq.2.103.

As already pointed out, for unpolarized neutrons in a single-mode field, the intensity pattern only reveals the transition amplitudes belonging to even multiples $2n\hbar\omega_1$ (see (eq.2.93)), which are given in principle by the Bessel functions

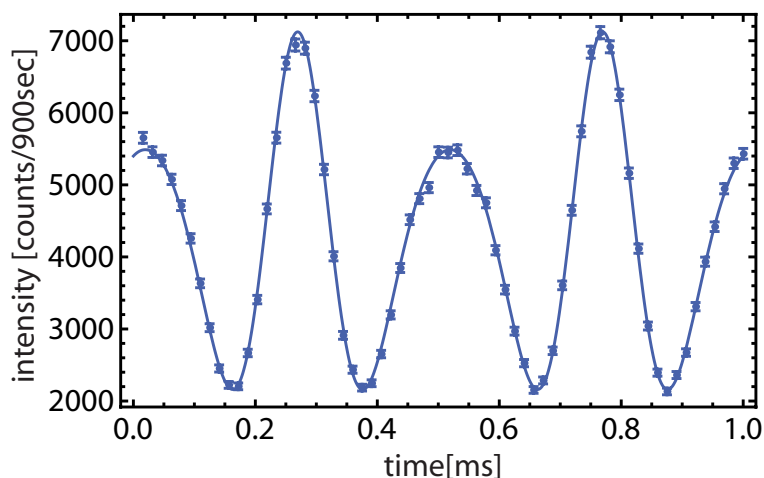


Figure 2.12: The time-resolved interference pattern if a magnetic field $B(t) = B_1 \cos \omega_1 t$ with $\omega_1 = 1\text{kHz}$ and $B_1 = 28\text{Gauss}$ is applied. The fit function is given by (eq.2.103).

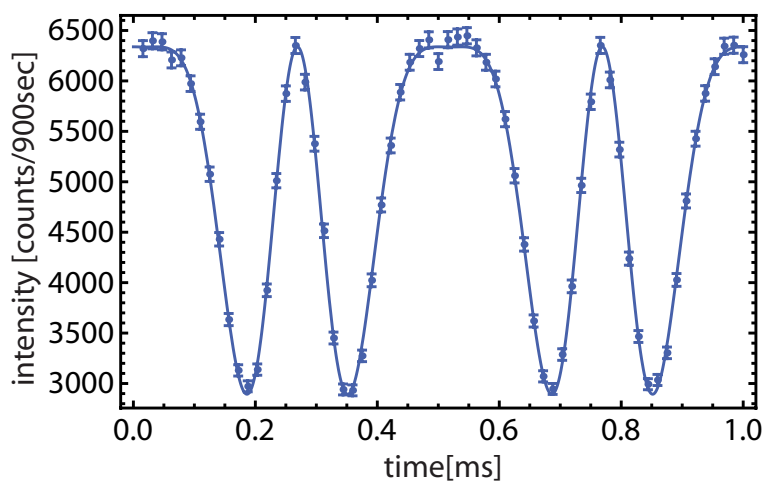


Figure 2.13: The time-resolved interference pattern if a magnetic field $B(t) = B_1 \cos \omega_1 t$ with $\omega_1 = 1\text{kHz}$ and $B_1 = 35\text{Gauss}$ is applied. The fit function is given by (eq.2.103).

$J_{2n}(\beta_1)$. Inserting the values of the known parameters, the argument of the Bessel functions explicitly reads

$$\beta_1 = 2 \frac{\mu B_1}{\hbar \omega_1} \sin \frac{\omega_1 T}{2} \simeq 1777.6 B_1$$

From the discrete Fourier transformation of the 64 measured (and normed) points,

2. ENERGY EXCHANGE IN A TIME-DEPENDENT MAGNETIC FIELD

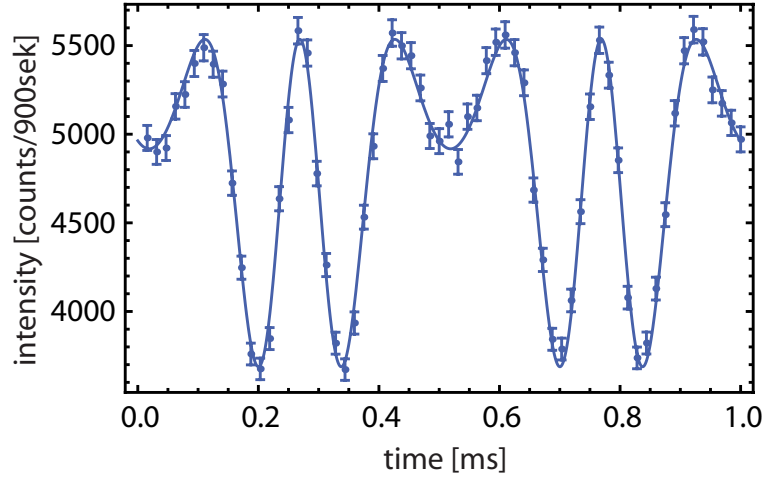


Figure 2.14: The time-resolved interference pattern for $B(t) = B_1 \cos \omega_1 t$ with $\omega_1 = 1\text{kHz}$ and $B_1 = 42\text{Gauss}$. The fit function is given by eq.2.103.

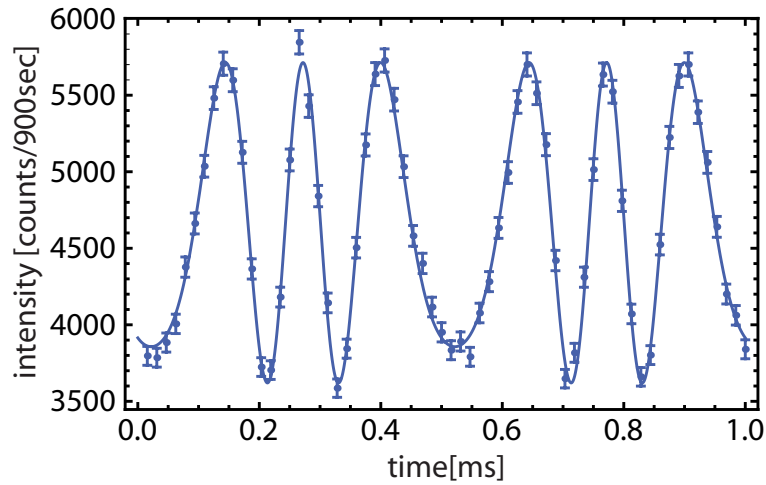


Figure 2.15: The time-resolved interference pattern if a magnetic field $B(t) = B_1 \cos \omega_1 t$ with $\omega_1 = 1\text{kHz}$ and $B_1 = 49\text{Gauss}$ is applied. The fit function is given by (eq.2.103).

one could in principle obtain Fourier coefficients belonging to the frequencies $0, 1, \dots, 31 \omega_1$, but for the maximally applied field strength of about $B_1 = 67$ Gauss only coefficients up to $16 \omega_1$ contribute (see fig.2.27). The even Fourier coefficients vanish and we depict the first one belonging to an energy exchange of $1 \cdot \hbar \omega_1$ (see fig.2.19). The transition amplitudes for emission and absorption of a certain amount of energy are equal, obeying energy conservation.

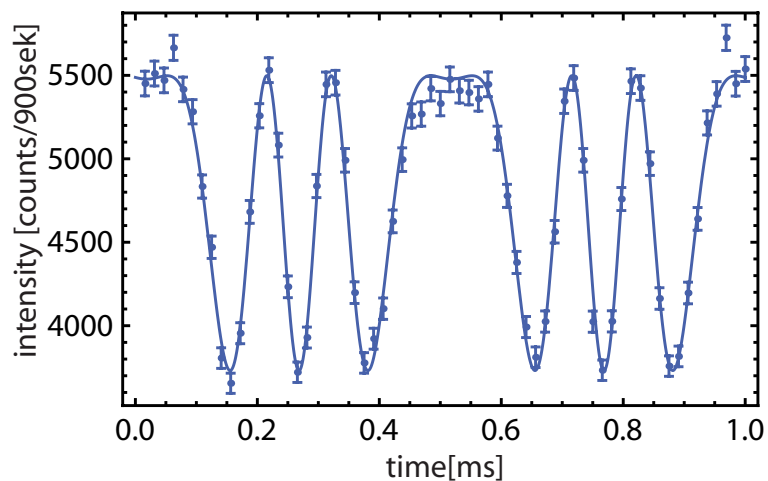


Figure 2.16: The time-resolved interference pattern if a magnetic field $B(t) = B_1 \cos \omega_1 t$ with $\omega_1 = 1\text{kHz}$ and $B_1 = 54\text{Gauss}$ is applied. The fit function is given by (eq.2.103).

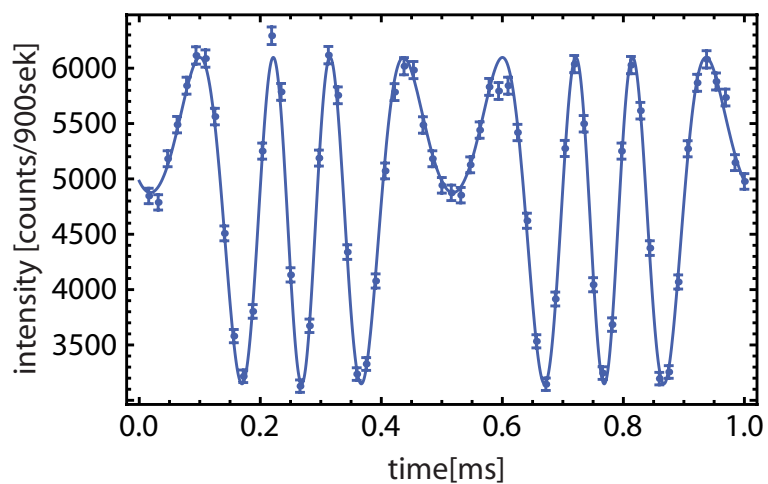


Figure 2.17: The time-resolved interference pattern for $B(t) = B_1 \cos \omega_1 t$ with $\omega_1 = 1\text{kHz}$ and $B_1 = 60\text{Gauss}$. The fit function is given by eq.2.103.

2. ENERGY EXCHANGE IN A TIME-DEPENDENT MAGNETIC FIELD

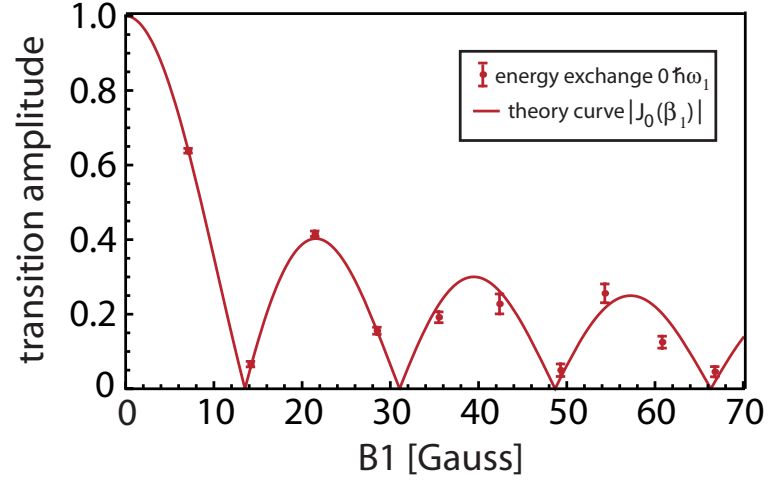


Figure 2.18: Transition amplitudes for an energy transfers of $0\hbar\omega_1$ as function of the field amplitude B_1 obtained by discrete Fourier transformation of the measured time-resolved interference patterns. The measured points are compared to the theoretical curve, i.e. Bessel functions $J_0(\beta_1) = J_0(1777.6B_1)$.

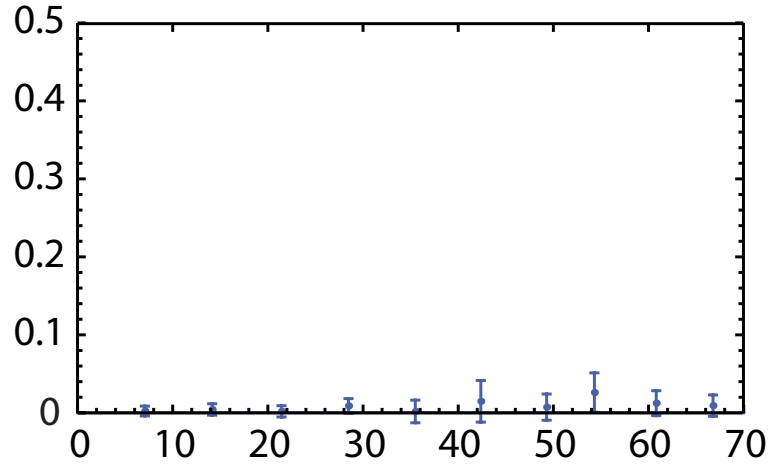


Figure 2.19: The Fourier component belonging to $1 \cdot \hbar\omega_1$ vanishes for all field strengths. The same holds for all even coefficients.

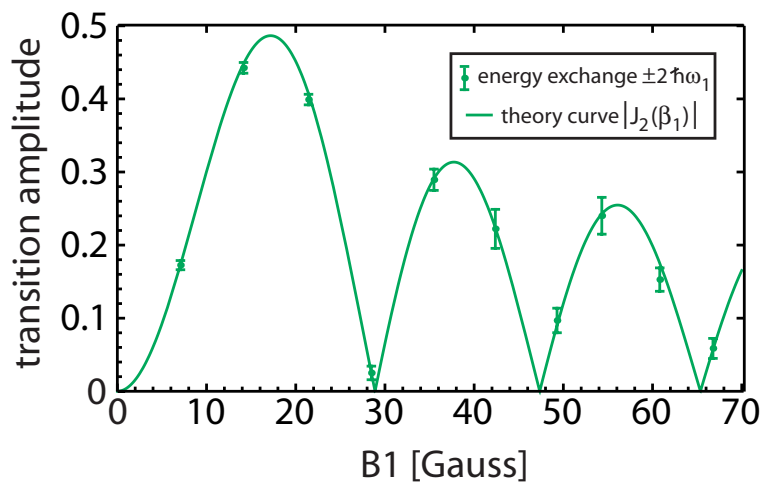


Figure 2.20: Transition amplitudes for an energy transfers of $2\hbar\omega_1$ as function of the field amplitude B_1 obtained by discrete Fourier transformation of the measured time-resolved interference patterns. The measured points are compared to the theoretical curve, i.e. Bessel functions $J_2(\beta_1) = J_2(1777.6B_1)$.

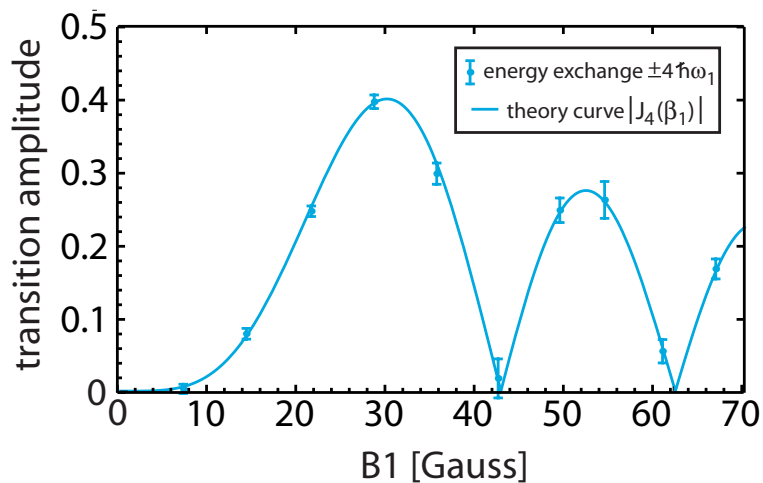


Figure 2.21: Transition amplitudes for an energy transfers of $4\hbar\omega_1$ as function of the field amplitude B_1 obtained by discrete Fourier transformation of the measured time-resolved interference patterns. The measured points are compared to the theoretical curve, i.e. Bessel functions $J_4(\beta_1) = J_4(1777.6B_1)$.

2. ENERGY EXCHANGE IN A TIME-DEPENDENT MAGNETIC FIELD

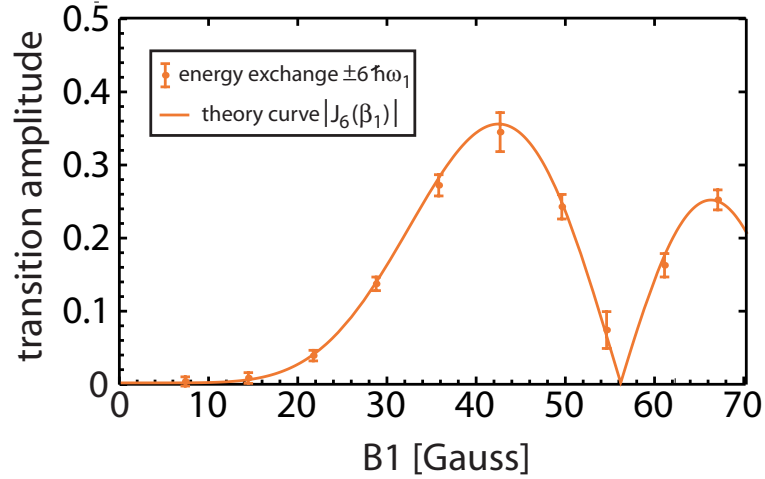


Figure 2.22: Transition amplitudes for an energy transfers of $6\hbar\omega_1$ as function of the field amplitude B_1 obtained by discrete Fourier transformation of the measured time-resolved interference patterns. The measured points are compared to the theoretical curve, i.e. Bessel functions $J_6(\beta_1) = J_6(1777.6B_1)$.

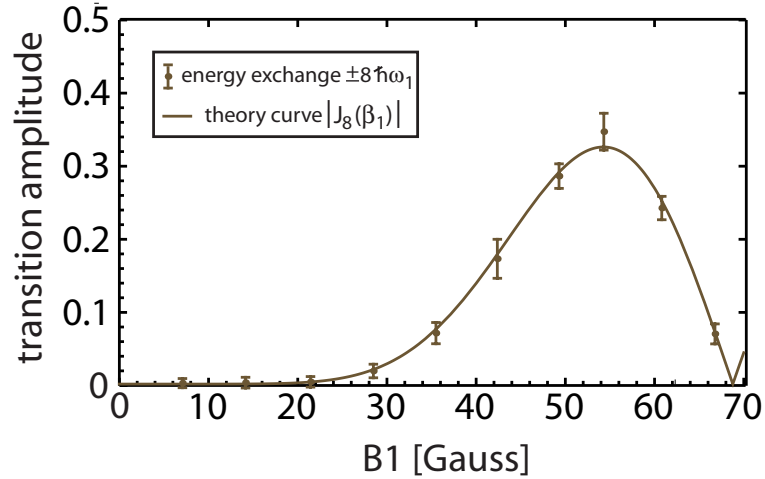


Figure 2.23: Transition amplitudes for an energy transfers of $8\hbar\omega_1$ as function of the field amplitude B_1 obtained by discrete Fourier transformation of the measured time-resolved interference patterns. The measured points are compared to the theoretical curve, i.e. Bessel functions $J_8(\beta_1) = J_8(1777.6B_1)$.

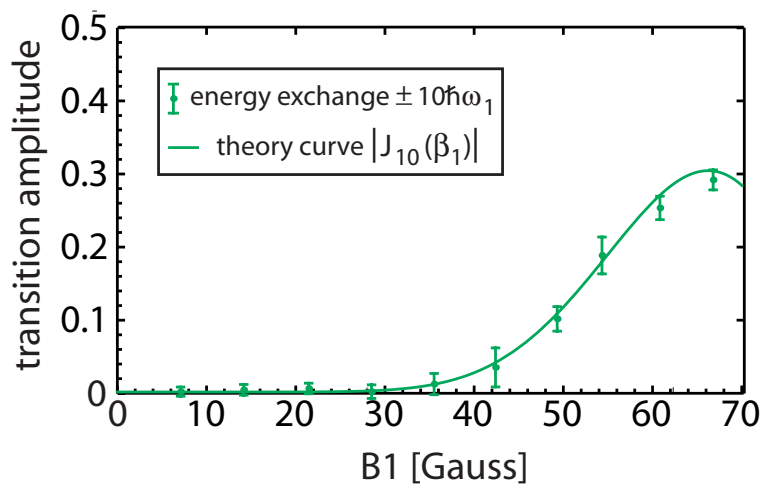


Figure 2.24: Transition amplitudes for an energy transfers of $10\hbar\omega_1$ as function of the field amplitude B_1 obtained by discrete Fourier transformation of the measured time-resolved interference patterns. The measured points are compared to the theoretical curve, i.e. Bessel functions $J_{10}(\beta_1) = J_{10}(1777.6B_1)$.

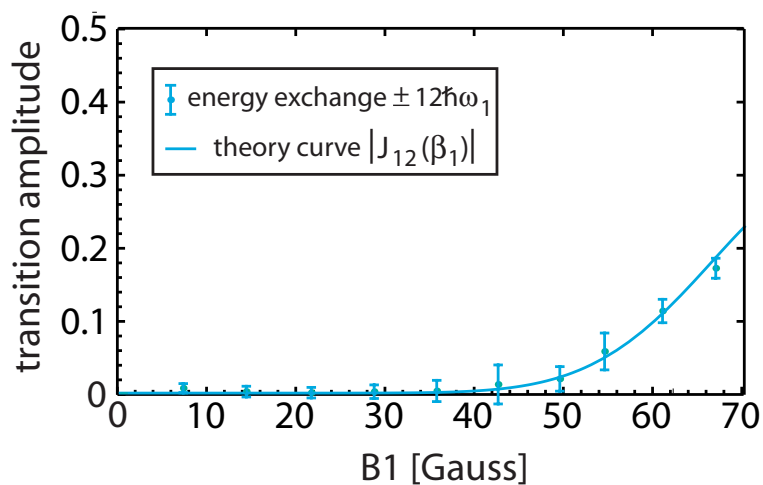


Figure 2.25: Transition amplitudes for an energy transfers of $12\hbar\omega_1$ as function of the field amplitude B_1 obtained by discrete Fourier transformation of the measured time-resolved interference patterns. The measured points are compared to the theoretical curve, i.e. Bessel functions $J_{12}(\beta_1) = J_{12}(1777.6B_1)$.

2. ENERGY EXCHANGE IN A TIME-DEPENDENT MAGNETIC FIELD

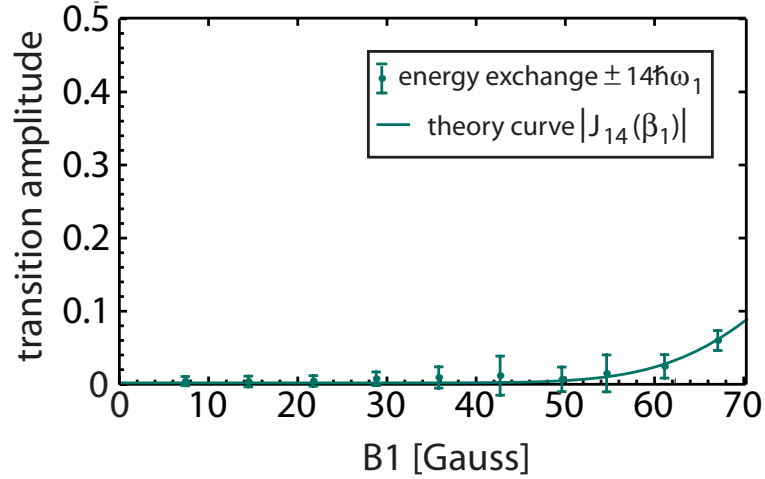


Figure 2.26: Transition amplitudes for an energy transfers of $14\hbar\omega_1$ as function of the field amplitude B_1 obtained by discrete Fourier transformation of the measured time-resolved interference patterns. The measured points are compared to the theoretical curve, i.e. Bessel functions $J_{14}(\beta_1) = J_{14}(1777.6B_1)$.

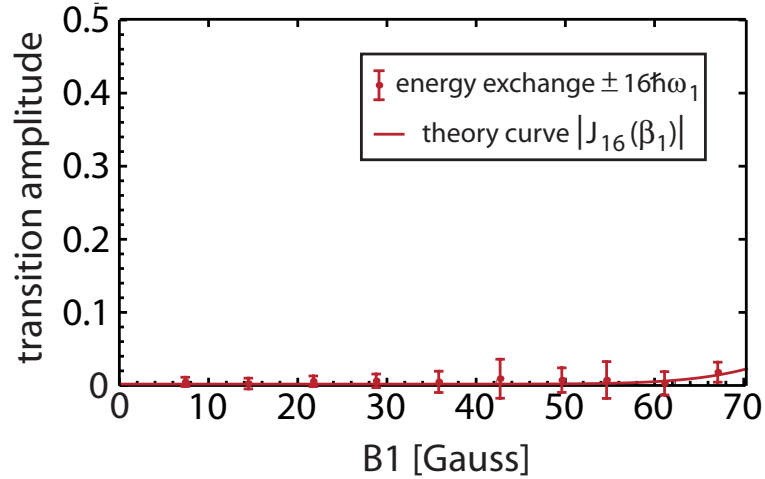


Figure 2.27: Transition amplitudes for an energy transfers of $16\hbar\omega_1$ as function of the field amplitude B_1 obtained by discrete Fourier transformation of the measured time-resolved interference patterns. The measured points are compared to the theoretical curve, i.e. Bessel functions $J_{16}(\beta_1) = J_{16}(1777.6B_1)$.

2.3.2 Magnetic field with two modes

Now we extend the experimental investigations by applying a magnetic field consisting of two modes in one arm of the interferometer.

$$B(t) = B_1 \cos(\omega_1 t + \varphi_1) + B_2 \cos(\omega_2 t + \varphi_2) \quad (2.104)$$

where $\omega_1 = 2\pi \cdot 2\text{kHz}$, $\omega_2 = 2\pi \cdot 3\text{kHz}$, $\varphi_1 = 0$ and $\varphi_2 = 2.55$. The period of this signal is given by the greatest common denominator $\omega_g = 2\pi \cdot 1\text{kHz}$ of the two frequencies ω_1 and ω_2 . Again we divide the period into 64 channels and record the time-resolved interference pattern for various field amplitudes, where $B_2 = 0.95B_1$ is always maintained (e.g. fig.2.28-2.29).

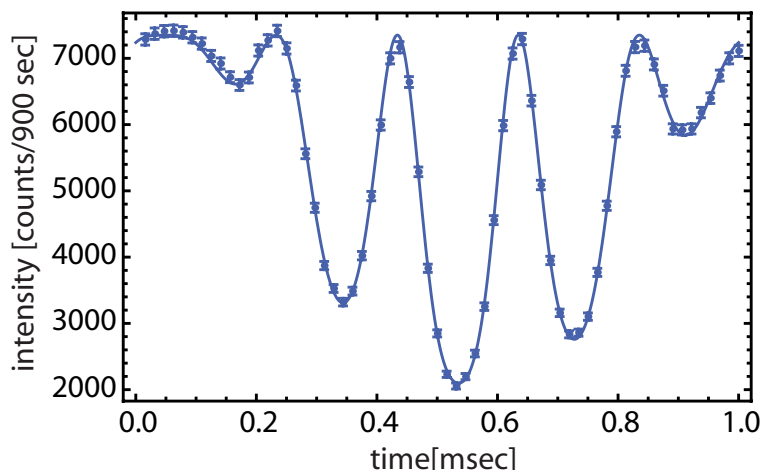


Figure 2.28: The time-resolved interference pattern when $B(t) = B_1 \cos(\omega_1 t) + B_2 \cos(\omega_2 t + 2.55)$ with $\omega_1 = 2\pi \cdot 2\text{kHz}$, $\omega_2 = 2\pi \cdot 3\text{kHz}$, $B_2 = 0.95B_1$ and $B_1 = 7.5$ Gauss is applied in one beam path. Full period ($=2\pi/\omega_g=1\text{ms}$) divided into 64 channels. The fit function is given by eq.2.105.

For higher amplitudes, the interference pattern gets more and more fine structures so that we increased the number of channels to 128 to resolve them (see fig.2.30-2.33).

The fit function for the intensity pattern when fields consisting of an arbitrary number N of modes are applied is deduced from (eq.2.95). For two modes it reads explicitly

$$I_O(x = x_{\text{det}}, t) = u + c \cos\left(\sum_{i=1}^2 \alpha_i \sin(\omega_i t + \gamma_i)\right) \quad (2.105)$$

In section 2.2, we have shown how the Fourier coefficients are related to the transition amplitudes. For this purpose, we have inserted the general solution

2. ENERGY EXCHANGE IN A TIME-DEPENDENT MAGNETIC FIELD

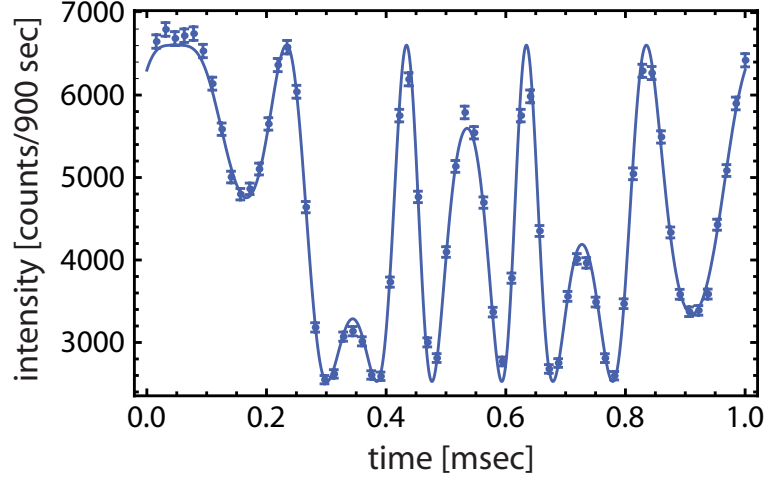


Figure 2.29: The time-resolved interference pattern for $B(t) = B_1 \cos(\omega_1 t) + B_2 \cos(\omega_2 t + 2.55)$ with $\omega_1 = 2\pi \cdot 2\text{kHz}$, $\omega_2 = 2\pi \cdot 3\text{kHz}$, $B_2 = 0.95B_1$ and $B_1 = 15$ Gauss. Full period ($2\pi/\omega_g=1\text{ms}$) divided into 64 channels. The fit function is given by eq.2.105.

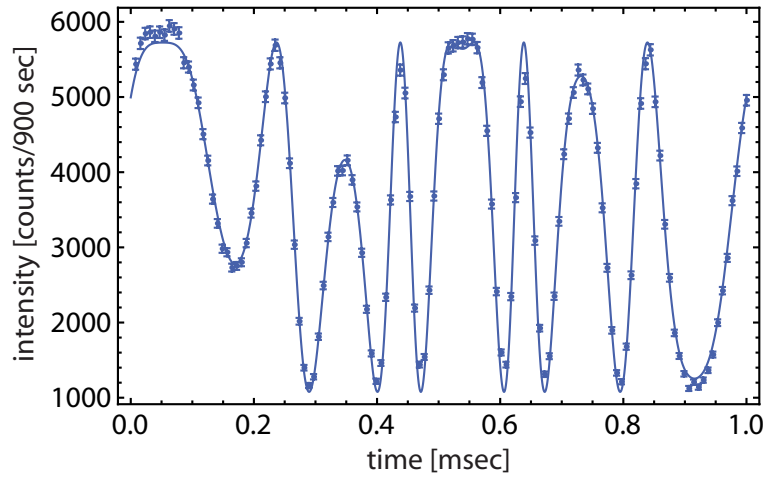


Figure 2.30: The time-resolved interference pattern for $B(t) = B_1 \cos(\omega_1 t) + B_2 \cos(\omega_2 t + 2.55)$ with $\omega_1 = 2\pi \cdot 22\text{kHz}$, $\omega_2 = 2\pi \cdot 23\text{kHz}$, $B_2 = 0.95B_1$ and $B_1 = 19\text{Gauss}$. Full period ($2\pi/\omega_g=1\text{ms}$) divided into 128 channels. The fit function is given by eq.2.105.

for ψ_{III} (eq.2.59) into the intensity formula (eq.2.62), then added intensities for up- and down-polarized neutrons and finally compared the expression with the ordinary Fourier transformation which gave for coefficient c_m , belonging to $e^{im\omega_g t}$,

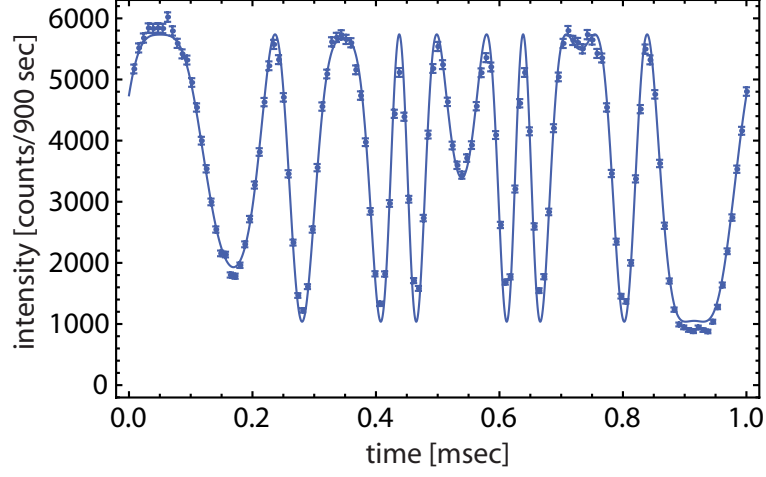


Figure 2.31: The time-resolved interference pattern for $B(t) = B_1 \cos(\omega_1 t) + B_2 \cos(\omega_2 t + 2.55)$ with $\omega_1 = 2\pi \cdot 22\text{kHz}$, $\omega_2 = 2\pi \cdot 23\text{kHz}$, $B_2 = 0.95B_1$ and $B_1 = 22.5\text{Gauss}$. Full period ($2\pi/\omega_g=1\text{ms}$) divided into 128 channels. The fit function is given by eq.2.105.

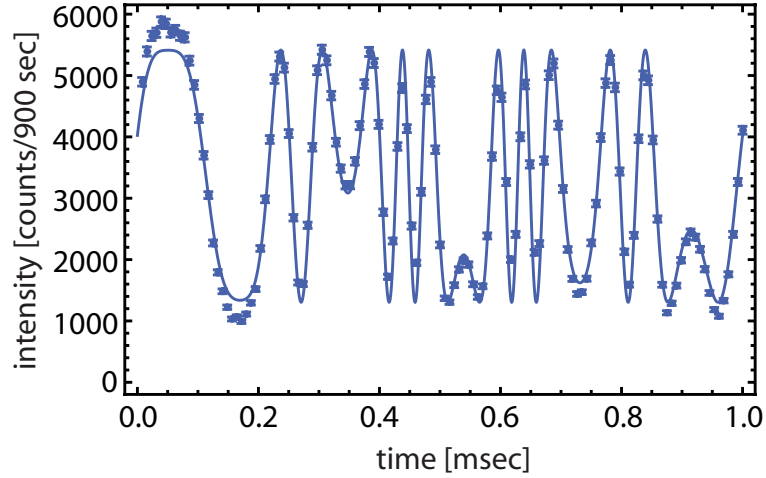


Figure 2.32: The time-resolved interference pattern for $B(t) = B_1 \cos(\omega_1 t) + B_2 \cos(\omega_2 t + 2.55)$ with $\omega_1 = 2\pi \cdot 22\text{kHz}$, $\omega_2 = 2\pi \cdot 23\text{kHz}$, $B_2 = 0.95B_1$ and $B_1 = 30\text{Gauss}$. Full period ($2\pi/\omega_g=1\text{ms}$) divided into 128 channels. The fit function is given by eq.2.105.

the expression (eq.2.101). For $N = 2$ it reads

$$c_m^{unpol} = \frac{1}{2}\delta_{m,0} + \frac{1}{2} \sum_{\substack{n_1, n_2 = -\infty \\ n_1 \omega_1 + n_2 \omega_2 = m \omega_g \\ n_1 + n_2 \text{ even}}}^{+\infty} J_{n_1}(\beta_1) J_{n_2}(\beta_2) \cos \chi e^{i(n_1 \xi_1 + n_2 \xi_2)}$$

2. ENERGY EXCHANGE IN A TIME-DEPENDENT MAGNETIC FIELD

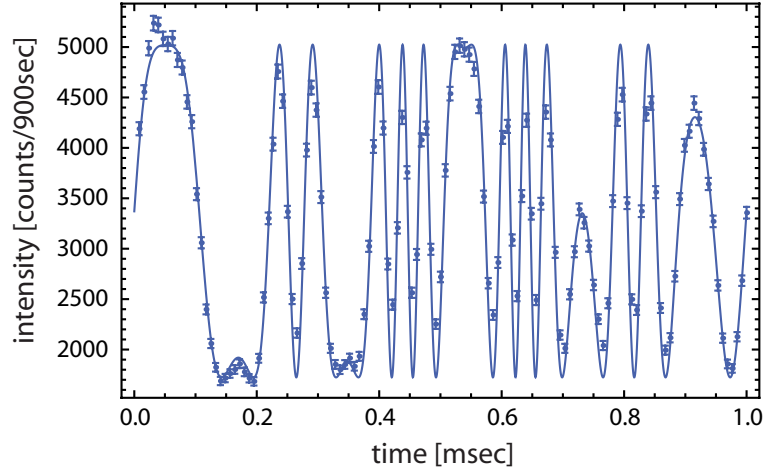


Figure 2.33: The time-resolved interference pattern for $B(t) = B_1 \cos(\omega_1 t) + B_2 \cos(\omega_2 t + 2.55)$ with $\omega_1 = 2\pi \cdot 2\text{kHz}$, $\omega_2 = 2\pi \cdot 23\text{kHz}$, $B_2 = 0.95B_1$ and $B_1 = 35\text{Gauss}$. Full period ($2\pi/\omega_g=1\text{ms}$) divided into 128 channels. The fit function is given by eq.2.105.

We can omit the $\cos \chi$ -term, because it has already been absorbed in the fit parameter b . Like in the $N = 1$ case, the phases ξ_i are now given by the fit phases γ_i and β_i is replaced by the fit parameter α_i . To illustrate this expression we want to perform the summation for special cases: For example, if we are interested in the case $m = 0$, we have

$$\begin{aligned}
 n_1\omega_1 + n_2\omega_2 &= 0 \cdot \omega_g \\
 0\omega_1 + 0\omega_2 &= 0 \quad , \quad 3\omega_1 - 2\omega_2 = 0 \quad , \\
 -3\omega_1 + 2\omega_2 &= 0 \quad , \quad 6\omega_1 - 4\omega_2 = 0 \quad , \dots
 \end{aligned}
 \tag{2.106}$$

Thus, from the first conditions to the summation we get the tuples

$$\begin{aligned}
 \{n_1, n_2\} &= \{(0, 0), (3, -2), (-3, 2), (6, -4), (-6, 4), (9, -6), (-9, 6), \dots\} \\
 &= \{(3j, -2j); j \in \mathbb{Z}\}
 \end{aligned}$$

The requirement, that $n_1 + n_2$ is even, is then fulfilled for every second of these tuples

$$\begin{aligned}
 \{n_1, n_2\} &= \{(0, 0), (6, -4), (-6, 4), (12, -8), (-12, 8), \dots\} \\
 &= \{(6j, -4j); j \in \mathbb{Z}\}
 \end{aligned}$$

Thus, to agree with theory, the measured Fourier coefficient c_0 should be given by

$$c_0 = \frac{1}{2} + \frac{1}{2} \sum_{j=-\infty}^{+\infty} J_{6j}(\alpha_1) J_{-4j}(\alpha_2) e^{i(6j\gamma_1 - 4j\gamma_2)} \quad (2.107)$$

$$= \frac{1}{2} + \frac{1}{2} \sum_{j=0}^{+\infty} (2 - \delta_{j,0}) J_{6j}(\alpha_1) J_{4j}(\alpha_2) \cos(6j\gamma_1 - 4j\gamma_2) \quad (2.108)$$

where we have splitted the sum, performed an index transformation ($j \rightarrow -j$) for the negative j 's, and then used the identity $J_{-n} = (-1)^n J_n$ for even n 's. Since we know that for the maximally applied field strengths of about 50 Gauss, the higher order Bessel functions vanish, we can restrict the summation to $j = -3, \dots, +3$. The measured Fourier coefficient c_0 is depicted in fig.2.34 and shows a very good agreement with the theory curve given by (eq.2.107).

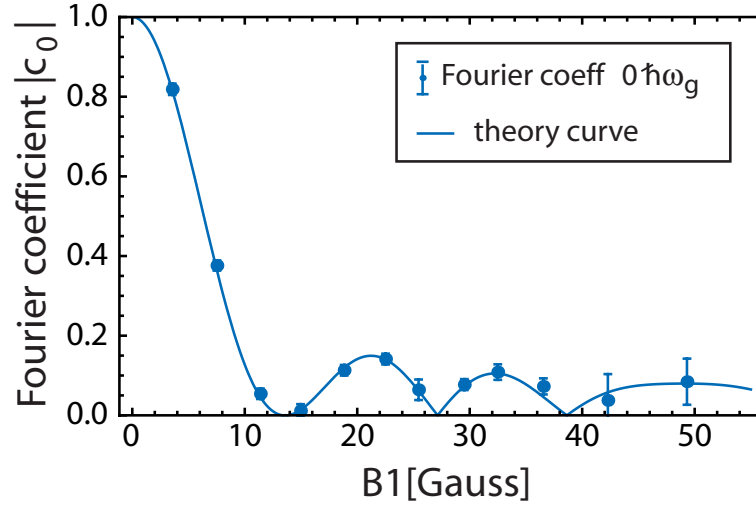


Figure 2.34: Fourier coefficient c_0 obtained by discrete Fourier transformation of the measured time-resolved interference patterns for the two mode magnetic field ($\omega_g = 1\text{kHz}$). The measured points are compared to the theoretical curve given by (eq.2.107).

In similar fashion, we calculate the theoretically expected curves for various Fourier coefficients and we can see that they all agree with the measured results (see fig.2.35-2.40).

2. ENERGY EXCHANGE IN A TIME-DEPENDENT MAGNETIC FIELD

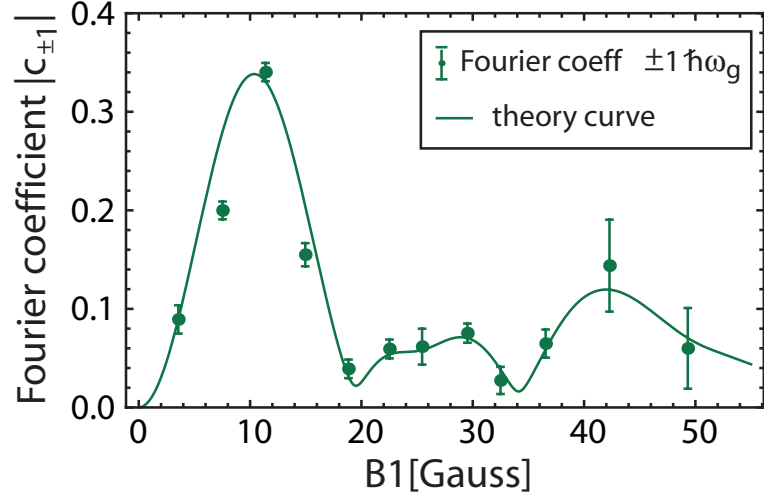


Figure 2.35: Fourier coefficient $c_{\pm 1}$ obtained by discrete Fourier transformation of the measured time-resolved interference patterns for the two mode magnetic field ($\omega_g = 1\text{kHz}$). The measured points are compared to the theoretical curve is deduced from (eq.2.101).

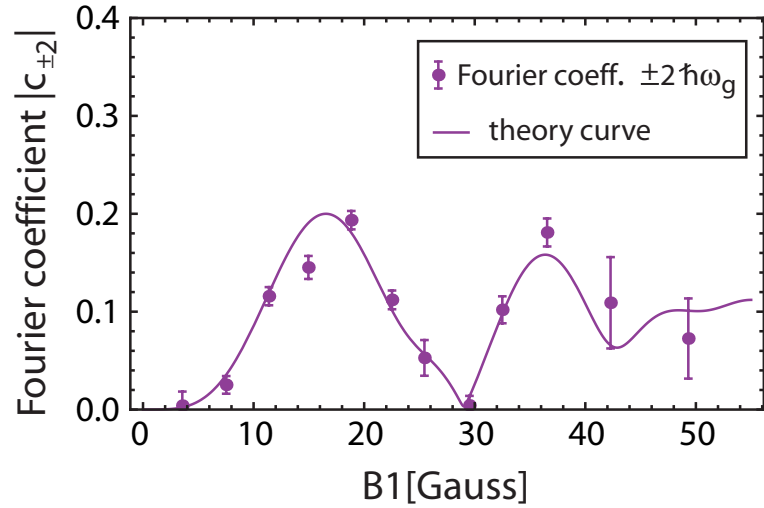


Figure 2.36: Fourier coefficient $c_{\pm 2}$ obtained by discrete Fourier transformation of the measured time-resolved interference patterns for the two mode magnetic field ($\omega_g = 1\text{kHz}$). The measured points are compared to the theoretical curve is deduced from (eq.2.101).

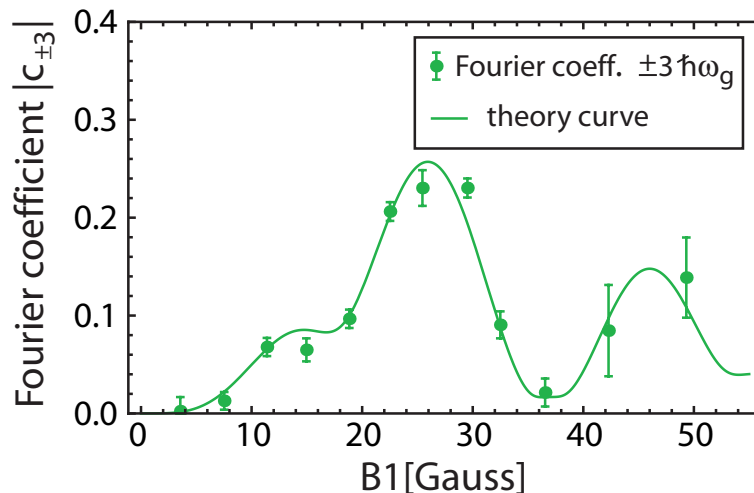


Figure 2.37: Fourier coefficient $c_{\pm 3}$ obtained by discrete Fourier transformation of the measured time-resolved interference patterns for the two mode magnetic field ($\omega_g = 1\text{kHz}$). The measured points are compared to the theoretical curve is deduced from (eq.2.101).

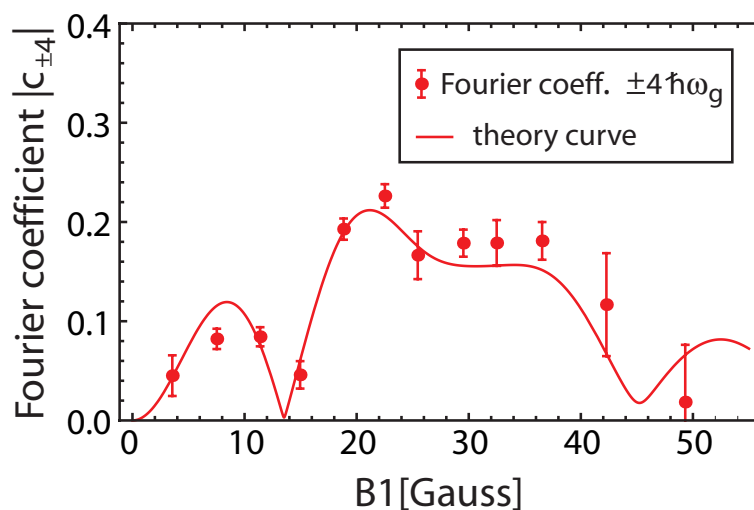


Figure 2.38: Fourier coefficient $c_{\pm 4}$ obtained by discrete Fourier transformation of the measured time-resolved interference patterns for the two mode magnetic field ($\omega_g = 1\text{kHz}$). The measured points are compared to the theoretical curve is deduced from (eq.2.101).

2. ENERGY EXCHANGE IN A TIME-DEPENDENT MAGNETIC FIELD

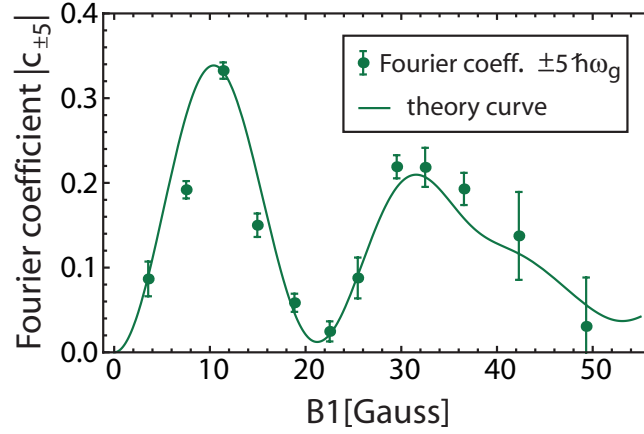


Figure 2.39: Fourier coefficient $c_{\pm 5}$ obtained by discrete Fourier transformation of the measured time-resolved interference patterns for the two mode magnetic field ($\omega_g = 1\text{kHz}$). The measured points are compared to the theoretical curve is deduced from (eq.2.101).

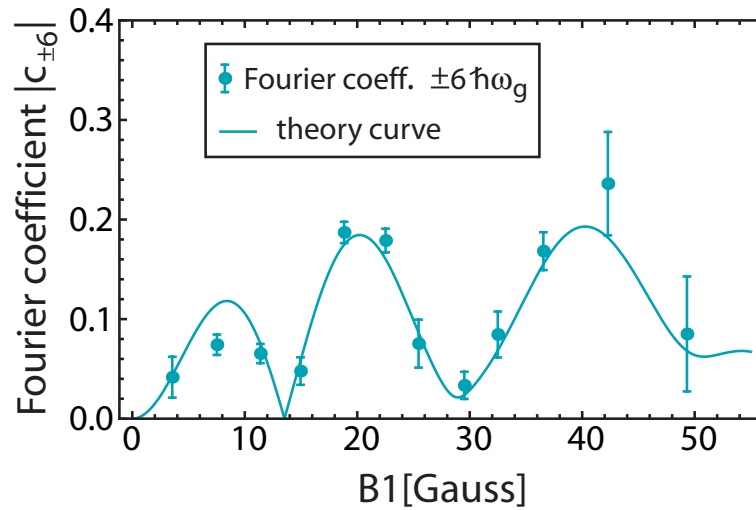


Figure 2.40: Fourier coefficient $c_{\pm 6}$ obtained by discrete Fourier transformation of the measured time-resolved interference patterns for the two mode magnetic field ($\omega_g = 1\text{kHz}$). The measured points are compared to the theoretical curve is deduced from (eq.2.101).

2.3.3 Magnetic field with three modes

The magnetic field now contains three frequencies

$$B(t) = B_1 \cos(\omega_1 t + \varphi_1) + B_2 \cos(\omega_2 t + \varphi_2) + B_3 \cos(\omega_3 t + \varphi_3) \quad (2.109)$$

where $\omega_1 = 2\pi \cdot 3\text{kHz}$, $\omega_2 = 2\pi \cdot 5\text{kHz}$, $\omega_3 = 2\pi \cdot 7\text{kHz}$, $\varphi_1 = 0$, $\varphi_2 = 0.62$ and $\varphi_3 = 2.46$. The period of this signal is given by the greatest common denominator $\omega_g = 2\pi \cdot 1\text{kHz}$ of the three frequencies ω_1 , ω_2 and ω_3 . We divide the signal period into 128 channels and record the time-resolved interference pattern for various field amplitudes, where $B_2 = 0.94B_1$ and $B_3 = 0.89B_1$ is always maintained (e.g. fig.2.41).

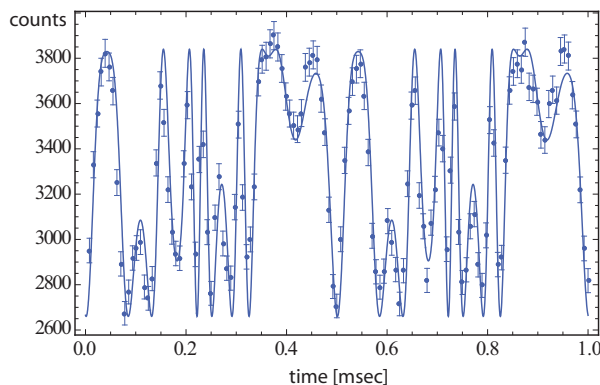


Figure 2.41: The time-resolved interference pattern for $B(t) = B_1 \cos(\omega_1 t) + B_2 \cos(\omega_2 t + 0.62) + B_3 \cos(\omega_3 t + 2.46)$ with $\omega_1 = 2\pi \cdot 3\text{kHz}$, $\omega_2 = 2\pi \cdot 5\text{kHz}$, $\omega_3 = 2\pi \cdot 7\text{kHz}$, $B_2 = 0.94B_1$, $B_3 = 0.89B_1$ and $B_1 = 16$ Gauss. Full period ($=2\pi/\omega_g=1\text{ms}$) divided into 128 channels.

Again, the Fourier components of the time-dependent intensity contain the transition amplitudes for the various energy transfers. We have used unpolarized neutron and as a consequence, not all combinations of the three basic frequencies belonging to a certain energy transfer contribute. For example, odd multiples of the greatest common denominator $\omega_g = 2\pi \cdot 1\text{ kHz}$ vanish completely. The less experimental effort by using unpolarized neutrons has therefore be compensated with a higher effort in the analysis. As an example we depict the characteristics of some Fourier components versus field amplitude (fig.2.42). The Fourier components are closely related to the transition amplitudes (see eq.2.101).

2. ENERGY EXCHANGE IN A TIME-DEPENDENT MAGNETIC FIELD

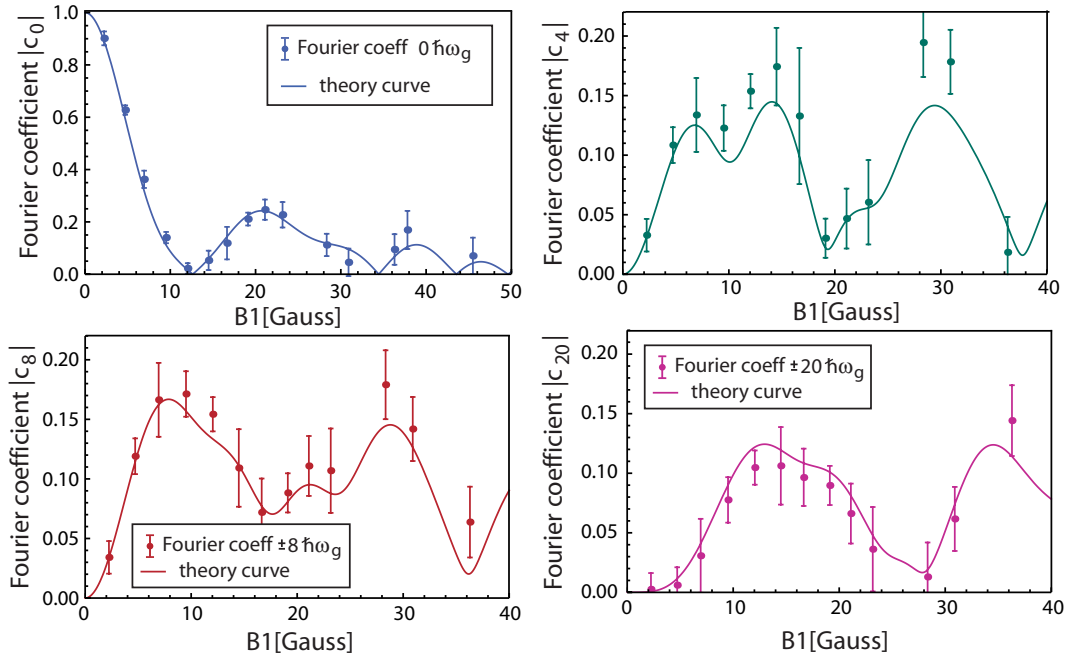


Figure 2.42: Fourier components obtained by discrete Fourier transformation of the measured time-resolved interference patterns for the three mode field ($\omega_g = 1\text{kHz}$).

2.3.4 Magnetic field with five modes

The highest number of modes we have experimentally investigated was five, i.e. the magnetic field was

$$B(t) = \sum_{i=1}^5 B_i \cos(\omega_i t + \varphi_i) \quad (2.110)$$

where $\omega_1 = 2\pi \cdot 3\text{kHz}$, $\omega_2 = 2\pi \cdot 5\text{kHz}$, $\omega_3 = 2\pi \cdot 7\text{kHz}$, $\omega_4 = 2\pi \cdot 11\text{kHz}$, $\omega_5 = 2\pi \cdot 13\text{kHz}$ and all $\varphi_i = 0$. The relation between the B_i 's is given by $B_2 = 0.95B_1$, $B_3 = 0.83B_1$, $B_4 = 0.72B_1$, and $B_5 = 0.62B_1$. The period of this signal is again given by the greatest common denominator $\omega_g = 2\pi \cdot 1\text{kHz}$. The resolution of the time-dependent intensity pattern is still possible, though the fitting procedure becomes more challenging and the agreement between fit and theory curves gets worse compared to the examples with lower modes (see figs. 2.43, 2.44). But in principle, the procedure can be applied to an arbitrary high, countable number of modes as long as the ratio of occurring frequencies is a rational number.

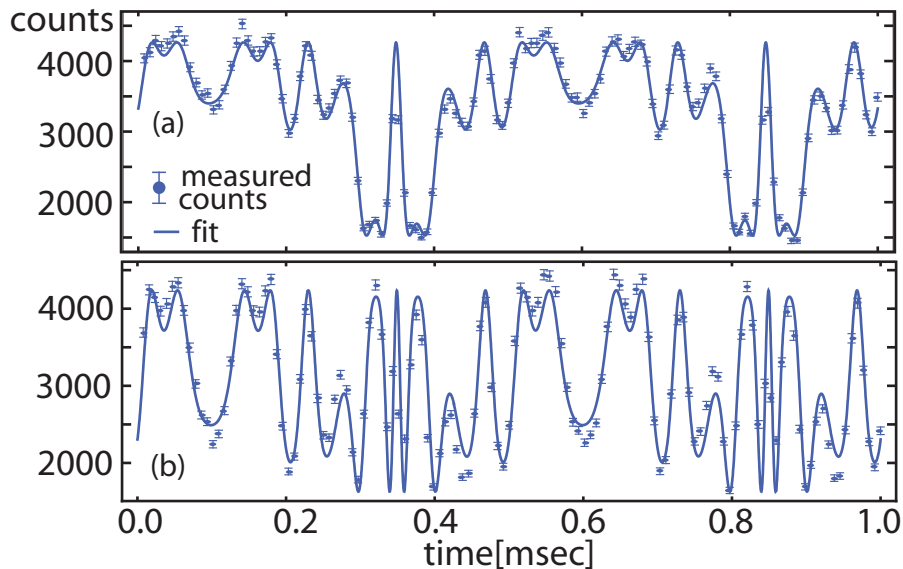


Figure 2.43: Example of a time-resolved interference pattern for $B(t) = \sum_{i=1}^5 B_i \cos(2\pi f_i t + \varphi_i)$ with $f_1 = 3\text{kHz}$, $f_2 = 5\text{kHz}$, $f_3 = 7\text{kHz}$, $f_4 = 11\text{kHz}$, $f_5 = 13\text{kHz}$, $\phi_1 = \phi_2 = \phi_3 = \phi_4 = 0$, $\phi_5 = 0.1$, $B_2 = 0.95B_1$, $B_3 = 0.83B_1$, $B_4 = 0.72B_1$, $B_5 = 0.62B_1$ and $B_1 = 4$ Gauss (a) and 11 Gauss (b).

In chapter 3, we will extend our investigations of time-dependent magnetic fields in neutron interferometry to the case of noise fields that do not fulfill the

2. ENERGY EXCHANGE IN A TIME-DEPENDENT MAGNETIC FIELD

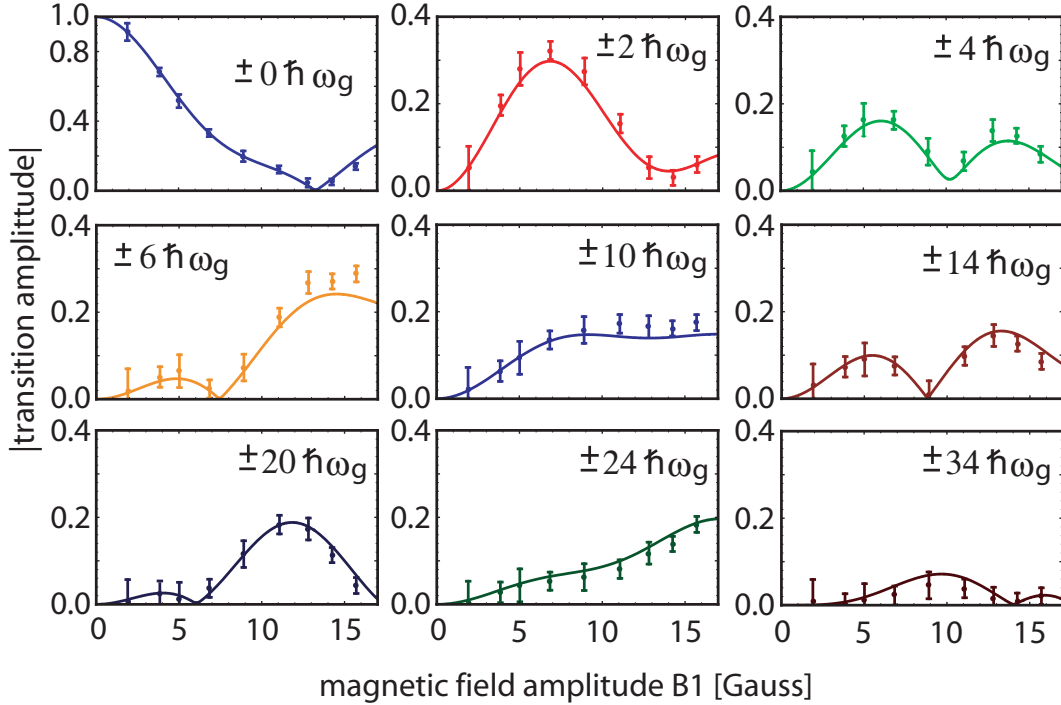


Figure 2.44: Transition amplitudes of various energy exchanges for the five mode magnetic field as described in fig.2.43. For an odd frequency number, the odd multiples of greatest common denominator of the occurring frequencies $\hbar\omega_g = 2\pi \cdot 1\text{kHz}$ vanish for unpolarized neutrons.

condition of periodicity. They consist of an infinite number of modes and their frequency spectrum lies dense in the set of real numbers. Resolution of energy transfer is then not possible with the methods presented here, but we are more interested in the behaviour of the interferometer contrast when noise fields are applied, because of the connection between noise fields and decoherence, i.e. vanishing contrast. In contrast to ideal noises, real signals consist of a countable number of modes and we will also use the formulae derived in this chapter to calculate the interferometer contrast. We will see that above a certain number of modes (~ 200) the difference to the ideal case with an infinite number of modes is experimentally not seizable (see chap.4).

2.4 Quantized field treatment

In the preceding chapters, we have dealt with the interaction of a neutron that passes an oscillating magnetic field that is bounded to a finite region $0 \leq x < L$. Though we have treated the field purely classical, one could already see that the energy transfer between neutron and field is quantized, i.e. only integer multiples of the frequencies contained in the magnetic field signal are exchanged. In the most simple case of a single mode field with frequency ω , the probability of exchanging an energy amount of $n\hbar\omega$ is given by the square of the n -th Bessel function $|J_n|^2$. In several papers [Sum1993, SHK⁺1995], this process is claimed to be an n -photon exchange. To justify this statement, one at first has to answer the question: what is a photon?

If we define the photon as a unit of electromagnetic radiation with energy $\hbar\omega$, the statement is just. After passing the field region, the energy of the neutron has changed for an amount $n\hbar\omega$ with probability $|J_n|^2$. Thus, at least on an effective level, n photons with frequency ω have been exchanged.

On the other hand, the most accurate theory for describing the electromagnetic field is the quantum field theory. In its framework, every mode of the electromagnetic field is described by a quantum harmonic oscillator. The occupation numbers of the oscillators are interpreted as photons. Creation and annihilation operators acting on the field state change the photon number. Treating the magnetic field as a quantum field would thus allow us to keep track of the actual photon number in every stage of the physical process.

An electromagnetic field can be subjected to quantization if it is a solution of the (inhomogeneous) Maxwell-equations. Since we are interested in a very special, rectangular form for the spatial structure of the field, the solutions obtained from the quantization of the free electromagnetic field will not be suitable to construct such a mode form. Quantization of the electromagnetic field in presence of external sources is by far no trivial task, but if we restrict ourselves to classical currents as sources we can use the following result [Kro1965, CTDRG1997]:

The quantum mechanical state generated by a time-dependent classical current is just the coherent state corresponding to the field that would have been produced classically.

Now consider a superconducting resonant circuit whose resonant frequency is so low that radiation losses can be neglected during the measurement time. The spatial characteristics of the magnetic field along the coil axis can now, as in the classical case, be approximated by the simple rectangular form (constant within coil region $0 \leq x < L$, zero outside). In addition, the only mode that is excited is the one belonging to the resonance frequency ω_{res} . That means we can write

2. ENERGY EXCHANGE IN A TIME-DEPENDENT MAGNETIC FIELD

the field operator in the form

$$\hat{B} \propto (\hat{a}f(x) + \hat{a}^\dagger f^*(x)) \quad (2.111)$$

where $f(x)$ describes the spatial structure of the mode and \hat{a} (\hat{a}^\dagger) denotes the creation (annihilation) operator associated with ω_{res} . The proportionality factor will be derived later (see eq.2.143).

Due to the special spatial structure of the field, we have to distinguish between three different situations accompanied by three different Hamiltonians. If the neutron is inside the field region, i.e. its position variable x_{neutron} lies between 0 and L , an interaction takes place and thus, an interaction term occurs in the Hamiltonian. This interaction term can be found for example in [PCT1965] and stems from the quantized version of the Zeemann Hamiltonian that describes the interaction between the neutron and a magnetic field. All constants are absorbed in the coupling parameter λ . If the neutron is outside the field region, the neutron and the field both evolve undisturbed and the Hamiltonian only consists of the two free Hamilton operators for field and particle. Explicitly, the three Hamiltonians read in the Schrödinger picture representation (vacuum energy of the field mode is omitted for clarity's sake)

$$\hat{H}_I = \frac{p^2}{2m} + \hbar\omega a^\dagger a, \quad x_{\text{neutron}} < 0 \quad (2.112)$$

$$\hat{H}_{II} = \frac{p^2}{2m} + \hbar\omega a^\dagger a + \lambda\sigma_z (a^\dagger + a), \quad 0 \leq x_{\text{neutron}} < L \quad (2.113)$$

$$\hat{H}_{III} = \frac{p^2}{2m} + \hbar\omega a^\dagger a, \quad L \leq x_{\text{neutron}} \quad (2.114)$$

In the further, we will omit the subscript in the position variable, x always refers to the position coordinate of the neutron if not stated otherwise. We solve the Schrödinger equation for a up polarized ($\sigma_z = +1$) neutron. In region I, where no interaction between the magnetic field and the neutron takes place the general solution is given by an arbitrary superposition of plane waves for the neutron and Fock states of the field

$$|\Psi_I\rangle = \sum_n \int dk c_n^I(k) |k\rangle \otimes |n\rangle \quad (2.115)$$

As "initial" condition for the calculation we choose the neutron to be a plane wave of fixed wave vector k_0 and the magnetic field is present in a distinct Fock state n_0 . This yields for the overall wave function whose time dependence is now also included explicitly

$$|\Psi_I(t)\rangle = e^{-i\omega_0 t} |k_0\rangle \otimes e^{-i\omega n_0 t} |n_0\rangle \quad (2.116)$$

To find the general solution for region II we convert the Hamiltonian (eq.2.113)

$$\begin{aligned}
\hat{H}_{II} &= \frac{p^2}{2m} + \hbar\omega a^\dagger a + \lambda (a^\dagger + a) \\
&= \frac{p^2}{2m} + \hbar\omega \left(a^\dagger + \frac{\lambda}{\hbar\omega} \right) \left(a + \frac{\lambda}{\hbar\omega} \right) - \frac{\lambda^2}{\hbar\omega} \\
&= \frac{p^2}{2m} + \hbar\omega D^\dagger \left(\frac{\lambda}{\hbar\omega} \right) a^\dagger a D \left(\frac{\lambda}{\hbar\omega} \right) - \frac{\lambda^2}{\hbar\omega}
\end{aligned} \tag{2.117}$$

with the help of the unitary displacement operator $D(\alpha)$ that is defined by

$$D(\alpha) = e^{\alpha a^\dagger - \alpha^* a} \tag{2.118}$$

and fulfills

$$D^\dagger(\alpha) a^{(\dagger)} D(\alpha) = a^{(\dagger)} + \alpha \tag{2.119}$$

Thus, the eigenfunctions of (2.117) are given by

$$|k\rangle \otimes D^\dagger \left(\frac{\lambda}{\hbar\omega} \right) |n\rangle \tag{2.120}$$

belonging to the energy eigenvalue

$$\hat{H}_{II} \left(|k\rangle \otimes D^\dagger \left(\frac{\lambda}{\hbar\omega} \right) |n\rangle \right) = E^{II}(k, n) \left(|k\rangle \otimes D^\dagger \left(\frac{\lambda}{\hbar\omega} \right) |n\rangle \right) \tag{2.121}$$

$$E^{II}(k, n) = \frac{\hbar^2 k^2}{2m} + \hbar\omega n - \frac{\lambda^2}{\hbar\omega} = \hbar\omega(k) + \hbar\omega n - \hbar\tilde{\lambda} \tag{2.122}$$

where we have defined

$$\omega(k) \equiv \frac{\hbar^2 k^2}{2m}, \quad \tilde{\lambda} \equiv \frac{\lambda^2}{\hbar^2 \omega} \tag{2.123}$$

for better readability. An arbitrary superposition of these eigenstates constitutes the general solution in region II

$$|\Psi_{II}(t)\rangle = \sum_{n=0}^{\infty} \int_{-\infty}^{+\infty} dk c_n^{II}(k) e^{-iE^{II}(k,n)t/\hbar} |k\rangle \otimes D^\dagger \left(\frac{\lambda}{\hbar\omega} \right) |n\rangle \tag{2.124}$$

In the following the argument $\lambda/\hbar\omega$ of the displacement operator will be omitted. Before we proceed with the calculation by matching the wave functions $|\Psi_I\rangle$ and $|\Psi_{II}\rangle$ at $x = 0$, a few remarks concerning the meaning of the position coordinate x and the different regions:

In contrast to section 2.1, $|\Psi_I\rangle$ does not mean overall wave function (neutron and field) $|\Psi_I(x)\rangle$ for $x \leq 0$. The spatial characteristics of the field are given

2. ENERGY EXCHANGE IN A TIME-DEPENDENT MAGNETIC FIELD

by fig.2.1 with $B_0 = 0$. The field is always only present in region II, i.e. where $0 \leq x \leq L$ and it changes its state depending on the position of the neutron. Thus, $|\Psi_I\rangle$ describes the overall wave function when the position coordinate of the neutrons wavefunction has value below 0. In a simple picture, one can say when the neutron is left from the field region. In this case, no interaction takes place and both subsystems, field and neutron evolve freely in time. When the neutron is present in the field region, the field gets displaced due to the interaction with the neutron and the dynamics of the composite system change described by H_{II} . To fulfill the matching condition we express the neutron part of the wave function in its position representation and equalize $|\Psi_I\rangle$ and $|\Psi_{II}\rangle$ at $x = 0$.

$$\Psi_I(x, t) = e^{ik_0x} e^{-i\omega_0t} e^{-i\omega n_0t} |n_0\rangle \longrightarrow \Psi_I(0, t) = e^{-i\omega_0t} e^{-i\omega n_0t} |n_0\rangle \quad (2.125)$$

$$\Psi_{II}(0, t) = \sum_n \int dk c_n^{II}(k) e^{-i\omega(k)t} e^{-i\omega n t} e^{i\tilde{\lambda}t} D^\dagger |n\rangle \quad (2.126)$$

From

$$\Psi_I(0, t) = \Psi_{II}(0, t) \quad (2.127)$$

we get the coefficient $c_n^{II}(k)$ by multiplying both sides with $\langle n_0 + q | D \rangle$, exploiting unitary of the displacement operator, using the orthogonality of the Fock states and equating coefficients of $e^{-i\omega t}$.

$$\begin{aligned} e^{-i(\omega_0+\omega n_0)t} |n_0\rangle &= \sum_n \int dk c_n^{II}(k) e^{-i\omega(k)t} e^{-i\omega n t} e^{i\tilde{\lambda}t} D^\dagger |n\rangle \\ e^{-i(\omega_0+\omega n_0)t} \langle n_0 + q | D | n_0\rangle &= \sum_n \int dk c_n^{II}(k) e^{-i\omega(k)t} e^{-i\omega n t} e^{i\tilde{\lambda}t} \delta_{n_0+q,n} \\ e^{-i(\omega_0+\omega n_0)t} \langle n_0 + q | D | n_0\rangle &= \int dk c_{n_0+q}^{II}(k) e^{-i\omega(k)t} e^{-i\omega(n_0+q)t} e^{i\tilde{\lambda}t} \\ e^{-i(\omega_0-\omega q+\tilde{\lambda})t} \langle n_0 + q | D | n_0\rangle &= \int dk c_{n_0+q}^{II}(k) e^{-i\omega(k)t} \end{aligned}$$

This equality can be fulfilled if

$$c_{n_0+q}^{II}(k) = c_{n_0+q}^{II} \cdot \delta_{k, \tilde{k}_{-q}} = \langle n_0 + q | D | n_0\rangle \cdot \delta_{k, \tilde{k}_{-q}} \quad (2.128)$$

where

$$\tilde{k}_{-q} \equiv \left(k_0^2 + \frac{2m}{\hbar} \tilde{\lambda} - \frac{2m}{\hbar} \omega q \right)^{1/2} \quad (2.129)$$

because

$$\omega(\tilde{k}_{-q}) = \frac{\hbar \tilde{k}_{-q}^2}{2m} = \frac{\hbar}{2m} \left(k_0^2 + \frac{2m}{\hbar} \tilde{\lambda} - \frac{2m}{\hbar} \omega q \right) = \omega_0 - \omega q + \tilde{\lambda} \quad (2.130)$$

2.4 Quantized field treatment

Inserting the coefficient $c_n^{II}(k)$ given by (eq.2.128) into the general form of Ψ_{II} (eq.2.124) we obtain

$$\begin{aligned}
 |\Psi_{II}(t)\rangle &= \sum_{q=-n_0}^{\infty} \langle n_0 + q | D | n_0 \rangle e^{-iE^{II}(\tilde{k}_{-q}, n_0+q)t/\hbar} |\tilde{k}_{-q}\rangle \otimes D^\dagger |n_0 + q\rangle \\
 |\Psi_{II}(t)\rangle &= \sum_{q=-n_0}^{\infty} \langle n_0 + q | D | n_0 \rangle e^{-i(\omega(\tilde{k}_{-q})+(n_0+q)\omega-\tilde{\lambda})t} |\tilde{k}_{-q}\rangle \otimes D^\dagger |n_0 + q\rangle \\
 |\Psi_{II}(t)\rangle &= e^{-i(\omega_0+n_0\omega)t} \sum_{q=-n_0}^{\infty} \langle n_0 + q | D | n_0 \rangle |\tilde{k}_{-q}\rangle \otimes D^\dagger |n_0 + q\rangle \quad (2.131)
 \end{aligned}$$

We can see from the overall time-dependent phase factor, that the energy of the total system is conserved. i.e equal to the energy of the "initial" state $|\Psi_I\rangle$. Changes in the photon number of the (displaced) field are compensated by the neutron's momentum. The superposition of all possible exchanges yields the solution for region II. The probability of exchanging a certain number of photons q is given by the matrix element $\langle n_0 + q | D | n_0 \rangle$. To meet the matching condition, the constant shift $\hbar\tilde{\lambda}$ in the energy was absorbed in the neutron's momentum. Written in position space, (eq.2.131) reads

$$\Psi_{II}(x, t) = e^{-i(\omega_0+n_0\omega)t} \sum_{q=-n_0}^{\infty} \langle n_0 + q | D | n_0 \rangle e^{i\tilde{k}_{-q}x} D^\dagger |n_0 + q\rangle \quad (2.132)$$

In region III, neutron and field do not interact anymore and the general solution reads

$$|\Psi_{III}(t)\rangle = \sum_n \int dk c_n^{III}(k) e^{-i\omega(k)t} |k\rangle \otimes e^{-in\omega t} |n\rangle, \quad \omega(k) = \frac{\hbar k^2}{2m} \quad (2.133)$$

Again, we write the neutron part of the wave function in position representation and equalize $|\Psi_{II}\rangle$ and $|\Psi_{III}\rangle$ at $x = L$.

$$\begin{aligned}
 \sum_n \int dk c_n^{III}(k) e^{-i\omega(k)t} e^{ikL} e^{-in\omega t} |n\rangle = \\
 e^{-i(\omega_0+n_0\omega)t} \sum_{q=-n_0}^{\infty} \langle n_0 + q | D | n_0 \rangle e^{i\tilde{k}_{-q}L} D^\dagger |n_0 + q\rangle
 \end{aligned}$$

2. ENERGY EXCHANGE IN A TIME-DEPENDENT MAGNETIC FIELD

We multiply both sides with $\langle n_0 + q_2 |$ and use $\langle n | m \rangle = \delta_{n,m}$.

$$\begin{aligned} \int dk c_{n_0+q_2}^{III}(k) e^{-i\omega(k)t} e^{ikL} e^{-(n_0+q_2)\omega t} = \\ e^{-i(\omega_0+n_0\omega)t} \sum_{q=-n_0}^{\infty} \langle n_0 + q | D | n_0 \rangle e^{i\tilde{k}-qL} \langle n_0 + q_2 | D^\dagger | n_0 + q \rangle \\ \int dk c_{n_0+q_2}^{III}(k) e^{-i\omega(k)t} e^{ikL} = \\ e^{-i(\omega_0-q_2\omega)t} \sum_{q=-n_0}^{\infty} \langle n_0 + q | D | n_0 \rangle e^{i\tilde{k}-qL} \langle n_0 + q_2 | D^\dagger | n_0 + q \rangle \end{aligned}$$

Equating coefficients of $e^{-i\omega t}$, one can see that this equation can be fulfilled if

$$c_{n_0+q_2}^{III}(k) = c_{n_0+q_2}^{III} \cdot \delta_{k,k-q_2}, \quad k_{-q_2}^2 = k_0^2 + \frac{2m}{\hbar} q_2 \omega \quad (2.134)$$

which gives

$$\begin{aligned} \int dk c_{n_0+q_2}^{III} \delta_{k,k-q_2} e^{-i\omega(k)t} e^{ikL} = \\ e^{-i(\omega_0-q_2\omega)t} \sum_{q=-n_0}^{\infty} \langle n_0 + q | D | n_0 \rangle e^{i\tilde{k}-qL} \langle n_0 + q_2 | D^\dagger | n_0 + q \rangle \\ c_{n_0+q_2}^{III} e^{-i\omega(k-q_2)t} e^{ik-q_2L} = \\ e^{-i(\omega_0-q_2\omega)t} \sum_{q=-n_0}^{\infty} \langle n_0 + q | D | n_0 \rangle e^{i\tilde{k}-qL} \langle n_0 + q_2 | D^\dagger | n_0 + q \rangle \\ \implies c_{n_0+q_2}^{III} = \sum_{q=-n_0}^{\infty} \langle n_0 + q | D | n_0 \rangle e^{i(\tilde{k}-q-k-q_2)L} \langle n_0 + q_2 | D^\dagger | n_0 + q \rangle \quad (2.135) \end{aligned}$$

By taking into account that the incident kinetic energy of the neutron is much larger than the transferred photon energies or the $\lambda^2/\hbar\omega$ -shift we use

$$(k_0^2 + \Delta)^{\frac{1}{2}} \simeq k_0 + \frac{1}{2} \frac{\Delta}{k_0}, \quad k_0^2 \gg \Delta$$

to rewrite the exponent

$$(\tilde{k}_{-q} - k_{-q_2})L \simeq (k_0 + \frac{m}{\hbar k_0} \tilde{\lambda} - \frac{m}{\hbar k_0} \omega q - k_0 + \frac{m}{\hbar k_0} q_2)L = \tilde{\lambda}T - (q - q_2)\omega T$$

with the time of flight T through the field region

$$\frac{m}{\hbar k_0} L = \frac{L}{v_0} = T \quad (2.136)$$

The final result for the total wave function after the neutron has passed the field thus reads

$$|\Psi_{III}(t)\rangle = e^{-i(\omega_0+n_0\omega)t} \sum_{q_2=-n_0}^{+\infty} c_{n_0+q_2}^{III} |k_{-q_2}\rangle \otimes |n_0 + q_2\rangle \quad (2.137)$$

where

$$c_{n_0+q_2}^{III} = e^{i\tilde{\lambda}T} \sum_{q=-n_0}^{\infty} \langle n_0 + q_2 | D^\dagger | n_0 + q \rangle \langle n_0 + q | D | n_0 \rangle e^{-i(q-q_2)\omega T} \quad (2.138)$$

Equations 2.137 and 2.138 allow a very intuitive physical explanation. Like in region II, the total energy is conserved and every change of the initial photon number n_0 in the field is compensated by a change of the neutrons momentum. The superposition of all possible exchanges gives the total wave function in region III. The coefficient $c_{n_0+q_2}^{III}$ that belongs to the transition from initial photon number n_0 to final photon number $n_0 + q_2$ also reflects the underlying physical processes. At the neutron's entrance in the field with photon number n_0 , displacement of the field occurs and transitions to other photon numbers become possible. After the neutron has left the field region, the field gets displaced back and transitions from $n_0 + q$ to $n_0 + q_2$ can happen. All possible intermediate steps, i.e. all q 's, have to be summed up and are weighted with a phase factor that reflects the energy difference $\hbar(q - q_2)\omega$ between the intermediate and the final photon number state. Due to the constant energy shift $\hbar\tilde{\lambda}$ in \hat{H}_{II} , the total wave function Ψ_{III} has also consumed a phase $\tilde{\lambda}T$ related to this shift and the length of stay T in the field region. So, we are able to explain every term that occurs in eqs.2.137 and 2.138. The simple pictures of an onefold absorbtion/emission of q_2 photons does not hold. In fact, the photon number changes two times, namely at the field gradients, and a certain final state is obtained by a summation over the possible intermediate states. For a graphical illustration see fig.2.45.

The fully quantized treatment of neutron and field is the most exact one and we can relate it to the results of the classical calculations in section 2.1 by investigating the final result (eq.2.137) for special states of the magnetic field, namely the coherent state [Gla1963]. It approximates the classical behaviour in the best fashion [HR2006]. To compare the results, we have to show first, how the different coupling constants (μ, λ) are connected to each other. Therefore, we look at the expectation value of the interaction term of the Hamiltonian in the coherent state in the Heisenberg picture and compare it with the classical

2. ENERGY EXCHANGE IN A TIME-DEPENDENT MAGNETIC FIELD

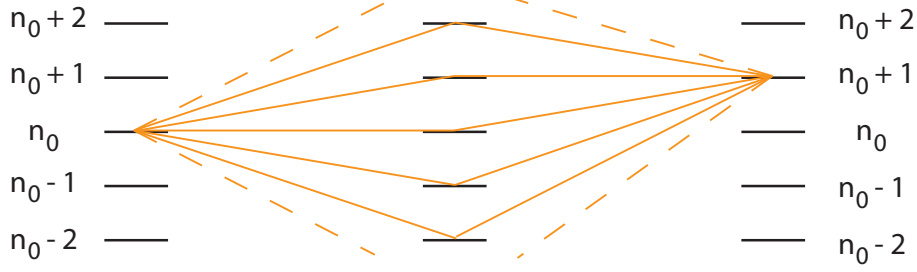


Figure 2.45: The transition from initial state (n_0) to the final state (n_0+1) happens over an intermediate state. All possible intermediate states have to be summed up to get the transition amplitude $\sum_q \langle n_0+1 | D^\dagger | n_0+q \rangle \langle n_0+q | D | n_0 \rangle e^{-iq\omega T}$.

potential $\mu\sigma B$.

$$\begin{aligned}
 \langle \alpha | \hat{H}_{int} | \alpha \rangle &= \lambda \sigma_z \langle \alpha | (a^\dagger e^{i\omega t} + a e^{-i\omega t}) | \alpha \rangle = \lambda \sigma_z (\alpha^* e^{i\omega t} + \alpha e^{-i\omega t}) \\
 &= \lambda \sigma_z |\alpha| (e^{-i\varphi_\alpha} e^{i\omega t} + e^{i\varphi_\alpha} e^{-i\omega t}) = 2\lambda \sigma_z |\alpha| \cos(\omega t - \varphi_\alpha) \\
 &\triangleq \mu \sigma_z B_1 \cos(\omega t + \varphi_1) \\
 \implies \lambda &= \frac{\mu B_1}{2|\alpha|} \tag{2.139}
 \end{aligned}$$

With the help of the energy density of the electromagnetic field

$$w(x, t) = \frac{1}{2} \left(\varepsilon_0 E^2(x, t) + \frac{1}{\mu_0} B^2(x, t) \right) \tag{2.140}$$

we get the classical expression for the (time-averaged) energy of the magnetic field

$$H_{class} = \frac{1}{T} \int_0^T dt \int_V dx w(x, t) = \frac{V}{2\mu_0} B_1^2 \frac{1}{T} \int_0^T \cos^2(\omega t) dt = \frac{V}{4\mu_0} B_1^2 \tag{2.141}$$

and compare it with the quantum mechanical expression

$$\langle \alpha | \hat{H}_0 | \alpha \rangle = \hbar\omega \langle \alpha | a^\dagger a | \alpha \rangle = \hbar\omega |\alpha|^2 \equiv \hbar\omega \bar{N} \tag{2.142}$$

from which we get

$$\frac{B_1}{|\alpha|} = 2\sqrt{\frac{\mu_0 \hbar \omega}{V}} \implies \lambda = \mu \sqrt{\frac{\mu_0 \hbar \omega}{V}} \tag{2.143}$$

For an estimated coil volume of several cm^3 the coupling constant λ divided by the photon energy reads $\lambda/\hbar\omega \simeq 10^{-11}$ illustrating the weak coupling between the neutron and the field. Therefore one expects visible effects not until very high

2.4 Quantized field treatment

photon numbers, i.e sufficient field strengths. In case of a 1kHz field and and amplitude of 1Gauss the mean photon number is already $\bar{N} = |\alpha|^2 = VB_1^2/4\mu_0\hbar\omega \simeq 10^{21}$. In the coherent state $|\alpha\rangle$, the photon number is Poissonian distributed with mean value $\bar{N} = |\alpha|^2$ and variance $\sqrt{\bar{N}} = |\alpha|$ and therefore the main contributions come from Fock states with a very high photon number. The matrix elements in (eq.2.138) can be calculated for such high photon numbers [PCT1965].

$$\langle m| D\left(\frac{\lambda}{\hbar\omega}\right)|n\rangle = J_{m-n}\left(\frac{2\lambda\sqrt{n}}{\hbar\omega}\right) = J_{m-n}\left(\frac{\mu B_1}{\hbar\omega}\right) \quad (2.144)$$

$$\langle m| D^\dagger\left(\frac{\lambda}{\hbar\omega}\right)|n\rangle = J_{n-m}\left(\frac{2\lambda\sqrt{n}}{\hbar\omega}\right) = J_{n-m}\left(\frac{\mu B_1}{\hbar\omega}\right) \quad (2.145)$$

where we have used $n \simeq \bar{N}$ and (eq.2.139). These are the Bessel functions that occur already in the classical treatment, but now they got a physical explanation. With the help of Graf's addition theorem (eq.2.26) we can also perform the summation over q when using

$$\begin{aligned} \sum_q &= \sum_{q=-n_0}^{\infty} \simeq \sum_{q=-\infty}^{\infty} \\ \sum_q \langle n_0 + q_2| D^\dagger\left(\frac{\lambda}{\hbar\omega}\right)|n_0 + q\rangle \langle n_0 + q| D\left(\frac{\lambda}{\hbar\omega}\right)|n_0\rangle e^{-iq\omega T} &= \\ \sum_q J_q\left(\frac{\mu B_1}{\hbar\omega}\right) J_{q-q_2}\left(\frac{\mu B_1}{\hbar\omega}\right) e^{-iq\omega T} &= J_{q_2}\left(\frac{\mu B_1}{\hbar\omega}\right) \sin\frac{\omega T}{2} e^{iq_2(\omega T - \pi)/2} \end{aligned} \quad (2.146)$$

This summation also occurred in the classical calculation at the matching at $x = L$. But there, it only seems to be a mathematical procedure. By introducing the field quantization, the physical origin of the expression becomes visible. The coefficient $c_{n_0+q_2}^{III}$ in case of high photon number n_0 finally reads

$$c_{n_0+q_2}^{III} = e^{i\tilde{\lambda}T} J_{q_2}\left(\frac{\mu B_1}{\hbar\omega}\right) \sin\frac{\omega T}{2} e^{iq_2(\omega T - \pi)/2} \quad (2.147)$$

Apart from the neglectable $\tilde{\lambda}$ -shift ($\tilde{\lambda}T \simeq 10^{-23}$), it corresponds exactly to the classically derived coefficient given by (eq.2.27) when $l = -q_2$ is inserted. The negative sign arises from the fact that $c_{n_0+q_2}^{III}$ means that the field energy, i.e. its photon number, was increased by $q_2\hbar\omega$ whereas the kinetic energy of the neutron has been reduced by $q_2\hbar\omega$. Solely the phase factor $e^{-i\varphi_1}$ coming from the phase of the magnetic field at $t = 0$ cannot be reproduced. Fock states do not carry any phase information [Lou2000], the complete reproduction of the results of

2. ENERGY EXCHANGE IN A TIME-DEPENDENT MAGNETIC FIELD

the classical calculation can only be achieved by assuming the field to be in the coherent state $|\alpha\rangle$ of the mode ω with

$$\alpha = |\alpha|e^{i\varphi_\alpha}, \quad |\alpha| = \frac{B_1}{2}\sqrt{V/\mu_0\hbar\omega}, \quad \varphi_\alpha = -\varphi_1 \quad (2.148)$$

so that

$$\langle\alpha|\hat{H}_{int}|\alpha\rangle = \mu\sigma_z B_1 \cos(\omega t + \varphi_1) \quad (2.149)$$

is fulfilled. The expansion of the coherent state in terms of Fock states is given by

$$|\alpha\rangle = \sum_{n=0}^{\infty} c_n^{(\alpha)} |n\rangle = e^{-|\alpha|^2/2} \sum_{n=0}^{\infty} \frac{\alpha^n}{\sqrt{n!}} |n\rangle \quad (2.150)$$

and represents, as already mentioned, a Poissonian distribution for the photon number probability $|c_n^{(\alpha)}|^2$ with mean value $|\alpha|^2$ and standard deviation $|\alpha|$. If the field is initially in a coherent state $|\alpha\rangle$, the wave function $|\Psi_I\rangle$ reads

$$|\Psi_I\rangle = |k_0\rangle \otimes |\alpha\rangle = |k_0\rangle \otimes \sum_{n_0=0}^{\infty} c_{n_0}^{(\alpha)} |n_0\rangle = \sum_{n_0} c_{n_0}^{(\alpha)} |k_0\rangle \otimes |n_0\rangle \quad (2.151)$$

where we have used the calculation rules for tensor products. By exploiting the linearity of the Hamilton operator we can immediately use the result (eq.2.59) for a distinct Fock state $|n_0\rangle$ and superpone all n_0 's weighted with the coefficients c_{n_0} .

$$|\Psi_{III}(t)\rangle = \sum_{n_0} c_{n_0}^{(\alpha)} e^{-i(\omega_0+n_0\omega)t} \sum_{q_2=-n_0}^{+\infty} c_{n_0+q_2}^{III} |k_{-q_2}\rangle \otimes |n_0 + q_2\rangle \quad (2.152)$$

To perform this summation it is advantageous to change the summation index in the expression for the final state

$$|\Psi_{III}(t)\rangle = \sum_{n_0} c_{n_0}^{(\alpha)} e^{-i(\omega_0+n_0\omega)t} \sum_{m=0}^{+\infty} c_m^{III} |k_{n_0-m}\rangle \otimes |m\rangle \quad (2.153)$$

and in the coefficient c_m^{III}

$$c_m^{III} = e^{i\tilde{\lambda}T} \sum_{n=0}^{\infty} \langle m|D^\dagger|n\rangle \langle n|D|n_0\rangle e^{-i(n-m)\omega T} \quad (2.154)$$

yielding

$$\begin{aligned} |\Psi_{III}\rangle &= \sum_{n_0, m, n} c_{n_0}^{(\alpha)} e^{i\tilde{\lambda}T} \langle m|D^\dagger|n\rangle \langle n|D|n_0\rangle e^{-i(n-m)\omega T} \\ &\quad \times e^{-i(\omega_0+n_0\omega)t} |k_{n_0-m}\rangle \otimes |m\rangle \end{aligned} \quad (2.155)$$

We again rewrite the neutron part of the wave function in coordinate representation and expand around k_0 being much larger than the transferred energies and end up with the following expression

$$|\Psi_{III}\rangle = \sum_{n_0, m, n} c_{n_0}^{(\alpha)} e^{i\tilde{\lambda}T} \langle m| D^\dagger |n\rangle \langle n| D |n_0\rangle e^{-i(n-m)\omega T} \times e^{ik_0 x} e^{i(n_0-m)\frac{\omega}{v_0}x} e^{-i(\omega_0+n_0\omega)t} |m\rangle \quad (2.156)$$

which can be further evaluated by performing the summations in the order indicated by the braces:

$$|\Psi_{III}\rangle = e^{i\tilde{\lambda}T} e^{ik_0 x} e^{-i\omega_0 t} \sum_m \langle m| D^\dagger(\lambda/\hbar\omega) \left(\sum_n |n\rangle \langle n| D(\lambda/\hbar\omega) \left(\sum_{n_0} c_{n_0}^{(\alpha)} |n_0\rangle e^{in_0\frac{\omega}{v_0}x} e^{-in_0\omega t} \right) e^{-in\omega T} \right) e^{-im\frac{\omega}{v_0}x} e^{im\omega T} |m\rangle$$

Thus, we perform the summation over n_0 a first. Using the definition of the coherent state we can write

$$\begin{aligned} \sum_{n_0} c_{n_0}^{(\alpha)} |n_0\rangle e^{in_0\frac{\omega}{v_0}x} e^{-in_0\omega t} &= e^{-|\alpha|^2/2} \sum_{n_0} \frac{\alpha^{n_0}}{\sqrt{n_0!}} |n_0\rangle e^{in_0\frac{\omega}{v_0}x} e^{-in_0\omega t} = \\ &= e^{-|\alpha e^{i\frac{\omega}{v_0}x} e^{-i\omega t}|^2/2} \sum_{n_0} \frac{(\alpha e^{i\frac{\omega}{v_0}x} e^{-i\omega t})^{n_0}}{\sqrt{n_0!}} |n_0\rangle = |\alpha e^{i\frac{\omega}{v_0}x} e^{-i\omega t}\rangle \equiv |\beta\rangle \end{aligned}$$

Apart from its time dependence $e^{-i\omega t}$, the phase factor $e^{in_0\omega x/v_0}$ coming from the neutron part of the wave function can also be absorbed in the coherent state. This works in the coordinate space representation and due to the special form of the coherent state. Note, that the tensorial product has vanished since the coordinate representation has been used. The expression $\langle x_{Neut} \equiv x | \Psi_{III} \rangle$ is a vector in the Hilbert space of the field, i.e. the Fock space, multiplied with the component of the neutron wave vector belonging to the basis vector $|x\rangle$. The action of the displacement operator on a coherent state is well-known [HR2006] and reads for a reel argument

$$D\left(\frac{\lambda}{\hbar\omega}\right) |\beta\rangle = e^{\frac{\lambda}{\hbar\omega}\beta^* - \frac{\lambda}{\hbar\omega}\beta} \left| \beta + \frac{\lambda}{\hbar\omega} \right\rangle = e^{-2i\frac{\lambda|\beta|}{\hbar\omega} \sin(\arg \beta)} \left| \beta + \frac{\lambda}{\hbar\omega} \right\rangle = e^{-i\phi(\beta)} |\gamma\rangle$$

where

$$\phi(\beta) = 2\frac{\lambda|\beta|}{\hbar\omega} \sin(\arg \beta), \quad \gamma = \beta + \frac{\lambda}{\hbar\omega}$$

2. ENERGY EXCHANGE IN A TIME-DEPENDENT MAGNETIC FIELD

We now calculate the sum over n by using

$$\langle n|\gamma\rangle = \langle n|\sum_l c_l^{(\gamma)}|l\rangle = c_n^{(\gamma)} \quad \text{and} \quad \sum_n c_n^{(\gamma)}|n\rangle e^{-in\omega T} = |\gamma e^{-i\omega T}\rangle \equiv |\delta\rangle$$

yielding

$$\sum_n |n\rangle \langle n| e^{-i\phi(\beta)} |\gamma\rangle e^{-in\omega T} = e^{-i\phi(\beta)} \sum_n |n\rangle \langle n|\gamma\rangle e^{-in\omega T} = e^{-i\phi(\beta)} |\delta\rangle$$

The remaining expression for the total wave function reads ($D^\dagger(x) = D(-x)$, $\delta - \lambda/\hbar\omega = \epsilon$)

$$\begin{aligned} |\Psi_{III}\rangle &= e^{i\tilde{\lambda}T} e^{ik_0x} e^{-i\omega_0t} \sum_m \langle m| D(-\lambda/\hbar\omega) e^{-i\phi(\beta)} |\delta\rangle e^{-im\frac{\omega}{v_0}x} e^{im\omega T} |m\rangle = \\ &= e^{i\tilde{\lambda}T} e^{ik_0x} e^{-i\omega_0t} e^{-i\phi(\beta)} \sum_m \langle m| e^{i\phi(\delta)} |\delta - \lambda/\hbar\omega\rangle e^{-im\frac{\omega}{v_0}x} e^{im\omega T} |m\rangle = \\ &= e^{i\tilde{\lambda}T} e^{ik_0x} e^{-i\omega_0t} e^{i(\phi(\delta)-\phi(\beta))} \sum_m \langle m|\epsilon\rangle e^{-im\frac{\omega}{v_0}x} e^{im\omega T} |m\rangle = \\ &= e^{i\tilde{\lambda}T} e^{ik_0x} e^{-i\omega_0t} e^{i(\phi(\delta)-\phi(\beta))} |\zeta\rangle \end{aligned} \quad (2.157)$$

The coherent state can be evaluated by re-inserting the abbreviations

$$\begin{aligned} |\zeta\rangle &= |\epsilon e^{i(\omega T - \frac{\omega}{v_0}x)}\rangle = |(\delta - \frac{\lambda}{\hbar\omega})e^{i(\omega T - \frac{\omega}{v_0}x)}\rangle = \\ &= |(\gamma e^{-i\omega T} - \frac{\lambda}{\hbar\omega})e^{i(\omega T - \frac{\omega}{v_0}x)}\rangle = |(\beta + \frac{\lambda}{\hbar\omega})e^{-i\omega T} - \frac{\lambda}{\hbar\omega})e^{i(\omega T - \frac{\omega}{v_0}x)}\rangle = \\ &= |(\alpha e^{-i\omega t} e^{i\frac{\omega}{v_0}x} + \frac{\lambda}{\hbar\omega})e^{-i\omega T} - \frac{\lambda}{\hbar\omega})e^{i(\omega T - \frac{\omega}{v_0}x)}\rangle = \\ &= |\alpha e^{-i\omega t} + \frac{\lambda}{\hbar\omega} e^{-i\frac{\omega}{v_0}x} - \frac{\lambda}{\hbar\omega} e^{i(\omega T - \frac{\omega}{v_0}x)}\rangle = \\ &= |\alpha e^{-i\omega t} + \frac{\lambda}{\hbar\omega} e^{-i\frac{\omega}{v_0}x} (1 - e^{i\omega T})\rangle \end{aligned}$$

The phase factor ($\phi(\delta) - \phi(\beta)$) can be further simplified as well. Therefore we need the modulus and the phases of δ and β

$$\beta = \alpha e^{-i\omega t} e^{i\frac{\omega}{v_0}x} \implies |\beta| = |\alpha|, \quad \arg \beta = \varphi_\alpha - \omega t + \frac{\omega}{v_0}x \quad (2.158)$$

$$\begin{aligned} \delta &= (\alpha e^{-i\omega t} e^{i\frac{\omega}{v_0}x} + \frac{\lambda}{\hbar\omega})e^{-i\omega T} - \frac{\lambda}{\hbar\omega} = \alpha e^{-i\omega(t+T)+i\frac{\omega}{v_0}x} + \frac{\lambda}{\hbar\omega}(e^{-i\omega T} - 1) \\ |\alpha| \gg \frac{\lambda}{\hbar\omega} &\implies |\delta| \simeq |\alpha|, \quad \arg \delta \simeq \varphi_\alpha - \omega t + \frac{\omega}{v_0}x - \omega T \end{aligned} \quad (2.159)$$

which gives for the phase factor

$$\phi(\delta) - \phi(\beta) = 2\frac{\lambda|\alpha|}{\hbar\omega} \left(\sin\left(\varphi_\alpha - \omega t + \frac{\omega}{v_0}x - \omega T\right) - \sin\left(\varphi_\alpha - \omega t + \frac{\omega}{v_0}x - \omega T\right) \right)$$

Using the addition theorem

$$\sin x - \sin y = 2 \cos \frac{x+y}{2} \sin \frac{x-y}{2}$$

and

$$\cos x = \sin\left(x + \frac{\pi}{2}\right), \quad 2\lambda|\alpha| = \mu B_1, \quad \varphi_\alpha = -\varphi_1$$

we arrive at

$$\phi(\delta) - \phi(\beta) = 2\frac{\mu B_1}{\hbar\omega} \sin \frac{\omega T}{2} \sin \left(\omega t + \varphi_1 - \frac{\omega}{v_0}x + \frac{\omega T}{2} - \frac{\pi}{2} \right)$$

We now use the abbreviations

$$\beta_1 = 2\frac{\mu B_1}{\hbar\omega} \sin \frac{\omega T}{2}, \quad \eta_1 = \varphi_1 + \frac{\omega T}{2} + \frac{\pi}{2}$$

like in section (2.1) and rewrite the whole phase factor by using the Jacobi-Angers expansion and performing an index transformation ($n \Rightarrow -n$)

$$e^{i\beta_1 \sin \left(\omega t + \varphi_1 - \frac{\omega}{v_0}x + \frac{\omega T}{2} - \frac{\pi}{2} \right)} = \sum_{n=-\infty}^{+\infty} J_n(\beta_1) e^{-in\omega t} e^{in\frac{\omega}{v_0}x} e^{-in\eta_1}$$

and insert it into expression (2.157) for $|\Psi_{III}\rangle$

$$|\Psi_{III}\rangle = e^{i\tilde{\lambda}T} \sum_n J_n(\beta_1) e^{-i\omega_0 t} e^{-in\omega t} e^{ik_0 x} e^{in\frac{\omega}{v_0}x} e^{-in\eta_1} |\zeta\rangle \quad (2.160)$$

Performing the expansion of the k -vector in the reverse direction and using the compact notation of sec.(2.1) one gets

$$|\Psi_{III}\rangle = e^{i\tilde{\lambda}T} \sum_n J_n(\beta_1) e^{-i\omega_n t} e^{ik_n x} e^{-in\eta_1} \left| \alpha e^{-i\omega t} + \frac{\lambda}{\hbar\omega} e^{-i\frac{\omega}{v_0}x} (1 - e^{i\omega T}) \right\rangle \quad (2.161)$$

The correlation between the neutron and the magnetic field is now visible from the fact that the neutron's x -coordinate occurs in the coherent field state. Due to the interaction, neutron and field have become entangled. For high mean photon numbers $|\alpha| \gg \lambda/\hbar\omega$, we can neglect this correlation and perform the partial trace over the field state. We then obtain the same result for the neutron's density matrix as in the classical case.

2. ENERGY EXCHANGE IN A TIME-DEPENDENT MAGNETIC FIELD

2.5 Phaseshift picture

Another approach to calculate the phaseshift between the two beams relies on a semiclassical approximation of the path integral formalism [FHS2010, Kle2006], i.e. the Glauber eikonal approximation [Gla1959]. It was originally used in nuclear physics as an asymptotic high-energy approximation to the Lippmann-Schwinger equation in scattering theory, but it can be applied to interferometry as well. If the dimensions of the experiment are macroscopic ($S \gg \hbar$), the integrand in the general expression for the transition amplitude

$$\langle x_a, t_a | x_b, t_b \rangle = \int Dx e^{iS[x]/\hbar} \quad (2.162)$$

oscillates strongly, so that only paths where $\delta S \approx 0$ contribute significantly. This condition is fulfilled by the classical paths. In the interferometric setup depicted

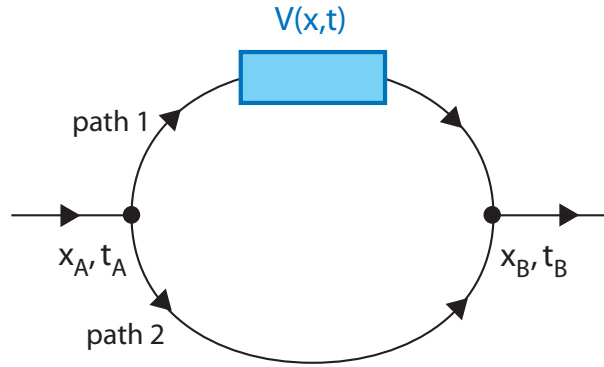


Figure 2.46: Generic picture of an interferometric situation. The particle travels along two different paths. In one of them a potential $V(x, t)$ is present, causing a phase difference $\int V dt$ at x_B .

in fig.2.46, we thus get for the transition amplitude

$$\begin{aligned} \langle x_a, t_a | x_b, t_b \rangle_{\text{IFM}} &= \sum_{n=\text{I,II}} e^{\frac{i}{\hbar} \int_{t_a}^{t_b} L(x_n(t), \dot{x}_n(t), t) dt} \\ &= e^{\frac{i}{\hbar} \int_{t_a}^{t_b} m \frac{\dot{x}_I^2(t)}{2} - V(x_I(t), \dot{x}_I(t), t) dt} + e^{\frac{i}{\hbar} \int_{t_a}^{t_b} m \frac{\dot{x}_{II}^2(t)}{2} dt} \end{aligned} \quad (2.163)$$

If we assume further, that the potential in path I is small compared to the initial kinetic energy, i.e. the velocity and the path of the particle virtually don't change while it is traversing the potential ($x_I \simeq x_{II}$, $\dot{x}_I \simeq \dot{x}_{II}$), we can factor out the kinetic energy term and get for the transition amplitude

$$\langle x_a, t_a | x_b, t_b \rangle_{\text{IFM}} = e^{\frac{i}{\hbar} \int_{t_a}^{t_b} m \frac{\dot{x}_I^2(t)}{2} dt} \left(e^{-\frac{i}{\hbar} \int_{t_a}^{t_b} V(x_I(t), \dot{x}_I(t), t) dt} + 1 \right)$$

Hence, the phase difference between the two path is given by

$$\Delta\varphi = -\frac{1}{\hbar} \int_{t_a}^{t_b} V(x(t), \dot{x}(t), t) dt \quad (2.164)$$

In the case of the spatially restricted, oscillating magnetic field, we have

$$\begin{aligned} \Delta\varphi &= -\frac{\mu}{\hbar} \int_t^{t+T} B(t) dt = -\frac{\mu}{\hbar} \int_t^{t+T} \sum_{i=1}^N B_i \cos(\omega_i t + \varphi_i) dt \\ &= -\sum_{i=1}^N \frac{\mu B_i}{\hbar \omega_i} (\sin(\omega_i(t+T) + \varphi_i) - \sin(\omega_i t + \varphi_i)) \\ &= \sum_{i=1}^N \frac{\mu B_i}{\hbar \omega_i} 2 \sin \frac{\omega_i T}{2} \sin \left(\omega_i t + \varphi_i + \frac{\omega_i T + \pi}{2} \right) \\ &= \sum_{i=1}^N \beta_i \sin(\omega_i t + \eta_i) \end{aligned} \quad (2.165)$$

where T denotes the time of flight through the potential region, and where we used the identities

$$\sin x - \sin y = 2 \cos \frac{x+y}{2} \sin \frac{x-y}{2}, \quad \cos x = -\sin\left(x + \frac{\pi}{2}\right) \quad (2.166)$$

and the previously defined quantities

$$\beta_i = 2\alpha_i \sin \frac{\omega_i T}{2}, \quad \eta_i = \varphi_i + \frac{\omega_i T + \pi}{2} \quad (2.167)$$

In combination with the auxillary phase shifter that also cause a phase shift $\chi = -Nb_c \lambda \Delta D$ in path II because of the optical path difference, we get for the intensity at the third plate, i.e. where the two paths are combined again

$$|\langle x_a, t_a | x_b, t_b \rangle|^2 \propto \frac{1}{2} |1 + e^{i(\chi - \Delta\varphi)}|^2 = 1 + \cos \left(\chi - \sum_{i=1}^N \beta_i \sin(\omega_i t + \eta_i) \right) \quad (2.168)$$

Comparison with the result coming from the solution of the Schrödinger equation (eq.2.80) shows that the only difference is the missing term $x\omega_i/v_0$ in the phase of the cosine. This term arised from the change in the kinetic energy, i.e. the expansion of the k -vector. When we do the Fourier analysis of eq.2.168, we already obtain the Bessel functions in the Fourier coefficients, but the interpretation in form of transition amplitudes for the energy transfer between neutron and magnetic field is not apparent.

2. ENERGY EXCHANGE IN A TIME-DEPENDENT MAGNETIC FIELD

3

Modelling Decoherence with magnetic noise fields

In the preceding chapters, we have dealt with the exchange of energy/photons between a neutron and an oscillating magnetic field. Theoretical calculations for the classical field (sec.2.1) and their experimental demonstration (sec.2.2,2.3) have been investigated in detail. Above that, an quantum field theoretical approach (sec.2.4) and a path integral approximation (sec.2.5) have been presented.

Now, we want to analyze how the interferometer contrast behaves, when the number of modes whose phases are randomly distributed is continuously increased, i.e. when noise fields are applied. We will see that contrast vanishes if the field is sufficiently strong. To build the bridge between the loss of contrast and decoherence theory, we will describe the interferometer in the density matrix formalism, recapitulate the main statements of the theory of open quantum systems and show in which sense noise fields can be used to model decoherence.

3.1 Density matrix formalism in quantum mechanics

In quantum mechanics, the concept of the state vector is ubiquitous. It is a vector of the underlying Hilbert space \mathcal{H} and carries all information about the system. To describe a mixture of different states, the density matrix formalism has to be introduced. If N different, normed states $|\psi_i\rangle$ are prepared with a probability p_i , the density matrix ρ of the ensemble $\{p_i, |\psi_i\rangle\}$ is given by

$$\rho = \sum_{i=1} p_i |\psi_i\rangle \langle \psi_i|, \quad \text{with} \quad \sum_{i=1} p_i = 1 \quad (3.1)$$

3. MODELLING DECOHERENCE WITH MAGNETIC NOISE FIELDS

The condition that the probabilities p_i sum up to one can be formulated more generally by the trace of the density matrix, i.e. $\text{tr}(\rho) = 1$. All axioms of quantum mechanics can be formulated in the density matrix formalism [NC2004]. Representing the states in an arbitrary orthonormal basis, shows that the density matrix contains in general diagonal and off-diagonal entries

$$|\psi_i\rangle = \sum_n a_n^i |n\rangle, \quad \sum_i p_i a_n^{(i)} a_m^{*(i)} \equiv c_{nm} \quad (3.2)$$

$$\implies \rho = \sum_{n,m} c_{nm} |n\rangle \langle m| \quad (3.3)$$

Note, that the incoherent mixture appearing in eq.3.1 should not be confused with a coherent quantum mechanical superposition of different states, the probabilities are real numbers and the density matrix describes a "classical" sum of different states. To illustrate the difference between a superposition and a mixture, we want to give a simple example. Written in the eigenbasis of the Pauli matrix σ_z , denoted as $|\uparrow\rangle$ and $|\downarrow\rangle$, the eigenstate of σ_x belonging to the eigenvalue $+1$ reads in the density matrix formalism

$$\rho = |+\rangle \langle +| = \frac{1}{\sqrt{2}} (|\uparrow\rangle + |\downarrow\rangle) \frac{1}{\sqrt{2}} (\langle\uparrow| + \langle\downarrow|) \quad (3.4)$$

$$= \frac{1}{2} (|\uparrow\rangle \langle\uparrow| + |\uparrow\rangle \langle\downarrow| + |\downarrow\rangle \langle\uparrow| + |\downarrow\rangle \langle\downarrow|) = \frac{1}{2} \begin{pmatrix} 1 & 1 \\ 1 & 1 \end{pmatrix} \quad (3.5)$$

On the other hand, if states $|\uparrow\rangle$ are manipulated by an apparatus in a way that 50% are flipped to $|\downarrow\rangle$, the density matrix describing the outgoing mixture would be

$$\rho = \frac{1}{2} |\uparrow\rangle \langle\uparrow| + \frac{1}{2} |\downarrow\rangle \langle\downarrow| \implies \frac{1}{2} \begin{pmatrix} 1 & 0 \\ 0 & 1 \end{pmatrix} \quad (3.6)$$

The main advantage of the density matrix formalism is that both mixtures and pure states can be described using it. Consequently, it also constitutes the adequate tool for describing the transition between superpositions and classical mixtures of states, a feature that is of main interest in decoherence theory. To see how the density matrix formalism enables us to describe the process of decoherence, we at first take a look at composite systems. The insights gained there will then be used as a starting point for the description of an open quantum system and we will see that the impossibility of isolating a system is the main source for its loss of coherence.

3.2 Physics of composite systems

The Hilbert space \mathcal{H} of a quantum mechanical system consisting of two subsystems A and B is the tensor product of their separate Hilbert spaces \mathcal{H}_A and \mathcal{H}_B

3.2 Physics of composite systems

$$\mathcal{H} = \mathcal{H}_A \otimes \mathcal{H}_B \quad (3.7)$$

Due to the quantum mechanical superposition principle a general state in this Hilbert space can be an arbitrary linear combination of product states

$$|\phi\rangle_{AB} = \sum_{n=1}^{\dim \mathcal{H}_A} \sum_{k=1}^{\dim \mathcal{H}_B} c_{nk} |n\rangle_A |k\rangle_B \quad (3.8)$$

The density matrix needed to describe mixtures in the composite system is of course an element of the set \mathcal{D} of density matrices defined on $\mathcal{H}_A \otimes \mathcal{H}_B$

$$\rho_{AB} = \sum_i p_i |\phi_i\rangle_{AB} \langle \phi_i|_{AB} \quad (3.9)$$

$$\rho_{AB} \in \mathcal{D}(\mathcal{H}) = \mathcal{D}(\mathcal{H}_A \otimes \mathcal{H}_B) \quad (3.10)$$

If one knows the state ρ_{AB} of the composite system, one may ask the question how to extract the behaviour (i.e. the state) of one of the subsystems. A determining condition for the state ρ_A is the relation

$$tr_{AB}(\rho_{AB} \cdot M_A \otimes \mathbb{1}_B) = tr_A(\rho_A \cdot M_A) \quad (3.11)$$

demanding that an operator M_A that acts locally only on one subsystem should yield the same expectation value for the composite system and the subsystem alone. This condition can be fulfilled if one chooses ρ_A to be the partial trace over ρ_{AB}

$$\rho_A := tr_B(\rho_{AB}) = \sum_n \langle n|_B \rho_{AB} |n\rangle_B \quad (3.12)$$

One can show that the resulting ρ_A has indeed all properties of a density matrix ($\rho_A \in \mathcal{D}(\mathcal{H}_A)$) and that taking the partial trace is the only linear operation on ρ_{AB} that fulfills equ.(3.11), i.e. preserves the measurement statistics. Therefore, ρ_A is uniquely determined. Nevertheless one has to bear in mind that the procedure of tracing out the other system can be interpreted as an averaging over all possible states of the not observed system and is thus connected with a loss of information. One cannot reproduce the total state with the reduced states

$$\rho_{AB} \neq tr_B(\rho_{AB}) \otimes tr_A(\rho_{AB}) = \rho_A \otimes \rho_B \quad !!! \quad (3.13)$$

To illustrate the general statements abouts composite quantum systems, we take a look at a composite system consisting of two qubits. Since each qubit

3. MODELLING DECOHERENCE WITH MAGNETIC NOISE FIELDS

lives in a two-dimensional complex vector space, the Hilbert space \mathcal{H} of the total system is $\mathbb{C}^2 \otimes \mathbb{C}^2$. As the canonical basis in each subsystem, we introduce

$$|0\rangle = \begin{pmatrix} 1 \\ 0 \end{pmatrix}, \quad |1\rangle = \begin{pmatrix} 0 \\ 1 \end{pmatrix} \quad (3.14)$$

so that an arbitrary state vector in the subsystem A can be written as

$$|\psi\rangle_A = \sum_{i=0}^1 c_i |i\rangle_A = \begin{pmatrix} c_1 \\ c_2 \end{pmatrix} \quad (3.15)$$

An arbitrary state of the composite system can then consequently be written as

$$|\psi\rangle_{AB} = \sum_{i,j=0}^1 c_{ij} |i\rangle_A \otimes |j\rangle_B, \quad |\psi\rangle_{AB} \in \mathcal{H}, |i\rangle_A \in \mathcal{H}_A, |j\rangle_B \in \mathcal{H}_B \quad (3.16)$$

Usually, one would now define a basis for the overall Hilbert space \mathcal{H} in the following way

$$|0\rangle = |0\rangle_A \otimes |0\rangle_B = \begin{pmatrix} 1 \\ 0 \\ 0 \\ 0 \end{pmatrix} \quad |1\rangle = |0\rangle_A \otimes |1\rangle_B = \begin{pmatrix} 0 \\ 1 \\ 0 \\ 0 \end{pmatrix} \quad (3.17)$$

$$|2\rangle = |1\rangle_A \otimes |0\rangle_B = \begin{pmatrix} 0 \\ 0 \\ 1 \\ 0 \end{pmatrix} \quad |3\rangle = |1\rangle_A \otimes |1\rangle_B = \begin{pmatrix} 0 \\ 0 \\ 0 \\ 1 \end{pmatrix} \quad (3.18)$$

to simplify the notation of the arbitrary state in \mathcal{H}

$$|\psi\rangle_{AB} = \sum_{i=0}^3 c_i |i\rangle, \quad |\psi\rangle_{AB}, |i\rangle \in \mathcal{H}, \quad (3.19)$$

and the arbitrary density matrix in $\mathcal{D}(\mathcal{H})$

$$\rho_{AB} = \sum_{i,j=0}^3 c_{ij} |i\rangle \langle j|, \quad \rho_{AB} \in \mathcal{D}(\mathcal{H}), |i\rangle \in \mathcal{H}, \quad (3.20)$$

But if we want to perform the partial trace over one subsystem the old notation is more adequate. With

$$|i\rangle_A \otimes |j\rangle_B \equiv |ij\rangle, \quad \langle l|_B \otimes \langle k|_A \equiv \langle lk| \quad (3.21)$$

3.2 Physics of composite systems

we write the general expression for a density matrix as

$$\rho_{AB} = \sum_{i,j,k,l=0}^1 c_{ijkl} |ij\rangle \langle lk| \quad (3.22)$$

The partial traces are then given by

$$\begin{aligned} tr_A(\rho_{AB}) &= \sum_{n=0}^1 \langle n|_A \cdot \sum_{i,j,k,l=0}^1 c_{ijkl} |ij\rangle \langle lk| \cdot |n\rangle_A \\ &= \sum_{i,j,k,l=0}^1 \sum_{n=0}^1 c_{ijkl} \langle n|i\rangle |j\rangle_B \langle l|_B \langle k|n\rangle \\ &= \sum_{i,j,k,l,n=0}^1 c_{ijkl} \delta_{ni} |j\rangle_B \langle l|_B \delta_{kn} = \sum_{j,l,n=0}^1 c_{njnl} |j\rangle_B \langle l|_B \end{aligned} \quad (3.23)$$

and

$$tr_B(\rho_{AB}) = \sum_{i,k,n=0}^1 c_{inkn} |i\rangle_A \langle k|_A \quad (3.24)$$

respectively. We now take a look at a specific state of the composite system, namely the maximally entangled Bell-state $|\psi^{++}\rangle$

$$|\psi^{++}\rangle = \frac{1}{\sqrt{2}} (|00\rangle + |11\rangle) \quad (3.25)$$

The density matrix formalism enables us to determine the state of each qubit. The density matrix of the total system reads

$$\rho^{++} = |\psi^{++}\rangle \langle \psi^{++}| = \frac{1}{2} (|00\rangle \langle 00| + |00\rangle \langle 11| + |11\rangle \langle 00| + |11\rangle \langle 11|) \quad (3.26)$$

or in the general notation

$$\rho^{++} = \sum_{i,j,k,l=0}^1 c_{ijkl} |ij\rangle \langle lk|, \quad \begin{array}{l} c_{0000}, c_{0011}, c_{1100}, c_{1111} = \frac{1}{2} \\ c_{ijkl} = 0 \text{ else} \end{array} \quad (3.27)$$

The trace over the subsystems is then given by

$$\begin{aligned} \rho_A &= tr_B(\rho^{++}) = \sum_{i,k,n=0}^1 c_{inkn} |i\rangle_A \langle k|_A = c_{0000} |0\rangle_A \langle 0|_A + c_{1111} |0\rangle_A \langle 0|_A \\ &= \frac{1}{2} (|0\rangle_A \langle 0|_A + |0\rangle_A \langle 0|_A) = \frac{1}{2} \begin{pmatrix} 1 & 0 \\ 0 & 1 \end{pmatrix} \end{aligned} \quad (3.28)$$

3. MODELLING DECOHERENCE WITH MAGNETIC NOISE FIELDS

and

$$\begin{aligned}\rho_B &= \text{tr}_A(\rho^{++}) = \sum_{j,l,n=0}^1 c_{njnk} |i\rangle_B \langle k|_B = c_{0000} |0\rangle_B \langle 0|_B + c_{1111} |0\rangle_B \langle 0|_B \\ &= \frac{1}{2}(|0\rangle_B \langle 0|_B + |0\rangle_B \langle 0|_B) = \frac{1}{2} \begin{pmatrix} 1 & 0 \\ 0 & 1 \end{pmatrix}\end{aligned}\quad (3.29)$$

respectively, showing explicitly that the Kronecker product of the two density matrices of the subsystems does not yield the original density matrix of the composite system

$$\begin{aligned}\rho_A \otimes \rho_B &= \frac{1}{2} \begin{pmatrix} 1 & 0 \\ 0 & 1 \end{pmatrix} \otimes \frac{1}{2} \begin{pmatrix} 1 & 0 \\ 0 & 1 \end{pmatrix} = \frac{1}{4} \begin{pmatrix} 1 \cdot \begin{pmatrix} 1 & 0 \\ 0 & 1 \end{pmatrix} & 0 \cdot \begin{pmatrix} 1 & 0 \\ 0 & 1 \end{pmatrix} \\ 0 \cdot \begin{pmatrix} 1 & 0 \\ 0 & 1 \end{pmatrix} & 1 \cdot \begin{pmatrix} 1 & 0 \\ 0 & 1 \end{pmatrix} \end{pmatrix} \\ \rho_A \otimes \rho_B &= \frac{1}{4} \begin{pmatrix} 1 & 0 & 0 & 0 \\ 0 & 1 & 0 & 0 \\ 0 & 0 & 1 & 0 \\ 0 & 0 & 0 & 1 \end{pmatrix} \neq \frac{1}{2} \begin{pmatrix} 1 & 0 & 0 & 1 \\ 0 & 0 & 0 & 0 \\ 0 & 0 & 0 & 0 \\ 1 & 0 & 0 & 1 \end{pmatrix} = \rho^{++}\end{aligned}\quad (3.30)$$

3.3 Open quantum systems

The results of section 3.2 can be used to describe the dynamics of an open quantum system that is not isolated but interacts with its environment. In this case the total system consists of the observed system and the environment. Hilbert space \mathcal{H} and Hamiltonian H_{SE} are thus given by

$$\mathcal{H} = \mathcal{H}_S \otimes \mathcal{H}_E \quad (3.31)$$

$$H_{SE} = H_S \otimes \mathbb{1} + \mathbb{1} \otimes H_E + H_{int} \quad (3.32)$$

$$H_S \in \mathcal{H}_S; \quad H_E \in \mathcal{H}_E; \quad H_{SE}, H_{int} \in \mathcal{H}$$

where H_{int} denotes the interaction Hamiltonian. The unitary evolution of the total system is governed by the Liouville-van Neumann equation

$$\partial_t \rho_{SE} = \frac{1}{i\hbar} [H_{SE}, \rho_{SE}] \quad (3.33)$$

3.4 Density matrix formalism for the IFM

To get the dynamics of the system alone one has to take the trace over the environmental degrees of freedom

$$\partial_t \rho_S = \frac{1}{i\hbar} \text{tr}_E([H_{SE}, \rho_{SE}]) \quad (3.34)$$

Unfortunately one usually does not know the environment exactly and thus one cannot perform the partial trace. Therefore, one has to develop different strategies to obtain a differential equation for the dynamics of the system alone. Using the Markovian assumption and the theory of quantum mechanical semigroups one can find such a differential equation. The result is a Liouville-van Neumann master equation and in the so called Lindblad form it reads ($\rho_S \equiv \rho$)

$$\partial_t \rho(t) = -i[H(t), \rho(t)] - D[\rho(t)] \quad (3.35)$$

The usual Liouville-van Neumann equation has been expanded by a dissipator term $D[\rho(t)]$ that is given in its most general form via

$$D[\rho(t)] = \frac{1}{2} \sum_k \lambda_k [A_k^\dagger A_k \rho(t) + \rho(t) A_k^\dagger A_k - 2A_k \rho(t) A_k^\dagger] \quad (3.36)$$

The A_k 's are the so called Lindblad operators and there can be maximally $n^2 - 1$ of them where n is the dimension of the system. A detailed derivation of the master equation can be found for example in [BP2002, Hor2009]. The interaction with the environment is now effectively described by additional operators and it can lead to decoherence effects, that means quantum mechanical superpositions in the system are destroyed and only classical mixtures remain. In the density matrix formalism this means vanishing of the off diagonal elements.

3.4 Density matrix formalism for the IFM

To achieve a consistent formalism for the description of quantum states and classical mixtures, the states have to be described with the help of density matrices. We will now try to formulate the physics of the neutron interferometer in terms of the density matrix.

At first, we simplify the treatment of the interferometer by the following consideration: Though the exact behaviour of the neutron beam in the silicon-crystal interferometer requires the use of dynamical diffraction theory [Sea1989, RP1978], it is possible to describe the neutron's path degree of freedom by a qubit [YMK1986, BBKH2001]. The possible states are $|0\rangle$ (denoting the direction of the incoming O-beam) and $|1\rangle$ (denoting the direction of the reflected H-beam). The validity of this simplified approach has been confirmed in tests

3. MODELLING DECOHERENCE WITH MAGNETIC NOISE FIELDS

of quantum mechanics versus realistic-models (violation of a Bell-like inequality [HLB⁺2003], quantum contextuality and Kochen-Specker theorem [BKS⁺2009]). The spin state of the neutron being a spin- $\frac{1}{2}$ particle is described by a qubit as well. Hence, following the approach of [SPE⁺2000], we write the incoming state in front of the first plate as

$$\rho_{\text{in}} = |0\rangle\langle 0| \otimes \rho_{\text{spin}} = \begin{pmatrix} 1 & 0 \\ 0 & 0 \end{pmatrix} \otimes \rho_{\text{spin}} \quad (3.37)$$

denoting an incoming neutron beam in O-direction with in the spin state ρ_{spin} . The action of the whole interferometer setup (see fig.3.1) combines the beam

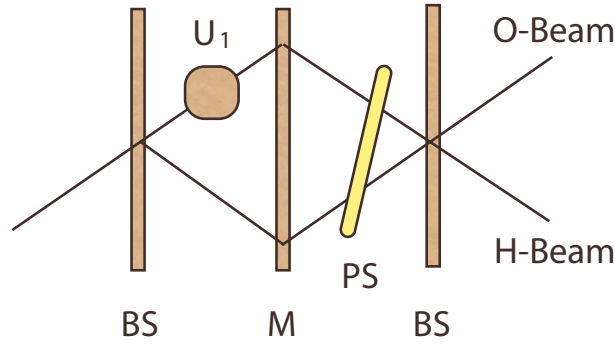


Figure 3.1: Schematic setup for the interferometer (IFM) with a unitary operation in one beam path

splitters (BS), the unitary transformation (U) acting only on the spin part of the wavefunction, the phase shifter (PS) and the mirror (M) yielding, for the output state,

$$\rho_{\text{out}} = U_{\text{BS}} U_{\text{PS}} U_{\text{M}} U U_{\text{BS}} \rho_{\text{in}} U_{\text{BS}}^\dagger U_{\text{M}}^\dagger U_{\text{PS}}^\dagger U_{\text{BS}}^\dagger \quad (3.38)$$

with

$$\begin{aligned} U_{\text{BS}} &= \frac{1}{\sqrt{2}} \begin{pmatrix} 1 & i \\ i & 1 \end{pmatrix} \otimes \mathbb{1}, & U_{\text{M}} &= \begin{pmatrix} 0 & 1 \\ 1 & 0 \end{pmatrix} \otimes \mathbb{1}, \\ U_{\text{PS}} &= \begin{pmatrix} e^{ix} & 0 \\ 0 & 1 \end{pmatrix} \otimes \mathbb{1}, \\ U &= \begin{pmatrix} 1 & 0 \\ 0 & 0 \end{pmatrix} \otimes U_1 + \begin{pmatrix} 0 & 0 \\ 0 & 1 \end{pmatrix} \otimes \mathbb{1} \end{aligned} \quad (3.39)$$

Apart from U , all unitary transformations act on the path qubit and leave the

3.4 Density matrix formalism for the IFM

spin state unchanged. Explicitly, ρ_{out} then reads

$$\begin{aligned} \rho_{\text{out}} = \frac{1}{4} \left\{ \begin{aligned} & \begin{pmatrix} 1 & i \\ -i & 1 \end{pmatrix} \otimes U_1 \rho_{\text{spin}} U_1^\dagger + \begin{pmatrix} e^{-i\chi} & -ie^{-i\chi} \\ -ie^{-i\chi} & -e^{-i\chi} \end{pmatrix} \otimes U_1 \rho_{\text{spin}} \\ & + \begin{pmatrix} e^{i\chi} & ie^{i\chi} \\ ie^{i\chi} & -e^{i\chi} \end{pmatrix} \otimes \rho_{\text{spin}} U_1^\dagger + \begin{pmatrix} 1 & -i \\ i & 1 \end{pmatrix} \otimes \rho_{\text{spin}} \end{aligned} \right\} \quad (3.40) \end{aligned}$$

By tracing over the spin degree of freedom, we get for the path density matrix ρ_{path} with

$$\text{tr}(U_1 \rho_{\text{spin}} U_1^\dagger) = \text{tr}(U_1^\dagger U_1 \rho_{\text{spin}}) = \text{tr}(\rho_{\text{spin}}) = 1 \quad (3.41)$$

$$\text{tr}(U_1 \rho_{\text{spin}}) = |\text{tr}(U_1 \rho_{\text{spin}})| e^{i \arg \text{tr}(U_1 \rho_{\text{spin}})} \equiv a e^{i\xi} \quad (3.42)$$

$$\text{tr}(\rho_{\text{spin}} U_1^\dagger) = \text{tr}(U_1 \rho_{\text{spin}})^* = a e^{-i\xi} \quad (3.43)$$

$$\begin{aligned} \rho_{\text{path}} &= \frac{1}{4} \left\{ \begin{aligned} & \begin{pmatrix} 1 & i \\ -i & 1 \end{pmatrix} \cdot \text{tr}(U_1 \rho_{\text{spin}} U_1^\dagger) + \begin{pmatrix} e^{-i\chi} & -ie^{-i\chi} \\ -ie^{-i\chi} & -e^{-i\chi} \end{pmatrix} \cdot \text{tr}(U_1 \rho_{\text{spin}}) \\ & + \begin{pmatrix} e^{i\chi} & ie^{i\chi} \\ ie^{i\chi} & -e^{i\chi} \end{pmatrix} \cdot \text{tr}(\rho_{\text{spin}} U_1^\dagger) + \begin{pmatrix} 1 & -i \\ i & 1 \end{pmatrix} \cdot \text{tr}(\rho_{\text{spin}}) \end{aligned} \right\} \\ &= \frac{1}{4} \left\{ \begin{aligned} & \begin{pmatrix} 1 & i \\ -i & 1 \end{pmatrix} + \begin{pmatrix} e^{-i\chi} & -ie^{-i\chi} \\ -ie^{-i\chi} & -e^{-i\chi} \end{pmatrix} a e^{i\xi} \\ & + \begin{pmatrix} e^{i\chi} & ie^{i\chi} \\ ie^{i\chi} & -e^{i\chi} \end{pmatrix} a e^{-i\xi} + \begin{pmatrix} 1 & -i \\ i & 1 \end{pmatrix} \end{aligned} \right\} \\ &= \frac{1}{4} \left\{ \begin{aligned} & \begin{pmatrix} 2 & 0 \\ 0 & 2 \end{pmatrix} + a \begin{pmatrix} e^{-i(\chi-\xi)} & -ie^{-i(\chi-\xi)} \\ -ie^{-i(\chi-\xi)} & -e^{-i(\chi-\xi)} \end{pmatrix} \\ & + a \begin{pmatrix} e^{i(\chi-\xi)} & ie^{i(\chi-\xi)} \\ ie^{i(\chi-\xi)} & -e^{i(\chi-\xi)} \end{pmatrix} \end{aligned} \right\} \\ &= \frac{1}{4} \begin{pmatrix} 2 & 0 \\ 0 & 2 \end{pmatrix} + a \begin{pmatrix} 2 \cos(\chi - \xi) & -2 \sin(\chi - \xi) \\ -2 \sin(\chi - \xi) & -2 \cos(\chi - \xi) \end{pmatrix} \\ \rho_{\text{path}} &= \frac{1}{2} \begin{pmatrix} 1 + a \cos(\chi - \xi) & -a \sin(\chi - \xi) \\ -a \sin(\chi - \xi) & 1 - a \cos(\chi - \xi) \end{pmatrix} \quad (3.44) \end{aligned}$$

The spin-independent intensity in the O-direction is given by

$$\begin{aligned} I_O &= \text{tr}(\mathbb{P}_{\text{meas}} \cdot \rho_{\text{out}}) = \text{tr} \left(\begin{pmatrix} 1 & 0 \\ 0 & 0 \end{pmatrix} \otimes \mathbb{1} \cdot \rho_{\text{out}} \right) \\ &= \frac{1}{2} (1 + a \cos(\chi - \xi)) \quad (3.45) \end{aligned}$$

3. MODELLING DECOHERENCE WITH MAGNETIC NOISE FIELDS

where tr denotes the trace over spin and path degree of freedom. The amplitude a of the oscillation is related to the interferometer contrast. By comparison with eq.3.44 we explicitly recognize that a vanishing contrast ($a \rightarrow 0$) indicates a totally mixed path density matrix.

If we apply a magnetic field B pointing in a fixed direction \vec{n}_B with a strength of up to approximately 100 Gauss on the thermal neutron beam ($v \approx 2000\text{m/s}$), the change in kinetic energy can be neglected and the transformation U_1 is given by eq.2.164 reading explicitly

$$U_1(t_i) = \exp \left\{ -i \frac{\mu}{\hbar} \vec{\sigma} \vec{n}_B \int_{t_i}^{t_i+T} B(t) dt \right\} \quad (3.46)$$

where $T = l/v$ denotes the time of flight of the neutron through the field region, l is the length of the field region and v the group velocity of the neutron. The neutron enters the field region at t_i . If the time-of-flight through the magnetic field is considerable shorter than the typical time variation of the field, one can use the quasistatic approximation and replace eq.3.46 by

$$U_1(t_i) = \exp \left\{ -i \frac{\mu}{\hbar} \vec{\sigma} \vec{n}_B T \cdot B(t_i) \right\} \quad (3.47)$$

For unpolarized neutrons one obtains

$$\text{tr}(U_1(t_i) \rho_{\text{spin}}) = \cos \left(\frac{\mu l}{\hbar v} B(t_i) \right) \quad (3.48)$$

Before inserting this expression into eq.3.44, we take into account that $\text{tr}(U_1(t_i) \rho_{\text{spin}})$ is a real number and therefore its argument is either 0 or π what we will use in the following form

$$\begin{aligned} |x| \cos(\chi - \arg x) &= x \cos \chi, & \text{for } x \in \mathbb{R} \\ |x| \sin(\chi - \arg x) &= x \sin \chi, & \text{for } x \in \mathbb{R} \end{aligned}$$

yielding a path density matrix

$$\rho_{\text{path}} = \frac{1}{2} \begin{pmatrix} 1 + C \cos \chi & -C \sin \chi \\ -C \sin \chi & 1 - C \cos \chi \end{pmatrix} \quad (3.49)$$

The new variable C denotes the experimentally measured contrast that results from summation over all N entrance times

$$C = \frac{1}{N} \sum_i \cos \left(\frac{\mu l}{\hbar v} B(t_i) \right) \simeq \frac{1}{T_m} \int_0^{T_m} \cos \left(\frac{\mu l}{\hbar v} B(t) \right) dt \quad (3.50)$$

3.4 Density matrix formalism for the IFM

where T_m denotes the measurement time. Providing a sufficiently long measurement time, the time-integral can be replaced by an integral over the distribution of the field amplitudes, i.e. we switch from time average to ensemble average

$$C = \int_{-\infty}^{+\infty} P(B) \cos\left(\frac{\mu l}{\hbar v} B\right) dB \quad (3.51)$$

A single neutron travels through a region with a constant magnetic field but the whole neutron ensemble sees the amplitude distribution $P(B)$ of the field. If the amplitude distribution is Gaussian with width ΔB and centered around $B_0 = 0$ (and if we are in the quasistatic regime) the contrast is given by

$$\begin{aligned} C &= \int_{-\infty}^{+\infty} \frac{1}{\sqrt{2\pi}\Delta B} e^{-\frac{(B-B_0)^2}{2(\Delta B)^2}} \cos\left(\frac{\mu l}{\hbar v} B\right) dB \\ &= \exp\left\{-\frac{1}{2}\left(\frac{\mu l}{\hbar v}\Delta B\right)^2\right\} \equiv \exp\left\{-\frac{1}{2}(\Delta\phi)^2\right\} \end{aligned} \quad (3.52)$$

where $\Delta\phi$ denotes the standard deviation of the phase fluctuations related to the standard deviation ΔB of the Gaussian noise field. From the expression for the contrast C , it can be concluded that a sufficiently strong noise field leads to a dephased behavior for the whole neutron ensemble. After the third interferometer plate the averaged path-density-matrix then looks like a classical mixture since the intensity no longer oscillates between O- and H-detector.

$$\begin{aligned} \rho_{\text{path}} &= \frac{1}{2} \begin{pmatrix} 1 + e^{-\frac{1}{2}(\Delta\phi)^2} \cos\chi & -e^{-\frac{1}{2}(\Delta\phi)^2} \sin\chi \\ -e^{-\frac{1}{2}(\Delta\phi)^2} \sin\chi & 1 - e^{-\frac{1}{2}(\Delta\phi)^2} \cos\chi \end{pmatrix} \\ &\rightarrow \frac{1}{2} \begin{pmatrix} 1 & 0 \\ 0 & 1 \end{pmatrix} \end{aligned} \quad (3.53)$$

Note, that this (non-unitary) evolution of the neutron path-state is an effective realization of a Lindblad master equation 3.35 with a single dissipator term Γ

$$\dot{\rho} = -\frac{i}{\hbar}[H, \rho] + \Gamma^\dagger \rho \Gamma - \frac{1}{2}(\Gamma^\dagger \Gamma \rho + \rho \Gamma^\dagger \Gamma) \quad (3.54)$$

To reproduce the behaviour of the path density matrix in the IFM, we have to choose the Hamiltonian to be $H = (\alpha/2)\sigma_y$ and the Lindblad operator to be $\Gamma = \sqrt{\lambda/2}\sigma_y$. Both act on the system for a time τ . We then have ($\sigma_y^\dagger = \sigma_y, \sigma_y^2 = \mathbb{1}$)

$$\dot{\rho} = -\frac{i\alpha}{\hbar} \frac{\alpha}{2} [\sigma_y, \rho] + \frac{\lambda}{2} \sigma_y \rho \sigma_y - \frac{\lambda}{2} \rho \quad (3.55)$$

3. MODELLING DECOHERENCE WITH MAGNETIC NOISE FIELDS

This differential matrix equation can be solved most easily in the eigenbasis of σ_y , because then the components of ρ stay uncoupled. With the help of the transformation matrix

$$V = \frac{1}{\sqrt{2}} \begin{pmatrix} i & 1 \\ -i & 1 \end{pmatrix} \quad (3.56)$$

we get for σ_y and the initial state $\rho(0)$

$$\sigma_y = \begin{pmatrix} 0 & -i \\ i & 0 \end{pmatrix}_z \implies V \sigma_y V^\dagger = \begin{pmatrix} 1 & 0 \\ 0 & -1 \end{pmatrix}_y \quad (3.57)$$

$$\rho(0) = |0\rangle\langle 0| = \begin{pmatrix} 1 & 0 \\ 0 & 0 \end{pmatrix}_z \implies V \rho(0) V^\dagger = \frac{1}{2} \begin{pmatrix} 1 & -1 \\ -1 & 1 \end{pmatrix}_y \quad (3.58)$$

In this basis, the Lindblad eq.3.55 reads

$$\begin{pmatrix} \dot{\rho}_{11} & \dot{\rho}_{12} \\ \dot{\rho}_{21} & \dot{\rho}_{22} \end{pmatrix}_y = \begin{pmatrix} 0 & (-\frac{i}{\hbar}\alpha - \lambda)\rho_{12} \\ (+\frac{i}{\hbar}\alpha - \lambda)\rho_{21} & 0 \end{pmatrix}_y \quad (3.59)$$

and is solved for the initial state $\rho(0)$ by

$$\rho = \begin{pmatrix} \rho_{11} & \rho_{12} \\ \rho_{21} & \rho_{22} \end{pmatrix}_y = \frac{1}{2} \begin{pmatrix} 1 & -e^{-\lambda t} e^{-\frac{i}{\hbar}\alpha t} \\ -e^{-\lambda t} e^{+\frac{i}{\hbar}\alpha t} & 1 \end{pmatrix}_y \quad (3.60)$$

The back transformation into the ($|0\rangle, |1\rangle$)-basis (= eigenstates of σ_z) is given in general by

$$V^\dagger (\rho_{ij})_y V = \frac{1}{2} \begin{pmatrix} \rho_{11} + \rho_{22} - (\rho_{12} + \rho_{21}) & -i(\rho_{11} - \rho_{22} + (\rho_{12} - \rho_{21})) \\ i(\rho_{11} - \rho_{22} - (\rho_{12} - \rho_{21})) & \rho_{11} + \rho_{22} + (\rho_{12} + \rho_{21}) \end{pmatrix}_z \quad (3.61)$$

and yields for ρ at time τ

$$\rho(\tau) = \frac{1}{2} \begin{pmatrix} 1 + e^{-\lambda\tau} \cos \alpha\tau & -e^{-\lambda\tau} \sin \alpha\tau \\ -e^{-\lambda\tau} \sin \alpha\tau & 1 - e^{-\lambda\tau} \cos \alpha\tau \end{pmatrix} \quad (3.62)$$

where we have omitted the index z now. Identifying the rotation angle $\alpha\tau$ with the angle χ and the damping factor $\lambda\tau$ with $(\Delta\phi)^2/2$, the correspondence of eq.3.53 and eq.3.35 is clearly visible. In the Bloch vector picture, the empty interferometer thus causes a rotation of Bloch vector, and applying the noise shrinks the Bloch vector. For a sufficiently strong noise signal, the Bloch vector collapses into the origin.

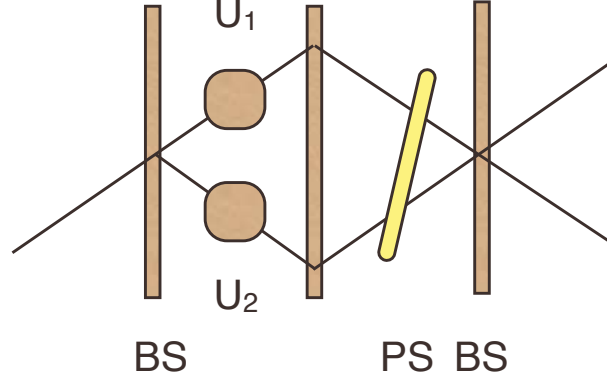


Figure 3.2: Schematic setup for the interferometer (IFM) with unitary operations in both beam paths.

If transformations are applied in both beam parts (see fig.3.2), an analogue calculation where

$$U = \begin{pmatrix} 1 & 0 \\ 0 & 0 \end{pmatrix} \otimes U_1 + \begin{pmatrix} 0 & 0 \\ 0 & 1 \end{pmatrix} \otimes U_2 \quad (3.63)$$

yields for the intensity in the O-beam

$$I_O = \text{Tr} (P_{\text{meas}} \cdot \rho_{\text{out}}) = \frac{1}{2} (1 + b \cos(\chi - \xi)) \quad (3.64)$$

with $b e^{i\xi} = \text{tr} (U_2^\dagger U_1 \rho_{\text{spin}})$. For two time-dependent magnetic fields the expression $U_2^\dagger U_1$ has the form

$$U_2^\dagger U_1 = \exp \left\{ i \frac{\mu}{\hbar} \vec{\sigma} \int_{t_i}^{t_i+T} \left(\vec{B}_2 \left(t - \frac{\Delta x}{v} \right) - \vec{B}_1(t) \right) dt \right\} \quad (3.65)$$

where $\Delta x = x_1 - x_2$ denotes the difference between the length of the two beam paths from the first interferometer plate to the position where the transformation U_i takes places (e.g. position of the coils). The resulting contrast for unpolarized neutrons and quasistatic fields is given by

$$C = \frac{1}{T_m} \int_0^{T_m} \cos \left(\frac{\mu l}{\hbar v} \left[B_2 \left(t - \frac{\Delta x}{v} \right) - B_1(t) \right] \right) dt \quad (3.66)$$

3. MODELLING DECOHERENCE WITH MAGNETIC NOISE FIELDS

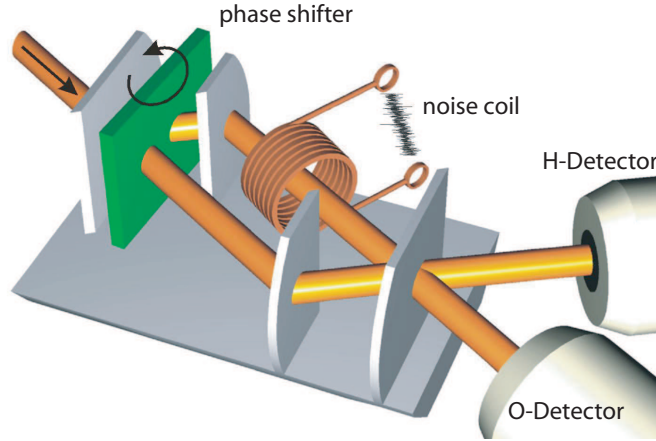


Figure 3.3: Setup for experiments in position space (phase shifts are smaller than the coherence length, intensity oscillates between the two detectors)

3.4.1 Experimental verification

For the experimental realization of the theoretical results in case of one unitary operation, we apply Gaussian white magnetic noise in one interferometer arm with the field pointing in beam direction (for preliminary results of such measurements see [BRS2003, Bar2005]). The field is generated by a fluctuating current in a coil connected to a Tektronix random signal generator AFG 3022b. The length l of the effective field region is 42.65mm. For neutrons with a mean wave length of $\lambda = 1.92\text{\AA}$ ($\delta\lambda/\lambda \simeq 0.01$) this leads to a time-of-flight of about $20.7\mu\text{s}$. The beam cross section of 6×8 mm is much smaller than the cross section of the coil (22×30 mm), so that we can neglect field changes perpendicular to the flight direction. To stay in the quasistatic regime, the frequency bandwidth of the noise has to be restricted. In our case, the time of flight $T = 20.7\mu\text{s}$ corresponds to a frequency of about 50kHz, so that the upper limit of the noise frequency bandwidth should not exceed 5kHz. The detailed characteristics of the input signal are shown in fig.3.4.

In order to compensate loss of contrast that is not due to the magnetic noise field (mainly induced by temperature fluctuations and mechanical vibrations) on/off contrast measurements have been performed. For each position of the phase shifter, the intensity is measured with and without noise (see fig.3.5). The contrasts of the resulting oscillations are determined ($C = (I_{max} - I_{min}) / (I_{max} + I_{min})$) and their quotient gives the relative contrast. The strength of a Gaussian noise is indicated by the width ΔB of the amplitude distribution. The contrast is measured for increasing field strengths and then compared with the theoretically expected curve in the quasistatic regime verifying the $\exp(-(\Delta\phi)^2/2)$ -dependence

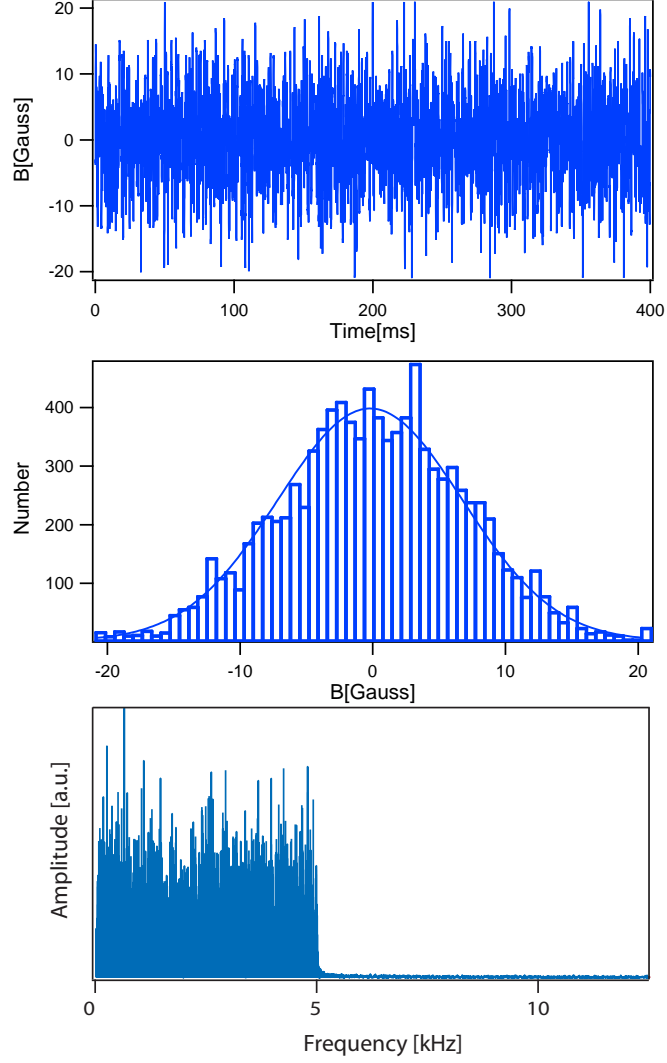


Figure 3.4: The applied noise signal on a 100ms time scale. Its corresponding histogram shows the Gaussian amplitude distribution. The frequencies are uniformly distributed from 0-5 kHz, ensuring the condition of quasistatics

of the contrast with high accuracy (see fig.3.6). If the bandwidth is enlarged the contrast reduction happens slower, i.e. a stronger field is needed to achieve a full incoherent behaviour. The phase shift depends on the integral over the magnetic field B over a time interval T (see eq.3.46). Higher frequencies oscillate stronger and the value of the integral decreases. The exponential decay of the contrast is weakened $C = \exp(-\gamma(\Delta\phi)^2/2)$, described by a fit parameter $\gamma < 1$. A more detailed analysis, relying on the formulas found for the fields with a low mode

3. MODELLING DECOHERENCE WITH MAGNETIC NOISE FIELDS

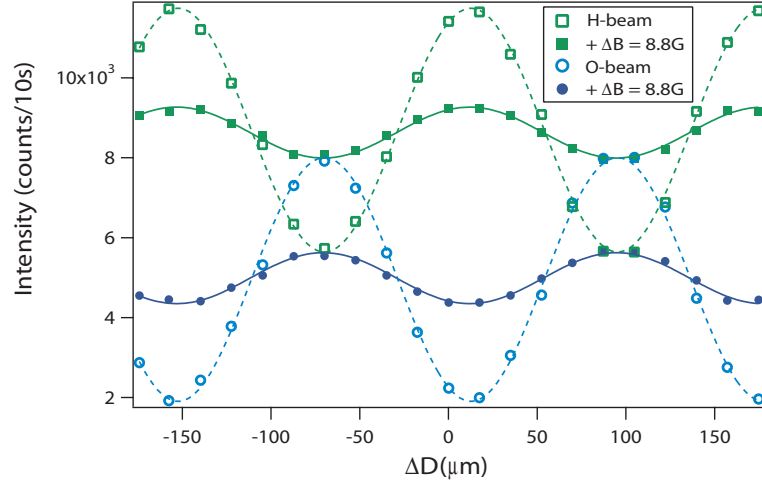


Figure 3.5: Characteristic interference pattern for noise on/off measurement. Oscillations are damped by the fluctuating field. Error bars are of comparable size as the markers and have been omitted.

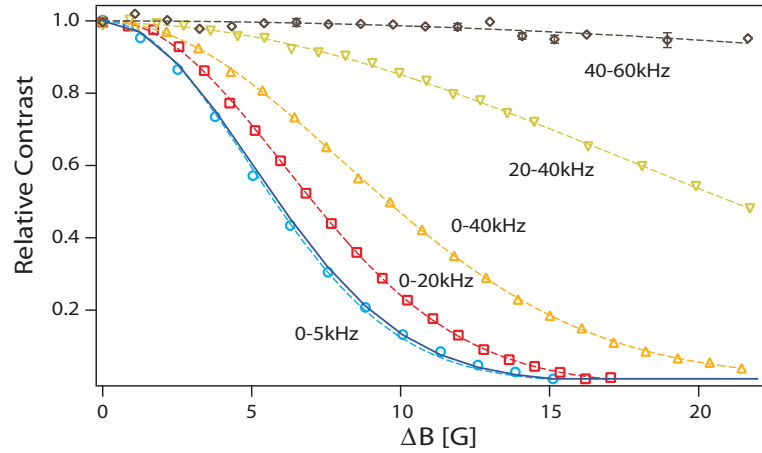


Figure 3.6: Loss of contrast as a function of the standard deviation of the Gaussian distributed field amplitudes caused by magnetic noise with different frequency bandwidths Δf . The dashed lines are exponential fits whereas the solid line represents the theory curve in the quasistatic regime. Error bars of comparable size as the markers have been omitted.

number (sec. 2.1 and 2.5) will be given in chapter 4. If the lower frequencies are excluded totally, contrast reduction is even more suppressed as illustrated for frequency bandwidths from 20-40 kHz and 40-60 kHz in fig.3.6.

By applying a second noise source, i.e. adding a coil in the second beam

3.4 Density matrix formalism for the IFM

path (see fig.3.7) the loss of contrast can be enforced or weakened. The loss

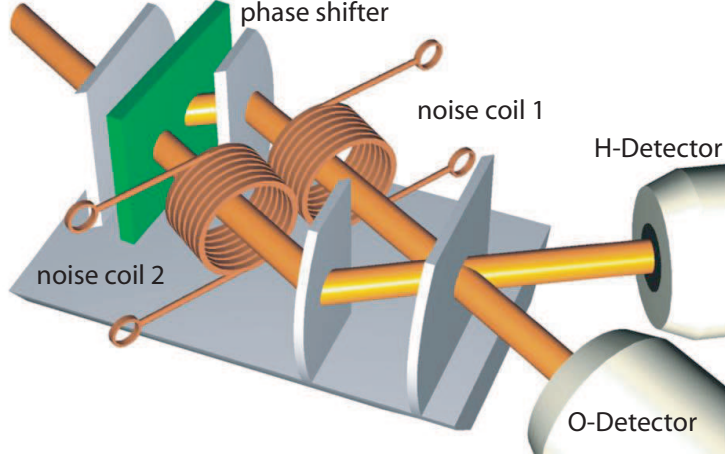


Figure 3.7: Experimental setup with 2 coils

of contrast can be completely reversed if an identical coil driven by the same signal is inserted. If the positions of the two coils in the interferometer are not symmetric an additional time delay Δt has to be implemented to compensate for the position difference Δx . eq.3.66 then becomes ($\phi_i = \frac{\mu}{\hbar} \frac{l}{v} B_i$)

$$C = \frac{1}{T_m} \int_0^{T_m} \cos \left(\phi_2 \left(t + \Delta t - \frac{\Delta x}{v} \right) - \phi_1(t) \right) dt \quad (3.67)$$

For identical, synchronized noise signals ($\phi_1 = \phi_2 = \phi$ and $\Delta t = \Delta x/v$) recovery of full contrast can be achieved ($C = 1$) and has been experimentally verified (see fig.3.8). For identical, unsynchronized noise, or two completely different noise signals, the dephasing process is enforced. For different signals with the same frequency bandwidth Δf , the $e^{-\frac{1}{2}\gamma(\Delta\phi_i)^2}$ -factors of the two Gaussian noise fields contribute multiplicatively to the contrast (see fig.3.9)

$$C = \exp \left\{ -\frac{1}{2}\gamma \left((\Delta\phi_1)^2 + (\Delta\phi_2)^2 \right) \right\} \quad (3.68)$$

In the quasistatic case ($\gamma = 1$), this formula results from averaging over an uncorrelated two-dimensional Gaussian distribution for B_1 and B_2 with mean values $B_1^0 = B_2^0 = 0$, correlation coefficient $\sigma_{12} = 0$, and standard deviations ΔB_1 and ΔB_2 .

$$C = \int \int P(B_1, B_2) \cos \left(\frac{\mu}{\hbar} \frac{l}{v} (B_2 - B_1) \right) dB_1 dB_2 \quad (3.69)$$

3. MODELLING DECOHERENCE WITH MAGNETIC NOISE FIELDS

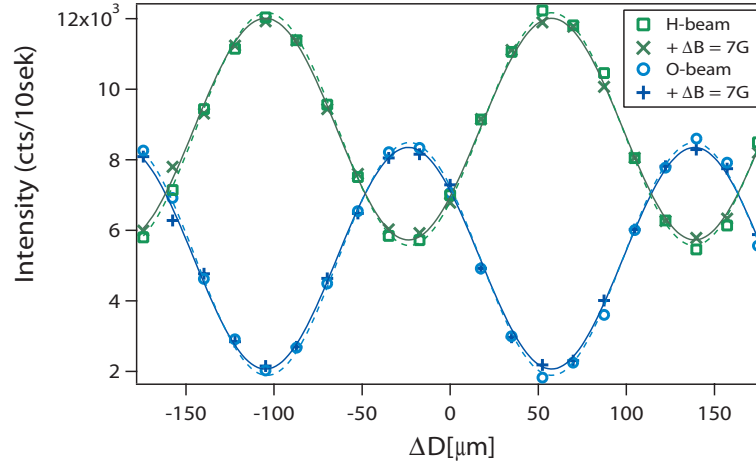


Figure 3.8: Interferogram for identical synchronized noise in both arms. Contrast remains when noise is turned on.

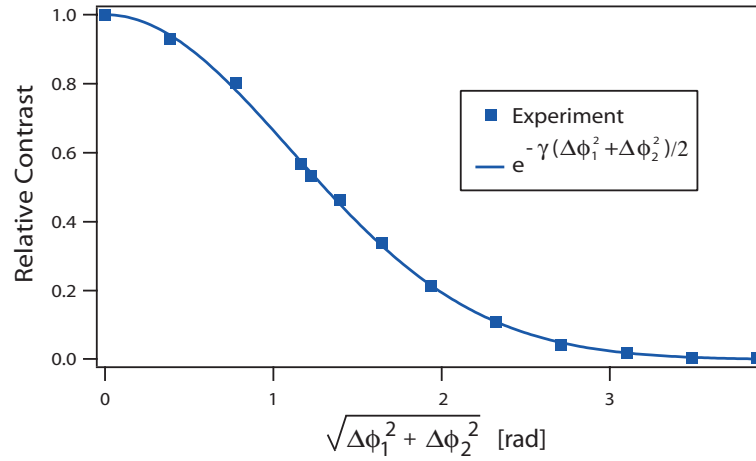


Figure 3.9: Contrast for independent noise sources in the coils plotted against $\sqrt{\Delta\phi_1^2 + \Delta\phi_2^2}$.

where

$$P(B_1, B_2) = N \times \exp \left\{ -\beta \left(\left(\frac{B_1}{\Delta B_1} \right)^2 - 2\sigma_{12} \left(\frac{B_1}{\Delta B_1} \right) \left(\frac{B_2}{\Delta B_2} \right) + \left(\frac{B_2}{\Delta B_2} \right)^2 \right) \right\} \quad (3.70)$$

3.4 Density matrix formalism for the IFM

with

$$N = \frac{1}{2\pi\Delta B_1\Delta B_2\sqrt{1-\sigma_{12}^2}}, \quad \beta = \frac{1}{2\sqrt{1-\sigma_{12}^2}}$$

For fully correlated noise signals ($\sigma_{12} \rightarrow 1$) follows $\int P(B_1, B_2)dB_2 \rightarrow \delta(B_1 - B_2)$ and eq.3.69 reproduces the result of eq.3.67 for the synchronized case.

The fully uncorrelated case can also be understood in a simpler picture: the phaseshifts ϕ_1 and ϕ_2 caused by the two magnetic noise fields are Gaussian distributed random variables with mean 0 and variances $\Delta\phi_1^2$ and $\Delta\phi_2^2$. The resulting relative phaseshift $\phi = \phi_1 - \phi_2$ between the two beams is thus also Gaussian distributed with mean $0 - 0 = 0$ and variance $\Delta\phi^2 = \Delta\phi_1^2 + \Delta\phi_2^2$. It is a general property of Gaussian distributed random variables that their sum is also Gaussian distributed and that their means and variances add up. That's also true for their differences. In our case with mean value 0, $-\phi_2$ is even described by exactly the same probability distribution as ϕ_2 .

If identical noise signals are applied, one can determine the relative position of the coils in the interferometer by scanning through different time delays and measuring the contrast. Maximum recovery of contrast is achieved when the time delay equals the ratio of position difference and neutron velocity $\Delta x/v$. If the coils are shifted relative to each other, the maximum is shifted as well (see fig.3.10).

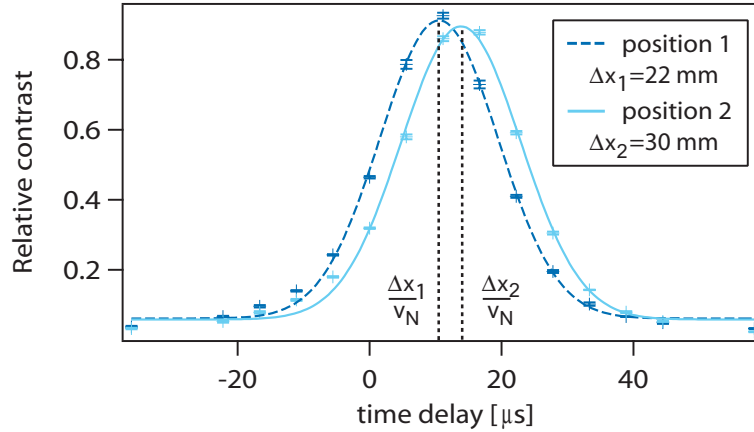


Figure 3.10: Contrast for the same noise in the two coils but different relative positions Δx_i plotted as function of the time delay in one coil.

The contrast is determined by the cosine of the difference of the two phase shifts in each beam path (see eq.3.67). Expanding the cosine near $\Delta t = \Delta x/v$ reveals the autocorrelation function of the noise signal. If the signal is shifted

3. MODELLING DECOHERENCE WITH MAGNETIC NOISE FIELDS

further, higher terms in the cosine expansion have to be considered and higher order autocorrelation terms occur as well. Using a broader frequency bandwidth for the incoming noise signal narrows the autocorrelation function (see fig.3.11). For ideal white noise it would become a Dirac delta function $\delta(t - \Delta x/v)$.

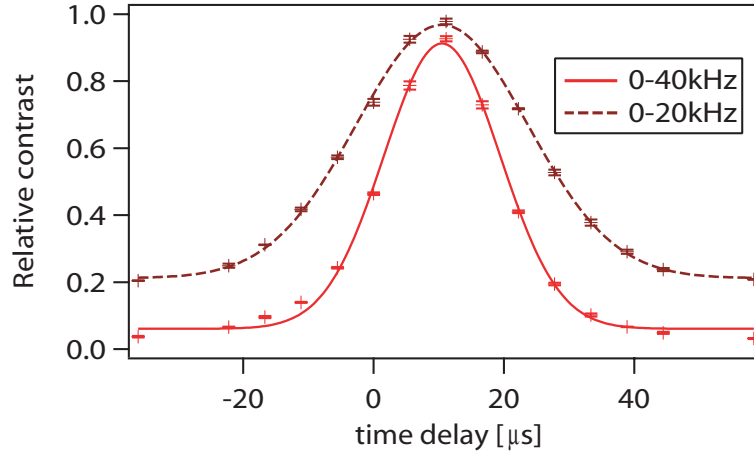


Figure 3.11: The two coils in the interferometer are driven with the same noise signal. The contrast is plotted for different frequency bandwidths against the time delay in one coil.

All these experiments show, that the classical noise field can be used to effectively model decoherence, though an irreversible loss of coherence as it appears in the interaction between two quantum systems can not be achieved. Still, the randomly distributed phase shifts constitute an alternative approach to explain the effects of an environment on a quantum system. In the interferometric setup, the procedure of tracing out the environmental degrees of freedom and the statistical accumulation of randomly distributed phase shifts are completely equal [SAI1990].

3.4.2 Momentum modulation measurements

3.4.2.1 Theory

After the observations off the coherence properties of the neutron beam in the standard interferometric setup, the magnetic noise-field is used now to investigate the dephasing of macroscopically distinguishable states, in particular whether their increasing spatial separation increases their sensitivity to external disturbances [WM1985, Zur1991, BP2002]. Schrödinger cat-like states can be produced in the interferometer with thick aluminum phase-shifters that shift the wave packets further than their coherence lengths that is in the order of 10\AA [JWR1994,

3.4 Density matrix formalism for the IFM

[Rau1995](#), [BRS2003](#)]. The two wavepackets travelling through the IFM are separated by a distance $\Delta_x = Nb_c\lambda^2 D/2\pi$ where N denotes the atom density, b_c the coherent scattering length of aluminum, D the phase shifter thickness and λ the neutron wave length. For Al-phase shifters of centimeter thickness, the separation width amounts to several 100Å so that there is practically no overlap in position space at the third IFM plate anymore. Nevertheless, they are still in a quantum state described by

$$\psi_{sup}(x, t) = \psi_I(x, t) + \psi_{II}(x, t) = \psi_0(x, t) + \psi_0(x + \Delta_x, t) \quad (3.71)$$

where ψ_I, ψ_{II} denote the wavepackets arriving from beam path I and II respectively. In good approximation they keep the same form ψ_0 , the aluminum slab only shifts the whole wavepacket. Thus, both have the same Fourier spectrum $\alpha_0(k)$. The interference properties are then exhibited in momentum space

$$\begin{aligned} \psi_{sup}(x, t) &= \psi_0(x, t) + \psi_0(x + \Delta_x, t) \\ \int \alpha_{sup}(k) e^{ikx} dk &= \int \alpha_0(k) e^{ikx} + \alpha_0(k) e^{ik(x+\Delta_x)} dk \\ \implies \alpha_{sup}(k) &= \alpha_0(k) + e^{ik\Delta_x} \alpha_0(k) \\ |\alpha_{sup}(k)|^2 &= |\alpha_0(k)|^2 (1 + \cos(k\Delta_x)) \end{aligned} \quad (3.72)$$

In the Wigner-function representation [[Wig1932](#), [Sud2005](#)]

$$W_{sup}(x, k) = \frac{1}{2\pi\hbar} \int_{-\infty}^{+\infty} \psi^\dagger(x + \frac{y}{2}) \psi(x - \frac{y}{2}) e^{iky} dy \quad (3.73)$$

both spatial separation and intensity modulation in momentum space are clearly visible (see [fig.3.12](#)).

We now expose this Schrödinger cat-like state to a magnetic noise in one arm of the interferometer causing a field-dependent phase shift.

$$\psi_{sup}(B, x, t) = e^{i\phi(B)} \psi_0(x, t) + \psi_0(x + \Delta_x, t) \quad (3.74)$$

In the quasistatic regime we can evaluate the resulting Wigner-function by averaging over the Gaussian distribution of the noise field,

$$\bar{W}(B, x, k, t) = \int_{-\infty}^{+\infty} P(B) W_{sup}(B, x, k, t) dB \quad (3.75)$$

which effects a smearing of the central wiggle structure of the Wigner function, leaving the separated wave packets nearly unchanged. Integrating over x yields the probability distribution in momentum space

$$|\alpha_{sup}(k)|^2 = |\alpha_0(k)|^2 \left(1 + e^{-\frac{1}{2} \frac{\mu l^2}{\hbar v^2} (\Delta B)^2} \cos(\Delta_x k) \right) \quad (3.76)$$

3. MODELLING DECOHERENCE WITH MAGNETIC NOISE FIELDS

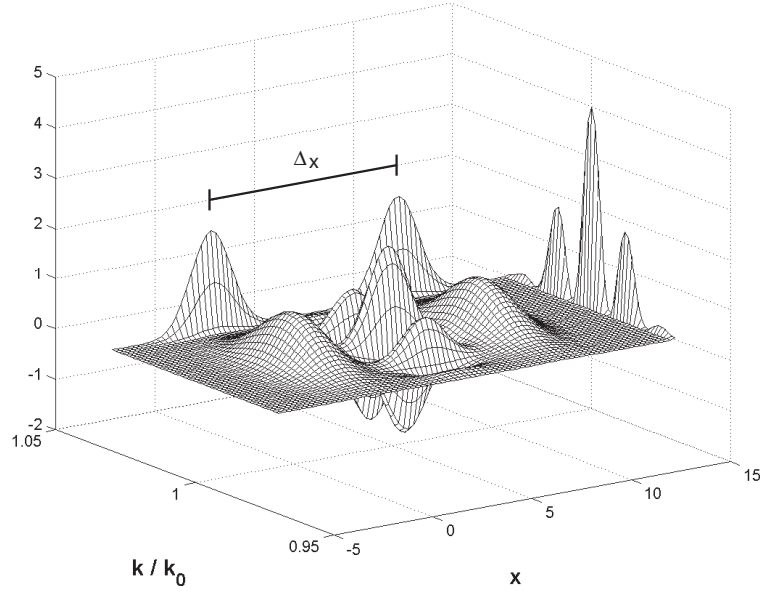


Figure 3.12: Wigner-function for the macroscopically separated cat-like state (x in arbitrary units)

The spatial separation Δ_x does not enter the expression for the contrast but only the standard deviation ΔB of the magnetic noise field. The loss of contrast is not affected by the separation width of the two Gaussian wave packets.

Note, that we again neglected the energy transfer between the magnetic field and the neutron because it lies several orders of magnitude below the length of the modulation period λ_{period} . It can be calculated by expanding the cosine around the mean wavelength λ_0 and then determining for which $\Delta\lambda$ the argument was augmented by 2π

$$\begin{aligned} \cos(k\Delta_x) &= \cos\left(\frac{2\pi}{\lambda}\Delta_x\right) = \cos\left(\frac{2\pi}{\lambda_0 + \Delta\lambda}\Delta_x\right) = \cos\left(\frac{2\pi}{\lambda_0}\left(1 + \frac{\Delta\lambda}{\lambda_0}\right)\Delta_x\right) \\ \frac{\lambda_{period}}{\lambda_0^2}\Delta_x &\doteq 1 \implies \lambda_{period} = \frac{\lambda_0^2}{\Delta_x} \end{aligned} \quad (3.77)$$

The modulation period λ_{period} is given by the ratio of the mean wavelength λ_0 and the interference order $n = \Delta_x/\lambda_0$. For our experimental parameters ($\lambda_0 \approx 2\text{\AA}$, Δ_x several 100\AA), it amounts to $\lambda_0/n \simeq 10^{-2}\text{\AA}$ whereas a shift of the wavelength corresponding to the exchange of a photon with 100kHz amounts to

$$\lambda_{shift} \simeq \frac{1}{2} \frac{\Delta E}{E} \lambda_0 = \frac{1}{2} \frac{\hbar\omega}{E_{kin}} \lambda_0 \simeq 10^{-8}\text{\AA} \quad (3.78)$$

Thus, the modulation pattern is practically not influenced by the altered neutron velocities. Under these conditions, the separation width has no influence on the contrast reduction.

3.4.2.2 Experiment

In the experimental setup we prepared three different Schrödinger cat-like states by using three different aluminum phase shifters with thicknesses of 18, 27 and 36nm, which caused a packet separation of 212, 318 and 424Å. To access k -space a silicon analyzer crystal that selects wavelengths from 1.88Å to 1.96Å via Bragg-reflection and a third detector were used (see fig.3.13 for schematic setup and fig.3.14 for the crystal).

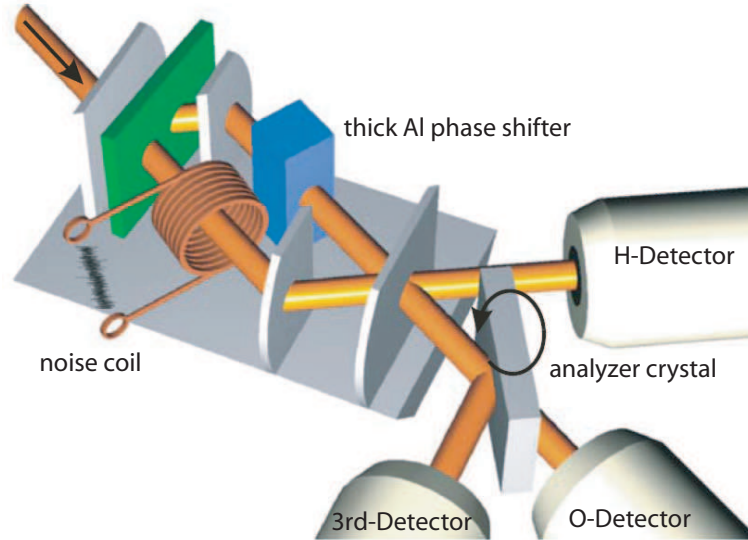


Figure 3.13: Schematic setup for interference measurements in momentum space with aluminum phase shifter, intensity oscillates in the wavelength spectrum recorded with the 3rd detector.

First we determined the wavelength distribution $|\alpha_0(\lambda)|^2$ for the empty interferometer (the dashed black line in fig.3.15 a). The measured intensity is normalized by the total number of counts in the O-beam (O-detector + 3rd detector). Then the Al-phase-shifter was inserted causing a modulation of that spectrum (the curves for $\Delta B = 0$ in fig.3.15 a). Turning on the magnetic noise leads to damped modulations. After dividing the modulated spectra by $|\alpha_0(\lambda)|^2$, one gets standard interferograms in cosine-form whose contrast can be determined easily (see fig.3.15 b).

3. MODELLING DECOHERENCE WITH MAGNETIC NOISE FIELDS

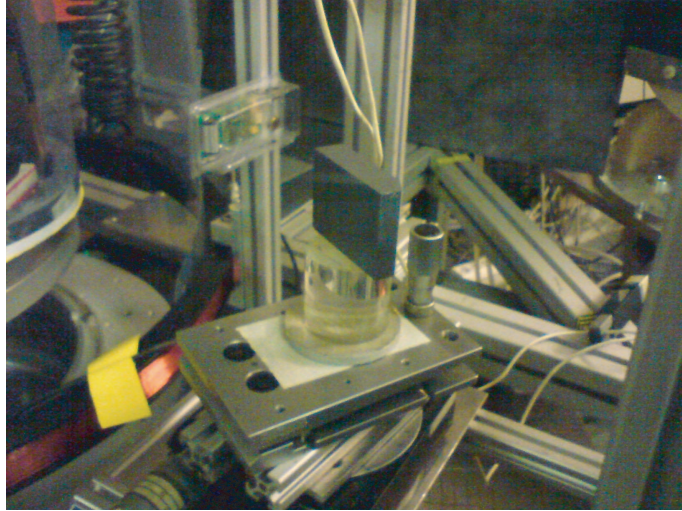


Figure 3.14: Silicon analyzer crystal used for selection of different wavelengths.

In this way, the relative contrast was measured for different field strengths $\Delta B \simeq 0 - 15G$. In fig.3.16, one can see how the momentum modulation gets smeared out with increasing noise strength and converges towards the wavelength distribution of the empty interferometer.

Then, an Al-phaseshifter with an other thickness causing a different separation width was inserted and the effect of the increased noise is investigated again (see as examples for the 27mm phase shifter fig.3.17 and fig.3.18 for the 36mm phase shifter).

The results for the three different separation widths are illustrated together in fig.3.19 showing that the loss of contrast is independent of the separation width.

Differences to the results of, for example [Zur1991], also arise from the different interaction Hamiltonians. In [Zur1991], a dipole interaction of the form $\hat{H}_{int} = \epsilon \hat{x} \frac{d\phi(t)}{dt}$ is assumed that contains the position operator \hat{x} explicitly. This leads to stronger decoherence for increasing spatial separation Δ_x of the Gaussian wave packets. In our case the interaction between neutron and field is given by $\hat{H}_{int} = -\mu \vec{\sigma} \vec{B}$ and "happens" in spin space. Under quasistatic approximation and neglectable energy transfer only the strength of the field fluctuation ΔB occurs in the expression for the contrast.

In agreement with [RSP1999], one can show that the coherent preparation of the macroscopically distinct Schrödinger cat-like states becomes more and more difficult with increasing separation width. The values of the off-contrast decrease (see Table 3.1) due to the inhomogeneities of the phaseshifters. But this concerns

3.4 Density matrix formalism for the IFM

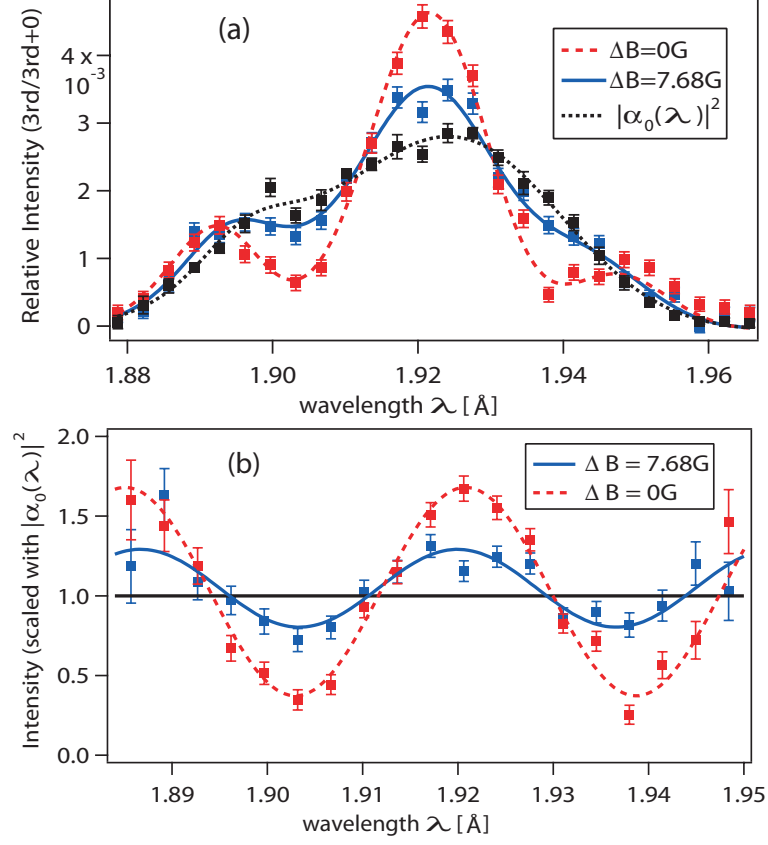


Figure 3.15: Interferogram in momentum space, wavelength distribution $|\alpha_0(\lambda)|^2$ of the empty interferometer and original on/off wavelength spectra for $\Delta_x = 212\text{Å}$ (a) and on/off-curves divided by $|\alpha_0(\lambda)|^2$ (b).

only the preparation of the state, it is not a statement about its principal stability. As shown in 3.19, the loss of contrast due to magnetic noise is the same for each separation width.

Moreover, if we compare the loss of contrast in the standard interferometric setup with the averaged decoherence curve in momentum space, we see that they are practically identical within the measurement accuracy (see fig.3.20).

3. MODELLING DECOHERENCE WITH MAGNETIC NOISE FIELDS

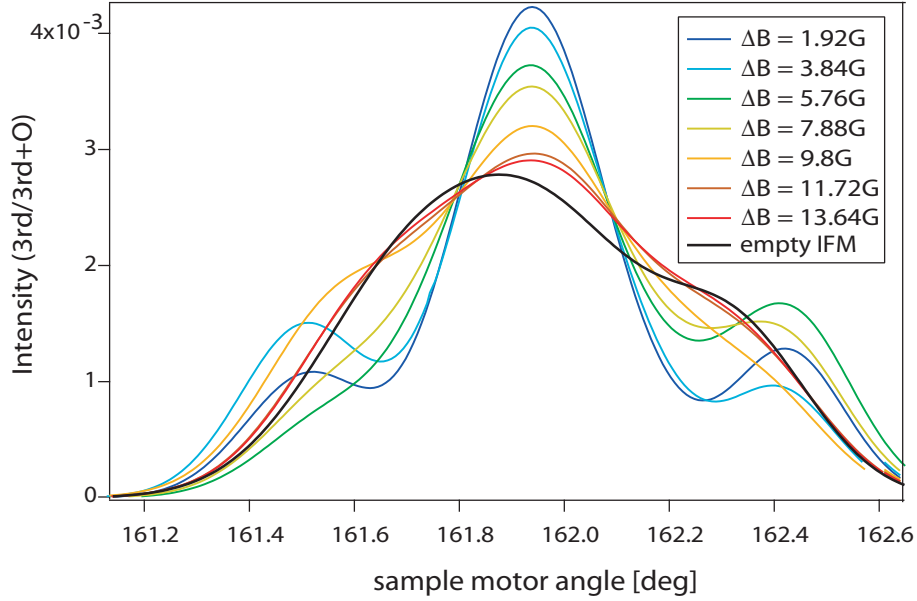


Figure 3.16: Interferogram in momentum space for the 18mm phase shifter (wave packet separation $\Delta_x = 212\text{\AA}$) for increasing noise strength ΔB plotted against the angle of analyzer crystal.

phaseshift	$\Delta_x = 212\text{\AA}$	$\Delta_x = 318\text{\AA}$	$\Delta_x = 424\text{\AA}$
Off-Contrast	$60.0 \pm 1.1\%$	$55.4 \pm 1.1\%$	$44.4 \pm 1.3\%$

Table 3.1: Decrease of (mean) Off-Contrast values for thick phase-shifters

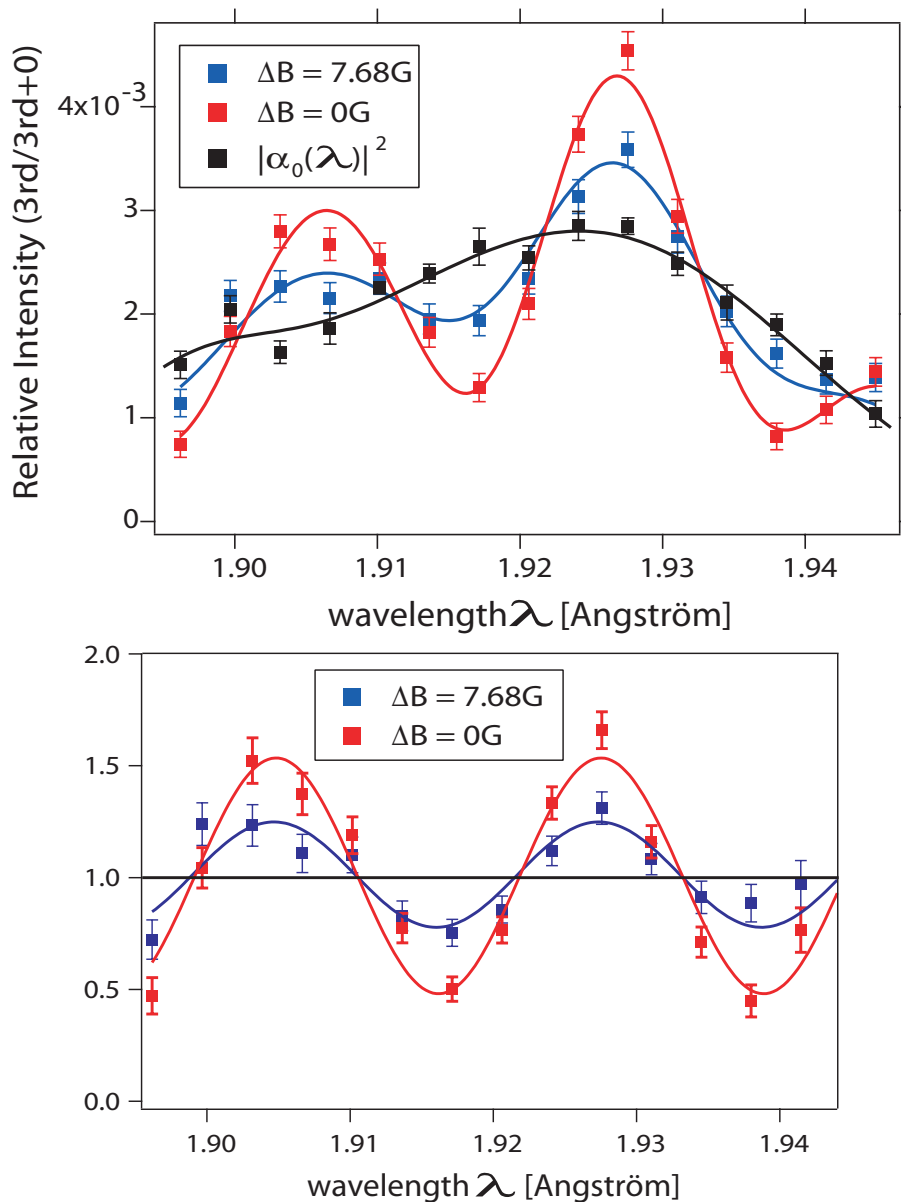


Figure 3.17: Interferogram in momentum space, wavelength distribution $|\alpha_0(\lambda)|^2$ of the empty interferometer and original on/off wavelength spectra for $\Delta_B = 7.86\text{G}$ for the 27mm Al-phase shifter causing a wave packet separation of $\Delta_x = 318\text{Å}$ (upper diagram) and on/off-curves divided by $|\alpha_0(\lambda)|^2$ exhibiting a standard interferogram in cosine-shape (lower diagram).

3. MODELLING DECOHERENCE WITH MAGNETIC NOISE FIELDS

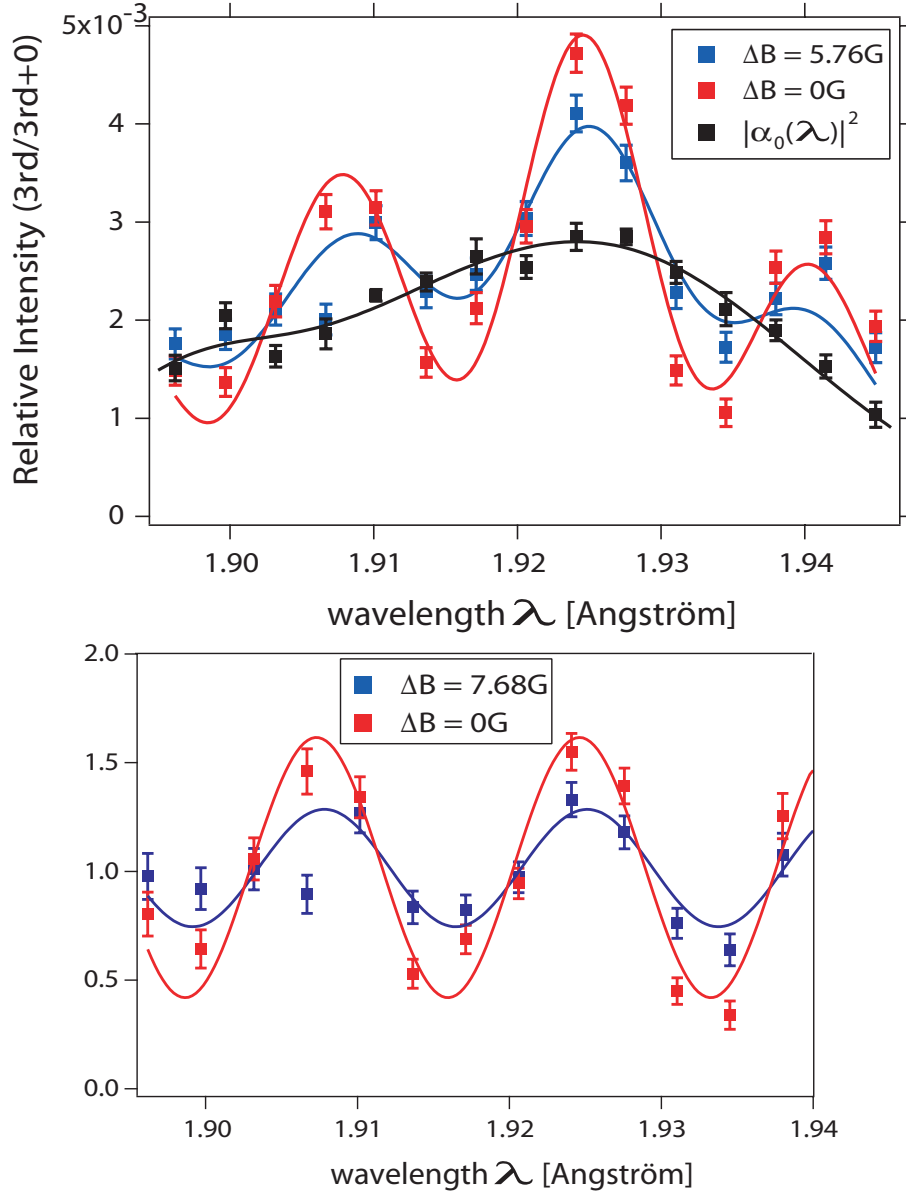


Figure 3.18: Interferogram in momentum space, wavelength distribution $|\alpha_0(\lambda)|^2$ of the empty interferometer and original on/off wavelength spectra for $\Delta_B = 7.86\text{G}$ for the 36mm Al Phase shifter causing a packet separation of $\Delta_x = 424\text{\AA}$ (upper diagram) and on/off-curves divided by $|\alpha_0(\lambda)|^2$ exhibiting a standard interferogram in cosine-shape (lower diagram).

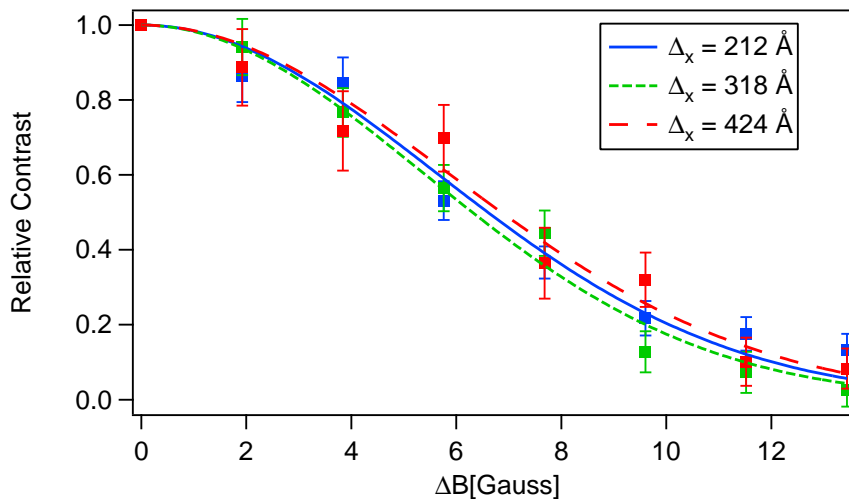


Figure 3.19: Decoherence behaviour for Schrödinger cat-like states with different separation width as function of the strength of the magnetic noise field (exponentially fitted)

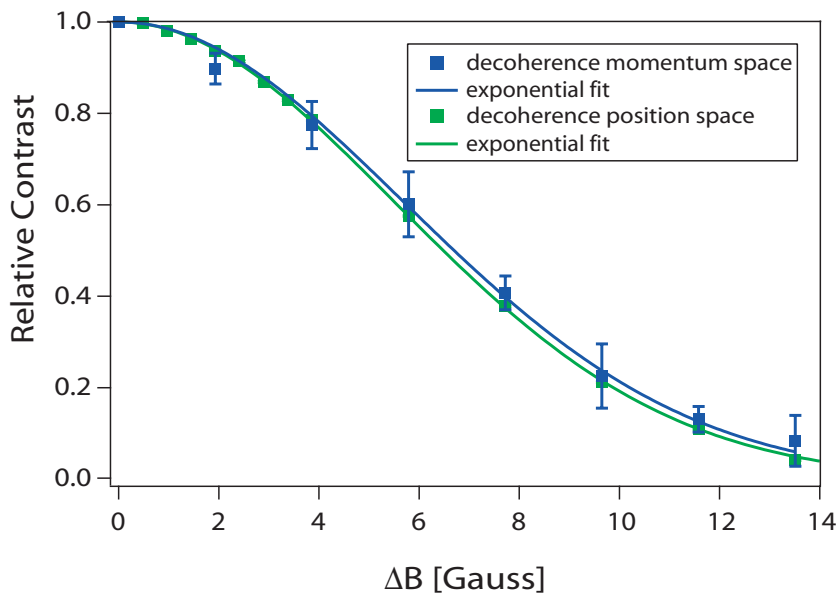


Figure 3.20: Decoherence behaviour for the standard interferometric setup and averaged behaviour of the damped modulations in momentum space plotted against noise strength ΔB (exponentially fitted).

3. MODELLING DECOHERENCE WITH MAGNETIC NOISE FIELDS

4

Finite mode number noise

4.1 Noise generation with random phases

Now, we want to approach the loss of contrast analytically by exploiting the results of chapter 2.1. There, we had an arbitrary oscillating magnetic field $B(t)$

$$B(t) = \sum_{i=1}^N B_i \cos(\omega_i t + \varphi_i) \quad (4.1)$$

restricted to a spatially finite region $0 \leq x < L$. After passing the field, the incoming plane wave is modified and the wave function ψ_{III} reads

$$\psi_{III}(x, t) = \sum_{\vec{n}} J_{n_1}(\beta_1) \cdot \dots \cdot J_{n_N}(\beta_N) e^{-i\vec{n}\vec{\eta}} e^{i\vec{k}_{\vec{n}}x} e^{-i\omega_{\vec{n}}t} \quad (4.2)$$

with

$$\vec{n} = (n_1, n_2, \dots, n_N), \quad \vec{\eta} = (\eta_1, \dots), \quad \vec{\omega} = (\omega_1, \dots) \quad (4.3)$$

$$\omega_{\vec{n}} = \omega_0 + \vec{n}\vec{\omega}, \quad \tilde{k}_{\vec{n}}^2 = k_0^2 - \frac{2m}{\hbar^2} \mu B_0 + \frac{2m}{\hbar} \vec{n}\vec{\omega} \quad (4.4)$$

$$\eta_i = \varphi_i + \frac{\omega_i T + \pi}{2}, \quad \beta_i = 2 \frac{\mu B_i}{\hbar \omega_i} \sin \frac{\omega_i T}{2} \quad (4.5)$$

The expression for the time dependent intensity $I_O(t)$ in the interferometric setup (see section 2.2) for unpolarized neutrons is given by

$$I_O^{unpol}(t) = \frac{1}{2} \left(1 + \cos \chi \cos \left(\sum_{i=1}^N \beta_i \sin(\omega_i t + \xi_i) \right) \right) \quad (4.6)$$

with

$$\xi_i = \varphi_i + \frac{\omega_i T + \pi}{2} - \frac{\omega_i}{v_0} x \quad (4.7)$$

4. FINITE MODE NUMBER NOISE

These formulas can be used for an arbitrary high, but still countable number of modes of the applied magnetic field, i.e. an arbitrary periodic field. An ideal noise signal consists of an infinite number of modes and is not periodic, but we will see that magnetic fields with about 200 or more modes whose phases are randomly distributed represent a good approximation for the ideal noise case as far as loss of contrast is concerned.

In chapter 2.2, we were interested in the time dependency of the intensity pattern from which we could deduce the transition probabilities for various energy transfers between the neutron and the magnetic field. Now, we do a time-independent intensity measurement, yielding an average intensity

$$\langle I_O \rangle = \frac{1}{N} \sum_{i=1}^N I_O(t_i) \quad (4.8)$$

over N neutrons detected at times t_i . Provided a sufficiently high neutron flux during the measurement time T_m we can rewrite the sum into an integral

$$\langle I_O \rangle = \frac{1}{T_m} \int_0^{T_m} I_O(t) dt \quad (4.9)$$

The period of the intensity is the same as the period of the magnetic field, given by the greatest common denominator $\omega_g = 2\pi/t_g$ of all occurring frequencies ω_i . If the measurement time is an integer multiple of t_g we can immediately rewrite

$$\langle I_O \rangle = \frac{1}{t_g} \int_0^{t_g} I_O(t) dt \quad (4.10)$$

If the measurement time is no integer multiple of t_g , but much larger than t_g ($T_m = n \cdot t_g + \Delta$, $n \gg 1$, $\Delta < t_g$, $\Delta/n \approx 0$), we can still estimate

$$\begin{aligned} \langle I_O \rangle &= \frac{1}{n \cdot t_g + \Delta} \left(\int_0^{n \cdot t_g} I_O dt + \int_{n \cdot t_g}^{n \cdot t_g + \Delta} I_O dt \right) \\ &\simeq \frac{1}{n \cdot t_g} \left(\int_0^{n \cdot t_g} I_O dt + \Delta \cdot \text{Max}(I_O) \right) \\ &\simeq \frac{1}{n \cdot t_g} \int_0^{n \cdot t_g} I_O dt = \frac{1}{t_g} \int_0^{t_g} I_O(t) dt \end{aligned} \quad (4.11)$$

leading to the same result. In the most simple case where the number of modes

4.1 Noise generation with random phases

$N = 1$ and $t_g = 2\pi/\omega_1$, we can then write

$$\begin{aligned}
 \langle I_O \rangle &= \frac{1}{t_g} \int_0^{t_g} \frac{1}{2} (1 + \cos \chi \cos (\beta_1 \sin(\omega_1 t + \xi_i))) dt \\
 &= \frac{1}{2} \left(1 + \cos \chi \frac{1}{t_g} \int_0^{t_g} \cos (\beta_1 \sin(\omega_1 t + \xi_i)) dt \right) \\
 &= \frac{1}{2} \left(1 + \cos \chi \frac{1}{2\pi} \int_0^{2\pi} \cos (\beta_1 \sin t) dt \right) \\
 &= \frac{1}{2} (1 + J_0(\beta_1) \cos \chi)
 \end{aligned} \tag{4.12}$$

showing that the measured contrast is given by the Bessel function J_0 if a sinusoidal field is applied. In fig.4.1, experimental results for various frequencies are shown. In case of more than one mode, the integral (eq.4.10) is not solvable at

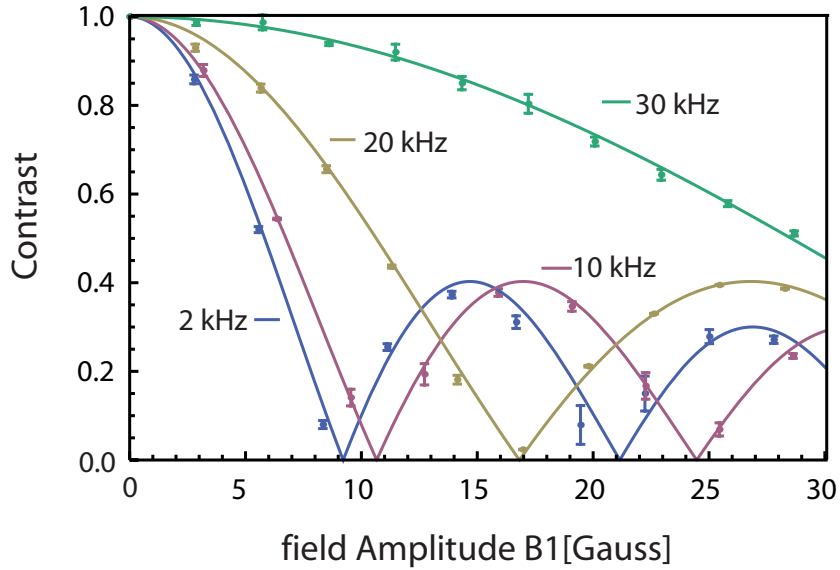


Figure 4.1: Measured contrast plotted against the amplitude B_1 of the applied single mode field $B(t) = B_1 \cos(\omega_1 t + \varphi_1)$ for various frequencies $\omega_1 = 2\pi \cdot 2\text{kHz}$, $2\pi \cdot 10\text{kHz}$, $2\pi \cdot 20\text{kHz}$ and $2\pi \cdot 30\text{kHz}$. The measured values agree well with the theory curve given by the Bessel function $J_0(\beta_1)$.

first sight, but we can use a former result to simplify things. As already mentioned, the intensity $I_O(t)$ has the same period as the magnetic field and can therefore be composed into a discrete Fourier series.

$$I_O(t) = \sum_{m=-\infty}^{+\infty} c_m e^{im\omega_g t} \tag{4.13}$$

4. FINITE MODE NUMBER NOISE

Over a full period, the oscillating parts vanish

$$\frac{1}{t_g} \int_0^{t_g} e^{im\omega_g t} dt = \delta_{m,0}$$

and we get for the measured time-averaged intensity

$$\langle I_O \rangle = \frac{1}{t_g} \int_0^{t_g} I_O(t) dt = \frac{1}{t_g} \int_0^{t_g} \sum_{m=-\infty}^{+\infty} c_m e^{im\omega_g t} dt = c_0 \quad (4.14)$$

The explicit form of all Fourier coefficients has been already determined in sec.2.2 (see eqs.2.82 and 2.83 for polarized neutrons and eqs.2.101 and 2.102 for unpolarized neutrons). We now need the coefficient c_0 for unpolarized neutrons that reads

$$c_0^{unpol} = \frac{1}{2} + \frac{1}{2} \cos \chi \sum_{\substack{\vec{n}; \vec{n}\vec{\omega}=0 \\ \sum_i n_i \text{ even}}} J_{n_1}(\beta_1) \cdot \dots \cdot J_{n_N}(\beta_N) e^{i\vec{n}\vec{\xi}} \quad (4.15)$$

revealing that the contrast is given by the modulus of the restricted sum. In case of $N = 1$, only $J_0(\beta_1)$ remains. For two modes $N = 2$, we have already investigated the Fourier coefficient c_0 for the frequencies $\omega_1 = 2\pi \cdot 2\text{kHz}$ and $\omega_2 = 2\pi \cdot 3\text{kHz}$ (eq.2.107). In general, the expression for the contrast C can be written for two frequencies ω_1 and ω_2 with $\omega_1/\omega_2 = p/q$, where p, q are coprime and $p + q$ is even

$$C = \sum_{n_1=0}^{+\infty} (2 - \delta_{n_1,0}) J_{qn_1}(\beta_1) J_{pn_1}(\beta_2) \cos(n_1(q\xi_1 - p\xi_2)) \quad (4.16)$$

$$(4.17)$$

or if $p + q$ is odd

$$C = \sum_{n_1=0}^{+\infty} (2 - \delta_{n_1,0}) J_{2qn_1}(\beta_1) J_{2pn_1}(\beta_2) \cos(2n_1(q\xi_1 - p\xi_2)) \quad (4.18)$$

$$(4.19)$$

In fig.4.2, we show a comparison between the results of the numeric integration (eq.4.10) and the explicit formula for the Fourier coefficient (eq.4.18) for a two mode field with frequencies $\omega_1 = 2\pi \cdot 10\text{kHz}$ and $\omega_2 = 2\pi \cdot 20\text{kHz}$, equal amplitudes $B_1 = B_2$ and phases $\varphi_1 = 0.42$ and $\varphi_2 = 2.26$. In the typical experimental field strength range of $B_1 \approx 0 - 50\text{Gauss}$, it is sufficient to take only the first three terms of the sum into account to achieve a good agreement.

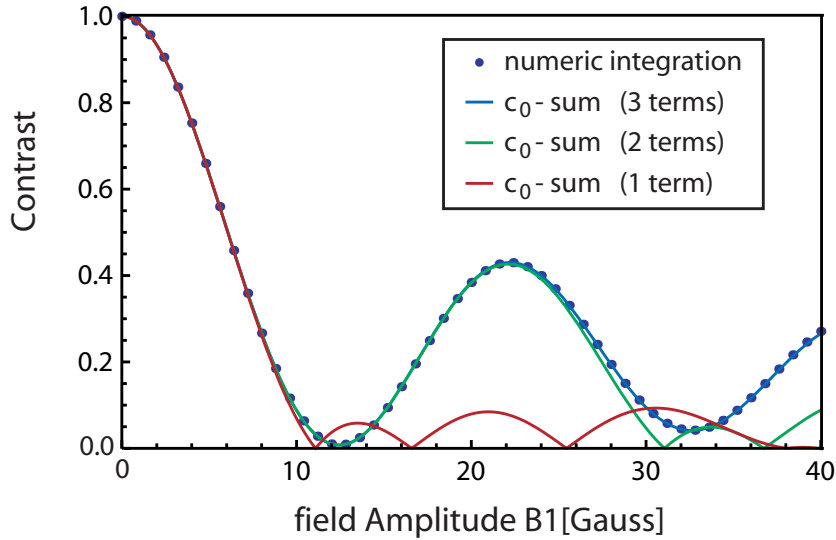


Figure 4.2: Interferometer contrast plotted against the amplitude B_1 when a two-mode field $B(t) = B_1 \cos(\omega_1 t + 0.42) + B_1 \cos(\omega_2 t + 2.26)$ with equally high amplitudes and frequencies $\omega_1 = 2\pi \cdot 10\text{kHz}$ and $\omega_2 = 2\pi \cdot 20\text{kHz}$ is applied. The results of the numeric integration (blue points) of the time-dependent intensity are compared to the sum obtained from the Fourier coefficient. After regarding the first three summands the results already coincide.

If the number of modes is further increased the evaluation of the conditions on the summation becomes more and more difficult. A closed representation becomes impossible and symbolic programming languages have to be used to get all combinations that fulfill $\sum_i n_i \omega_i = 0$. For $N = 5$, these calculations are still possible in a reasonable amount of time (see result for c_0 in fig.2.44 of chapter 2.3.4), but the computational effort for solving the numeric integration has already become lower. Therefore, we will from now on use the numeric integration, where the contrast is determined with 6-digits precision.

To compare the results for an increased number of field modes N , the amplitudes of all modes are chosen to be equal and normalized with \sqrt{N} ensuring constant signal power. The frequencies of the N modes are equidistantly distributed from $20/N$ kHz - 20kHz with step width $20/N$ kHz, e.g. for 5 modes, frequencies are 4, 8, 12, 16, and 20kHz. When the number of modes is increased, one can see that the oscillating behaviour of the contrast is washed out, i.e. recovery of contrast is suppressed due to the randomly distributed phases of the modes. In fig.4.3, this behaviour is illustrated for 2-20 modes.

If the number of modes exceeds 50, the effect is even more drastic (see fig.4.4). In addition to the vanishing contrast oscillations, the exponential decay of the

4. FINITE MODE NUMBER NOISE

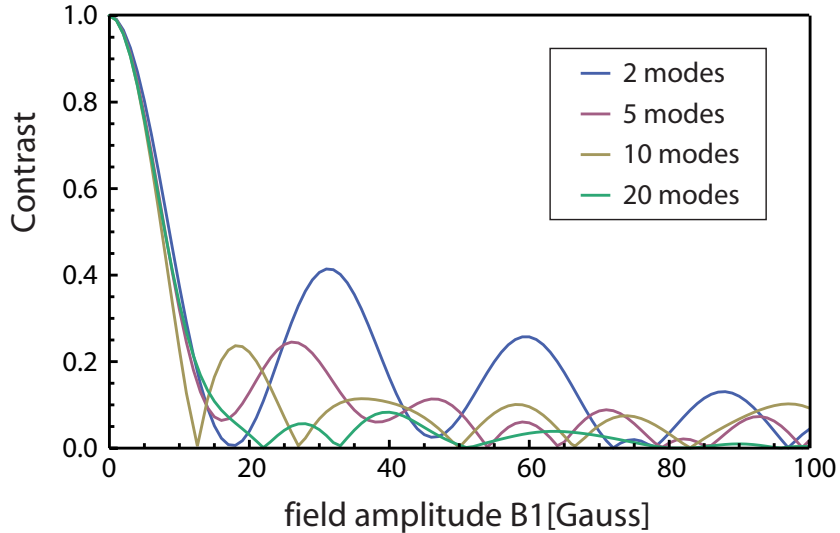


Figure 4.3: Interferometer contrast plotted against the amplitude B_1 when magnetic fields with increasing mode numbers are applied. The phases of the modes are randomly distributed in $[0, 2\pi)$. Contrast recovery vanishes for higher mode numbers.

contrast with increasing field strength becomes apparent.

If the number of modes is further increased, results for the same mode number obtained from magnetic field signals with varied relative phases differ in the same amount from each other as results obtained from different mode numbers. Therefore, one has to perform the simulation for a certain mode number repeatedly with different relative phases in order to get a mean contrast curve. The mean contrasts for different mode numbers can then be compared. As shown in fig.4.5, the mean contrast curves become practically indistinguishable. The damping factor obtained from an exponential fit is the same for the different mode numbers. That means that, as far as loss of contrast is concerned, the behaviour of the ideal noise with an infinite number of modes is practically the same as in the case of a magnetic field consisting of several hundred modes with randomly distributed relative phases. Increasing the number of frequencies only causes a stronger suppression of the contrast recovery for high field strengths.

Equipped with this knowledge, we can now investigate the influence of the frequency bandwidth of the noise on the damping factor by just determining it from the 200 modes signal. We are especially interested in damping factors for noise fields with frequency bandwidths $\Delta f = 0 - f_{\text{upper}}$ for upper frequencies f_{upper} ranging from 1 to 100 kHz. In this range, the numerically obtained curves can be compared with the measured contrast (see fig.3.6 in sec.3). In the experiment,

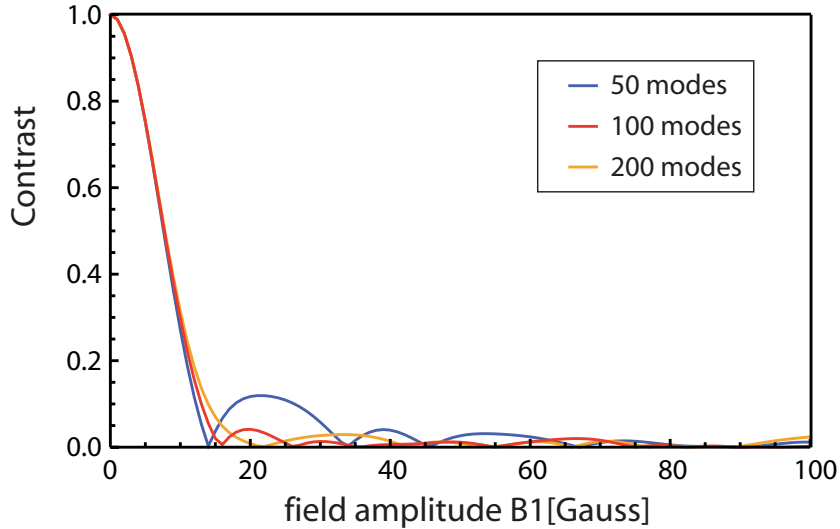


Figure 4.4: Interferometer contrast plotted against the amplitude B_1 when magnetic fields with 50, 100 and 200 modes are applied whose phases are randomly distributed in $[0, 2\pi)$. Contrast recovery vanishes totally and the exponential decay of contrast becomes visible.

the accessible parameter is the width of the Gaussian noise and we therefore have to find the width ΔB corresponding to a certain field amplitude B_1 of the 200 mode signal. For this instance, we plot the histogram of the magnetic field signal for $B_1 = 1\text{Gauss}$ and determine its width (see fig.4.6).

The damping factor k is then determined from the numerically calculated contrast curves plotted against increasing field width by using an exponential fit function given by

$$\text{fit}(k) = e^{-\frac{1}{2}k\left(\frac{\mu_N}{\hbar} \frac{L}{v} \Delta B\right)^2} \quad (4.20)$$

The proportionality factors are chosen such that a damping factor of $k = 1$ indicates the region where the quasistatic approximation is valid (see eq.3.52). To obtain the damping factor, we generate the 200 mode signal 100 times with different relative phases, determine the width for each signal and fit the numerically computed contrasts curves with the exponential fit function $\text{fit}(k)$. From the 100 k -values, mean value and standard deviation are calculated. In fig.4.7, the results of the simulation are compared to the measured quantities showing a satisfying agreement.

In the numerical simulation, the upper frequency can be further increased. As expected, the damping factor tends towards 0, because modes belonging to higher frequencies do not contribute to the loss of contrast. Their effect is averaged out, the phase shift they provoke is zero. In the semi-classical phaseshift picture, this

4. FINITE MODE NUMBER NOISE

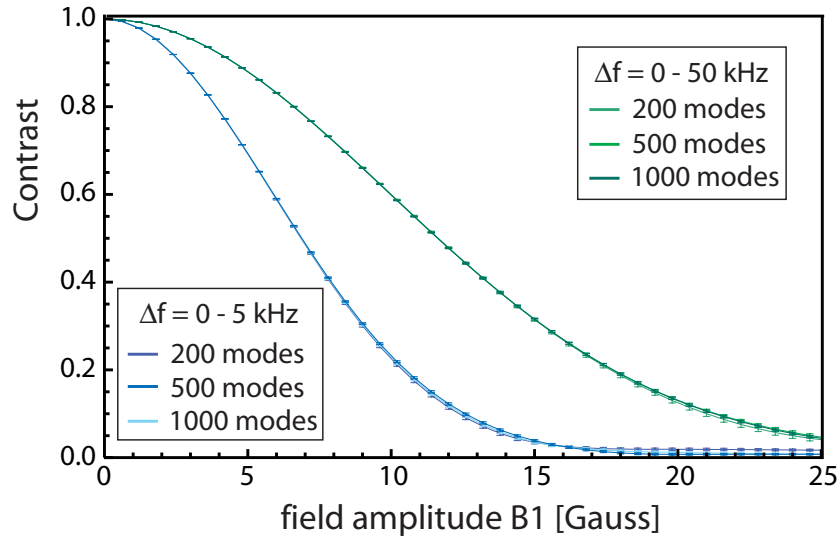


Figure 4.5: Interferometer contrast plotted against the amplitude B_1 when magnetic fields with 200, 500 and 1000 modes are applied whose phases are randomly distributed and whose frequencies lie in the range Δf . The contrast curve represents the mean value obtained from 25 simulations for each mode number. The error bars indicate the standard deviation of the mean value. The plot shows that using more than 200 modes in the simulation has no effect on the loss of contrast.

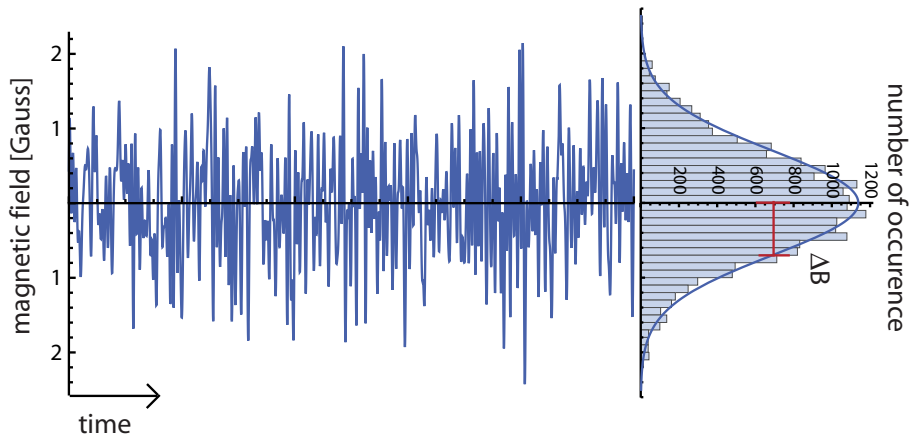


Figure 4.6: By sampling equidistant points from the magnetic field signal $B(t)$, we can construct its corresponding histogram from which the width ΔB can be determined.

can be seen from the integral over the time-off-flight (eq.2.164). In fig.4.8, the results of the simulation are shown.

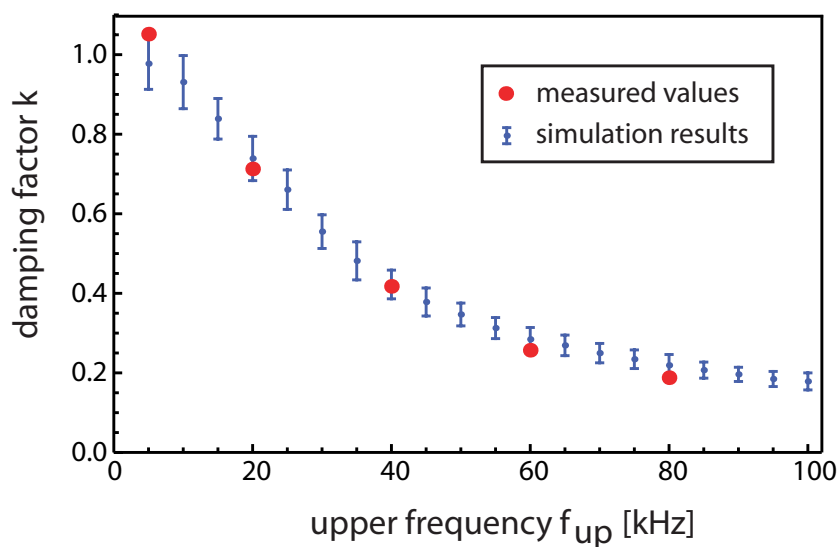


Figure 4.7: Damping factors k for magnetic noise fields with a frequency bandwidth from 0 to an upper frequency f_{up} . The experimentally determined values (red points) are compared to the results of a hundredfold repeated simulation relying on a magnetic signal consisting of 200 modes with randomly distributed phases. Error bars indicate the standard deviation of the 100 k -values.

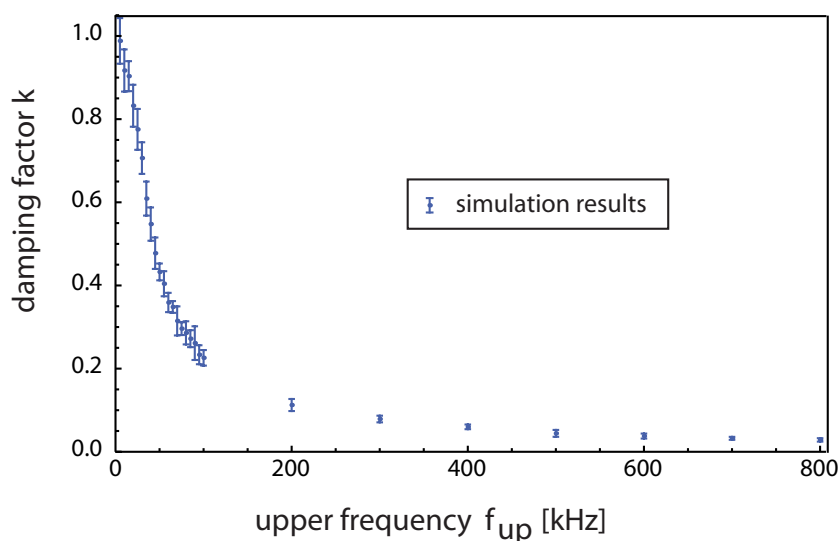


Figure 4.8: Damping factors k for magnetic noise fields with a frequency bandwidth from 0 to f_{up} . For increasing upper frequency, the damping factor vanishes, i.e contrast reduction also vanishes.

4. FINITE MODE NUMBER NOISE

Unfortunately, no simple analytic relation between the damping factor k and the upper frequency f_{up} becomes apparent.

4.2 Alternative noise generation

Till now, we have modelled the noise by considering equidistantly distributed frequencies in the region of interest whose phases are randomly distributed. In this way, we could immediately find the periodicity of the field from the lowest occurring frequency and use the integration formula (eq.4.9) instead of the sum (eq.4.8) to calculate the intensity.

One could argue that not only the phases, but also the frequencies should be randomly distributed, in order to simulate the ideal Gaussian white noise. The statistics of the amplitude distribution are really improved with this method, but we will show in this chapter that the influence on the loss of contrast is marginal.

If the frequencies are randomly distributed, the integration method fails, because the period of the signal becomes too long. Therefore, we have to rely on the summation method. Again, we generate the signal repeatedly and determine the mean value and standard deviation for the damping factor k for increasing frequency bandwidth Δf . In fig.4.9, the former result with random distributed phases only is compared to the new signal. It can be seen, that the mean values of one method lie within the standard deviations of the other method and vice versa. The experimentally measured values can also be reproduced by both approaches.

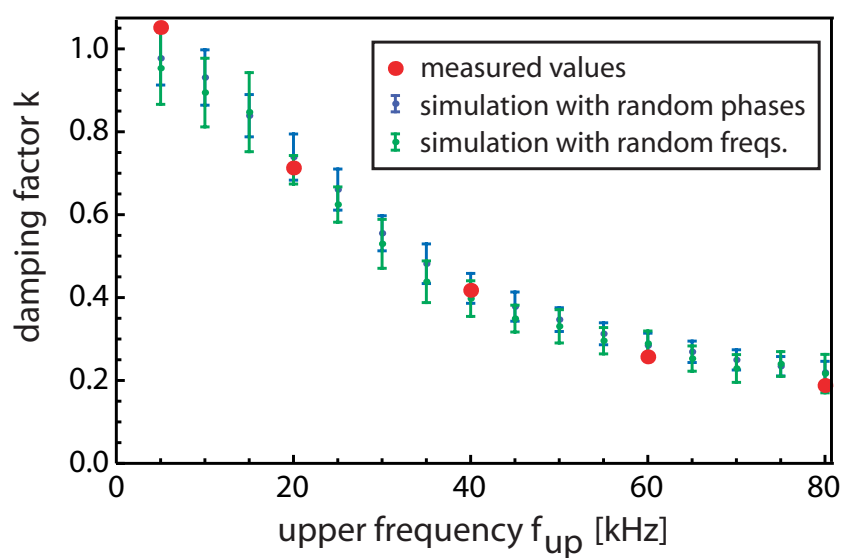


Figure 4.9: Comparison of the contrast reduction for differently generated noise signals with frequency bandwidth $\Delta f = 0 - f_{up}$. Both methods reproduce the experimentally measured values and lie within each others errors bars.

4. FINITE MODE NUMBER NOISE

5

Conclusion and Outlook

The main focus of this work was the theoretical and experimental investigation of the action of spatially bounded, time-dependent magnetic fields in the neutron interferometer. Since the direction of the magnetic field is fixed, all observations concern the dynamical phase, the geometric phase remains unchanged.

We started with the simple case of a sinusoidally varying field. For thermal neutrons and field strengths of maximally 100 Gauss, reflections at the magnetic potential can be neglected and the corresponding Schrödinger equation containing the field as a classical quantity was solved analytically. An incoming plane wave is split up in a superposition of plane waves whose energies are given by the initial energy plus integer multiples of the field's frequency ω . The transition amplitude for an energy exchange of $n\hbar\omega$ is given by the Bessel function J_n . The calculation was then generalized to an arbitrary periodic field. Energy exchange from all modes of the field occurs and leads to products of Bessel functions for the transition probabilities. If such a periodic field is applied in one arm of the neutron interferometer the transition amplitudes can be extracted from the Fourier analysis of the time dependent interference pattern. Results for magnetic signals with up to five modes have been depicted and show good agreement with the calculation.

We also presented an alternative, semiclassical approach relying on the eikonal approximation for path integrals. The modulus of the transition amplitudes is equal to the solution obtained from the Schrödinger equation, only their phase factors are different. Thus, it would be a task for future experiments to focus on the phase which was till now only treated as fit parameter.

By performing field quantization, a fully quantum mechanical treatment of neutron and magnetic field could also be achieved. In this model, the energy transfer is explained as a two-fold multi-photon exchange process and the entanglement between neutron and field caused by their interaction becomes visible. For high photon number coherent states, the results of the classical calculations

5. CONCLUSION AND OUTLOOK

can be reproduced. To obtain quantum effects that can not be explained with the classical field, the model could be adapted to systems with a stronger particle-field coupling where low mean photon numbers already have a considerable influence, e.g. atoms with higher magnetic moments, or charged particles in spatially bounded electric fields. Obviously, the experimental realization of the field is then a challenging task as well.

If the number of modes is increased the resolution of the energy exchanges becomes more and more difficult. Provided that the phases of the modes are randomly distributed, we approach the noise regime where the coherence of the neutron beam is totally destroyed. The contrast of the interferometer vanishes and can be interpreted as realization of a dephasing channel for the path qubit in the framework of decoherence theory. In order to see the connection, the main statements of decoherence theory with focus on their application to neutron interferometry were revisited. The loss of coherence was investigated for varying parameters:

At first, the exponential loss of contrast was verified for quasi-static magnetic noise fields. Then, the frequency bandwidth of the noise signal was extended leading to a weaker decay of contrast.

If noise fields are applied in both interferometer arms the correlation of these two noise signals determines the contrast. For uncorrelated noise sources, the dephasing process is enforced. For two Gaussian white noise signals with the same frequency bandwidth, the decrease of contrast depends on the sum of their variances. On the other hand, applying synchronized identical noise signals leads to full recovery of the contrast. By inserting an additional time delay between the two sources the autocorrelation function of the signal is revealed.

Not only the noise signal, but also the neutron wave function was modified and exposed to noise. By inserting thick aluminum blocks, the wave packets are shifted beyond their spatial coherence length. The interference of these Schrödinger cat-like states is exhibited in k-space through a modulated momentum distribution. The preparation of the Schrödinger cat-like states becomes more difficult with increasing spatial separation but, within measurement accuracy, the noise induced loss of contrast is independent of the spatial separation and comparable to the decoherence behaviour in the standard interferometric setup.



5. CONCLUSION AND OUTLOOK

Appendix A

Error propagation for Discrete Fourier Transformations

In sec.2.2, the discrete Fourier transformation (DFT) method is used to determine the modulus of the Fourier components of the time dependent intensity pattern that are related to the transition probabilities of energy exchanges between a neutron and an oscillating magnetic field. Since we can not directly measure the Fourier components the question arises, how their errors can be calculated from the errors of the measured intensity. Therefore, we have to investigate the DFT in more detail.

Consider a real-valued function that is periodic in time with period T . If it fullfills the Dirichlet conditions [Chu2008], it can be expanded in its Fourier series

$$x(t) = x(t + T) = \sum_{n=-\infty}^{n=+\infty} X_n e^{i2\pi \frac{n}{T}t} \quad (\text{A.1})$$

containing the fundamental frequency $f = 1/T$ and its harmonics $n \cdot 1/T$. If only frequencies up to $(N - 1)/2 \cdot 1/T$ are contained in the signal, a sample of N equidistant points $\{x_1, x_2, \dots, x_N\}$ over the full period suffices to determine the Fourier components exactly (Shannon-Nyquist sampling theorem, see [Chu2008]). The k -th component belonging to the frequency $k \cdot 1/T$ is given by the discrete Fourier transformation (DFT)

$$X_k = \frac{1}{\sqrt{N}} \sum_{n=0}^{N-1} x_n e^{-i\frac{2\pi}{N}k \cdot n} \quad (\text{A.2})$$

Note that the index k runs from 0 to $N - 1$ but due to the real x_i 's the relation $X_k = X_{N-k}^*$ holds and we only get independent coefficients from $k = 0$ to $(N - 1)/2$.

A. ERROR PROPAGATION FOR DISCRETE FOURIER TRANSFORMATIONS

If the distribution of the sample points is known, the most accurate way to determine the uncertainty in the Fourier components relies on simulated repetition of the experiment. Therefore, one generates a large number M of sequences $\{x_1, \dots, x_N\}$ according to their underlying distribution. The Fourier components of each of these sequences can be determined by eq.A.2, resulting in M values for each component whose distribution can then be investigated.

In our case, the originally measured values x_n are the number of detected neutrons. These counts are Poissonian distributed, i.e. the standard deviation is given by the square of the counts. Note that, for high count rates, the Poissonian distribution of a number of counts N nearly equals a normal distribution with mean value N and standard deviation \sqrt{N} . We take the fit values obtained from the measurement as starting values and generate 10000 samples numerically. In order to get intensities instead of count rates, we also subtract the underground u and divide all samples by the contrast c that we have obtained from the fit. We assume the values of u and c to have neglectable errors. The intensity samples \tilde{x}_n obtained from the count rate samples x_n are thus given by

$$\tilde{x}_n = \frac{x_n - u}{c}, \quad \Delta \tilde{x}_n^2 = \frac{\Delta x_n^2}{c^2} = \frac{x_n}{c^2}, \quad \tilde{x}_n \sim \mathcal{N}(\mu, \sigma) = \mathcal{N}\left(\tilde{x}_n, \frac{\sqrt{x_n}}{c}\right) \quad (\text{A.3})$$

where $\sim \mathcal{N}(\mu, \sigma)$ denotes a normal distribution with mean value μ and standard deviation σ .

In fig.A.1, we show the starting sample and its standard deviation, the fit curve and two generated sequences, indicated by the red and the green points respectively.

From the generated samples, we get the distribution of each Fourier component. As far as the transition probabilities are concerned, we are interested in the modulus of the Fourier components. For the even components we obtain approximately normal distributions whereas the vanishing odd components become Rayleigh-distributed. That stems from the fact that both real and imaginary part of the odd components are identically and independently normal distributed around zero with comparable standard deviations. In fig.A.2 and fig.A.3 the histograms of the modulus of the Fourier coefficients X_2 and X_3 are shown to illustrate both the odd and the even case.

Simulating the experiment numerically allows the determination of the exact form of the distribution of the Fourier components. The method is very elaborate and contains the maximal information. But on the other hand, it becomes apparent that distribution of the non-vanishing Fourier components is in good approximation Gaussian. To characterize a Gaussian distribution, only its mean value and standard deviation are necessary. We will now try to calculate the standard deviations of the Fourier components by using the error propagation law. The error propagation law is valid if the originally measured quantities are Gaus-

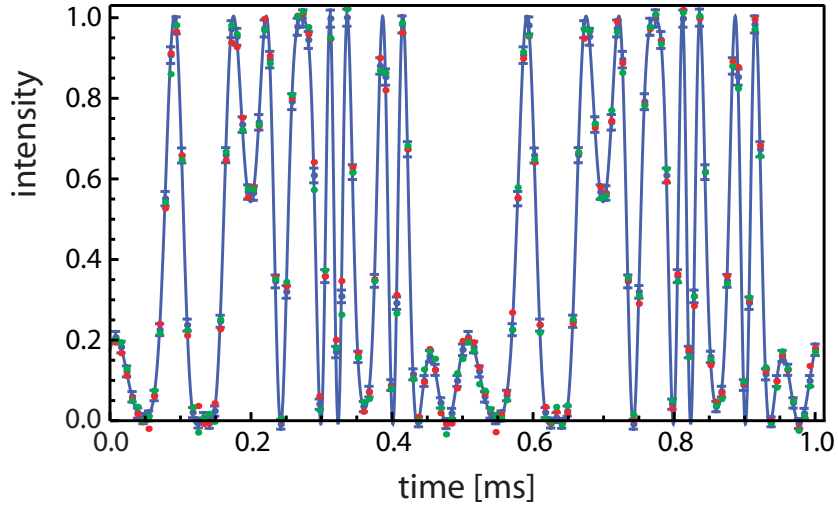


Figure A.1: Exemplary time dependent intensity pattern. The blue curve represents the fit obtained from the actual measurement. Its values (blue points) and their standard deviations (blue error bars) serve as starting point for the numerically simulated sequences (e.g. red and green points).

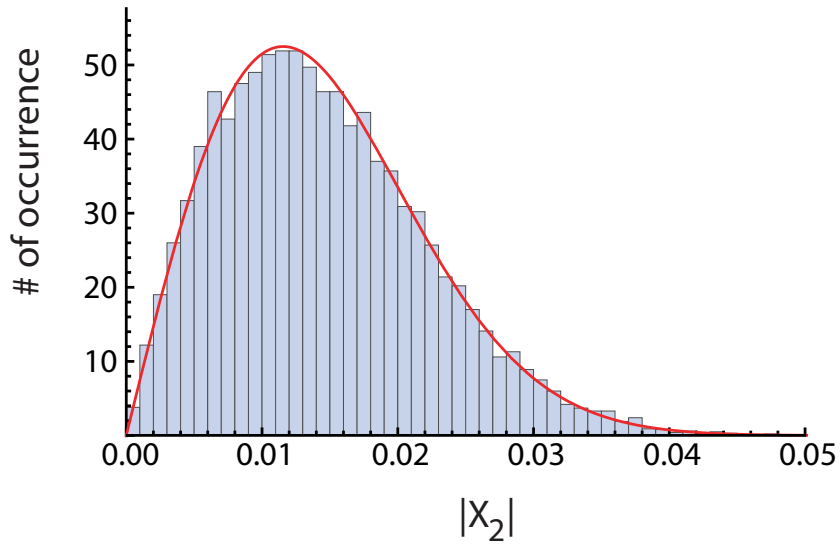


Figure A.2: Histogram of the modulus of the Fourier component X_2 . The red curve represents a Rayleigh distribution with parameter $\sigma = \langle |X_2| \rangle / \sqrt{\pi/2}$ where $\langle |X_2| \rangle$ indicates the mean value of the modulus of all X_2 .

sian distributed and if their standard deviations are so small, that the relation

A. ERROR PROPAGATION FOR DISCRETE FOURIER TRANSFORMATIONS

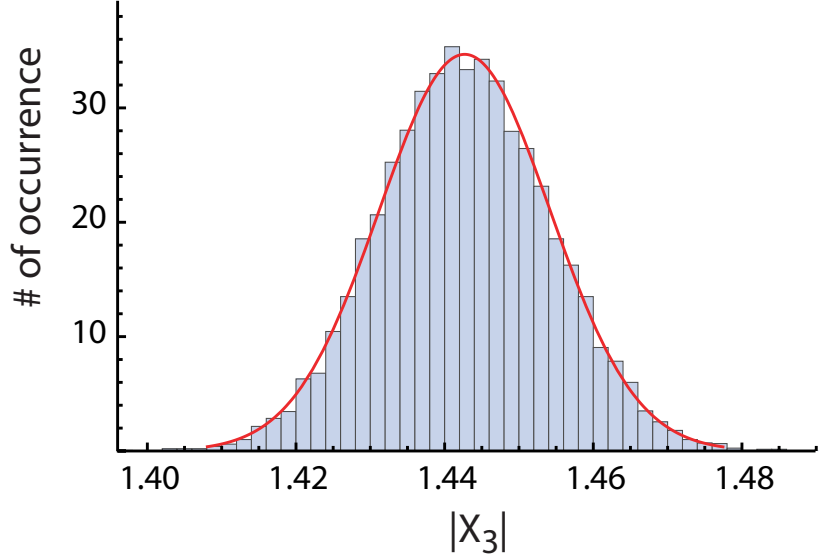


Figure A.3: Histogram of the modulus of the Fourier component X_3 . The red curve indicates that the modulus is normal distributed. Its mean value is the mean value $\langle |X_3| \rangle$ of the modulus of all X_3 and the standard deviation is their usual standard deviation $\sqrt{\langle |X_3| - \langle |X_3| \rangle \rangle^2}$.

between originally measured quantities and derived quantities can be considered to be linear in the observed range. The derived quantity y is then also Gaussian distributed with a standard deviation given by Δy

$$y = f(x_1, x_2, \dots, x_N) \implies \Delta y = \sqrt{\sum_{i=1}^N \left(\frac{\partial f}{\partial x_i} \right)^2 \Delta x_i^2} \quad (\text{A.4})$$

Since eq.A.4 is only valid for real numbers we at first have to investigate real and imaginary part of the Fourier components X_k separately

$$X_k = Y_k + iZ_k \quad (\text{A.5})$$

$$Y_k = \frac{1}{\sqrt{N}} \sum_{n=0}^{N-1} \tilde{x}_n \cos\left(\frac{2\pi}{N}k \cdot n\right) \quad (\text{A.6})$$

$$Z_k = -\frac{1}{\sqrt{N}} \sum_{n=0}^{N-1} \tilde{x}_n \sin\left(\frac{2\pi}{N}k \cdot n\right) \quad (\text{A.7})$$

The relation between the Gaussian-distributed \tilde{x}_n and the Y_k 's and Z_k 's is linear, whence follows that the Y_k 's and Z_k 's are also Gaussian-distributed with standard

deviations ΔY_k and ΔZ_k given by

$$\Delta Y_k^2 = \frac{1}{N} \sum_{n=0}^{N-1} \Delta \tilde{x}_n^2 \cos^2\left(\frac{2\pi}{N}k \cdot n\right) = \frac{1}{N} \sum_{n=0}^{N-1} \frac{x_n}{c^2} \cos^2\left(\frac{2\pi}{N}k \cdot n\right) \quad (\text{A.8})$$

$$\Delta Z_k^2 = \frac{1}{N} \sum_{n=0}^{N-1} \Delta \tilde{x}_n^2 \sin^2\left(\frac{2\pi}{N}k \cdot n\right) = \frac{1}{N} \sum_{n=0}^{N-1} \frac{x_n}{c^2} \sin^2\left(\frac{2\pi}{N}k \cdot n\right) \quad (\text{A.9})$$

To determine the error of the modulus of the Fourier components we have to apply the error propagation law once again, but we will now include the covariance term as well since correlations between real and imaginary part can not be excluded a priori.

$$|X_k| = \sqrt{Y_k^2 + Z_k^2} \quad (\text{A.10})$$

$$\begin{aligned} \Delta |X_k|^2 &= \left(\frac{\partial |X_k|}{\partial Y_k}\right)^2 \Delta Y_k^2 + \left(\frac{\partial |X_k|}{\partial Z_k}\right)^2 \Delta Z_k^2 + \\ &\quad 2 \frac{\partial |X_k|}{\partial Y_k} \frac{\partial |X_k|}{\partial Z_k} \text{cov}(Y_k, Z_k) \end{aligned} \quad (\text{A.11})$$

Here, the relation between $|X_k|$ and Y_k and Z_k is nonlinear and thus distortions from the normal-distributed shape are to be expected. For the calculation of the covariance term, the independence of the individual count rates is used, i.e. $\text{cov}(x_n, x_m) = x_n \delta_{nm}$.

In the latter, we will compare the standard deviations obtained from the error propagation law with the results from the repeatedly simulated experiment, but before we want to introduce a simplified expression for the standard deviation. We assume, that all \tilde{x}_n have the same error given by the square root of the mean value \bar{x} of the x_n divided by contrast c . Starting from eq.A.8 we get for the simplified error

$$\Delta Y_{k, \text{simp}}^2 = \frac{1}{N} \sum_{n=0}^{N-1} \frac{\bar{x}}{c^2} \cos^2\left(\frac{2\pi}{N}k \cdot n\right) \quad (\text{A.12})$$

$$\Delta Y_{k, \text{simp}}^2 = \frac{\bar{x}}{Nc^2} \sum_{n=0}^{N-1} \frac{1}{2} (1 + \cos(2\frac{2\pi}{N}k \cdot n)) \quad (\text{A.13})$$

$$\Delta Y_{k, \text{simp}}^2 = \begin{cases} \frac{\bar{x}}{c^2} & \text{if } k = 0 \text{ or } N/2 \\ \frac{1}{2} \frac{\bar{x}}{c^2} & \text{else} \end{cases} \quad (\text{A.14})$$

For the imaginary part, we get

$$\Delta Z_{k, \text{simp}}^2 = \begin{cases} 0 & \text{if } k = 0 \text{ or } N/2 \\ \frac{1}{2} \frac{\bar{x}}{c^2} & \text{else} \end{cases} \quad (\text{A.15})$$

A. ERROR PROPAGATION FOR DISCRETE FOURIER TRANSFORMATIONS

and finally for the modulus when neglecting the covariance term

$$\Delta|X_k|^2, \text{ simp} = \begin{cases} \frac{\bar{x}}{c^2} & \text{if } k = 0 \text{ or } N/2 \\ \frac{1}{2} \frac{\bar{x}}{c^2} & \text{else} \end{cases} \quad (\text{A.16})$$

Now, we can compare the differently obtained errors in our example where we restrict ourselves to the non-vanishing first 32 even Fourier coefficients. As one can see from fig.A.4, the standard deviations calculated from the numerically generated "measured" points agree well with the results from the error propagation law. The covariance term does not lead to an improvement. For a reasonable estimation for the error bars of the Fourier components it even suffices to only use the simplified error propagation formula.

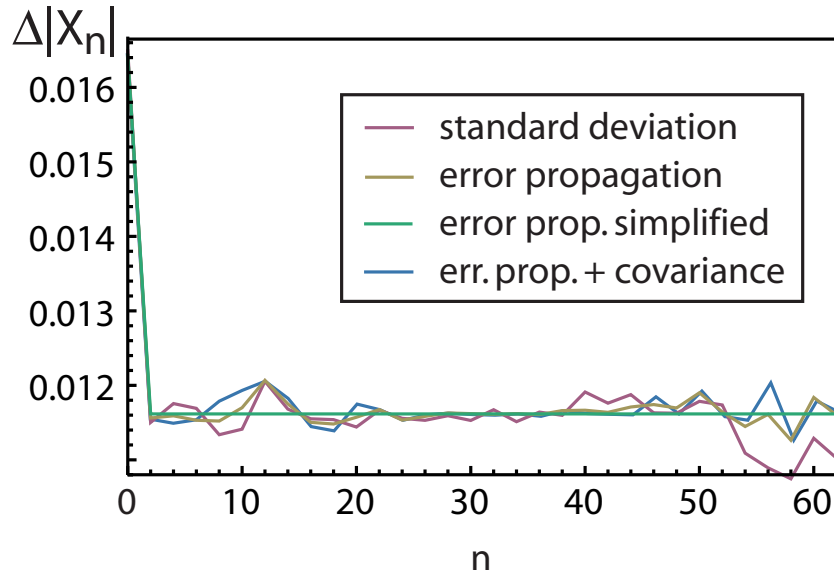


Figure A.4: The errors for the (even) Fourier components obtained from the numerical simulation of the experiment and from various formulations of the error propagation law.

For various intensity patterns (1-, 2- and 5-mode magnetic field, different amplitudes), similar results have been found. Thus, we used the simplified error propagation law to estimate the error of the Fourier components in the experiments of sec.2.2.

Bibliography

- [ABR1981] B. Alefeld, G. Badurek, and H. Rauch, *Observation of the neutron magnetic resonance energy shift*, Z. Phys. B **41** (1981), 231–235. [2](#), [5](#)
- [ANVA⁺1999] Markus Arndt, Olaf Nairz, Julian Voss-Andreae, Claudia Keller, Gerbrand van der Zouw, and Anton Zeilinger, *Wave-particle duality of C60 molecules*, Nature **401** (1999), 680–682. [1](#)
- [AS1964] M. Abramowitz and I. A. Stegun, *Handbook of mathematical functions*, Dover Publications, New York, 1964. [11](#)
- [Bar2005] Matthias Baron, *Messung von Quantenzuständen im Neutroneninterferometer*, Ph.D. thesis, TU Wien, Vienna, March 2005. [84](#)
- [BBKH2001] S. Basu, S. Bandyopadhyay, G. Kar, and D. Home, *Bell’s inequality for a single spin-1/2 particle and quantum contextuality*, Physics Letters A **279** (2001), 281–286. [77](#)
- [Ber1997] P. Berman (ed.), *Atom interferometry*, Academic Press, New York, 1997. [1](#)
- [BH1965] U. Bonse and M. Hart, *An X-ray interferometer*, Appl. Phys. Lett. **6** (1965), 155. [2](#)
- [BKS⁺2009] H. Bartosik, J. Klepp, C. Schmitzer, S. Sponar, A. Cabello, H. Rauch, and Y. Hasegawa, *Experimental test of quantum contextuality in neutron interferometry*, Phys. Rev. Lett. **103** (2009), 040403. [78](#)
- [Boh1925] Harald Bohr, *Zur Theorie der fastperiodischen Funktionen I*, Acta Math. **45** (1925), 29-127. [12](#)
- [BP2002] H.-P. Breuer and F. Petruccione, *The theory of open quantum systems*, Oxford University Press, Oxford, 2002. [2](#), [77](#), [90](#)

BIBLIOGRAPHY

- [BRS2003] Matthias Baron, Helmut Rauch, and Martin Suda, *First attempt of neutron quantum state reconstruction*, Journal of Optics B: Quantum and Semiclassical Optics **5** (2003), S241–S244. [84](#), [91](#)
- [CHL⁺1995] Michael S. Chapman, Troy D. Hammond, Alan Lenef, Jörg Schmiedmayer, Richard A. Rubenstein, Edward Smith, and David E. Pritchard, *Photon scattering from atoms in an atom interferometer: Coherence lost and regained*, Phys. Rev. Lett. **75** (1995), 3783–3787. [2](#)
- [Chu2008] Eleanor Chu, *Discrete and continuous Fourier transforms*, 1st ed., Chapman and Hall/CRC, March 2008. [117](#)
- [COK⁺1989] A. Cimmino, G. I. Opat, A. G. Klein, H. Kaiser, S. A. Werner, M. Arif, and R. Clothier, *Observation of the topological Aharonov-Casher phase shift by neutron interferometry*, Phys. Rev. Lett. **63** (1989), 380–383. [2](#)
- [COW1975] R. Colella, A. W. Overhauser, and S. A. Werner, *Observation of gravitationally induced quantum interference*, Phys. Rev. Lett. **34** (1975), 1472–1474. [2](#)
- [CTDRG1997] C. Cohen-Tannoudji, J. Dupont-Roc, and G. Grynberg, *Photons and Atoms*, 1st ed., Wiley and Sons, February 1997. [55](#)
- [DG1927] C. Davisson and L. H. Germer, *Diffraction of electrons by a crystal of nickel*, Phys. Rev. **30** (1927), 705–740. [1](#)
- [Dir1928] P. A. M. Dirac, *The quantum theory of the electron*, Proceedings of the Royal Society of London. Series A **117** (1928), no. 778, 610–624. [6](#)
- [FGRG1996] J. Felber, R. Gähler, C. Rausch, and R. Golub, *Matter waves at a vibrating surface: Transition from quantum-mechanical to classical behavior*, Phys. Rev. A **53** (1996), 319–328. [2](#)
- [FHS2010] Richard P. Feynman, Albert R. Hibbs, and Daniel F. Styer, *Quantum mechanics and path integrals*, emended edition 2005 ed., Dover Publications, 2010. [68](#)
- [GGK1994] R. Golub, R. Gähler, and T. Keller, *A plane wave approach to particle beam magnetic resonance*, American Journal of Physics **62** (1994), 779–788. [10](#)

- [Gla1959] R. J. Glauber, *High-energy collision theory*, Lectures in Theoretical Physics, vol. 1, Wiley-Interscience, New York, 1959. [68](#)
- [Gla1963] Roy J. Glauber, *Coherent and incoherent states of the radiation field*, Phys. Rev. **131** (1963), 2766–2788. [61](#)
- [HLB⁺2003] Y. Hasegawa, R. Loidl, G. Badurek, M. Baron, and H. Rauch, *Violation of a Bell-like inequality in single-neutron interferometry*, Nature (London) **425** (2003), 45. [78](#)
- [Hor2009] K. Hornberger, *Introduction to decoherence theory*, Lect. Notes Phys. **768** (2009), 221–276. [77](#)
- [HR1982] D. L. Haavig and R. Reifenberger, *Dynamic transmission and reflection phenomena for a time-dependent rectangular potential*, Phys. Rev. B **26** (1982), 6408–6420. [5](#)
- [HR2006] S. Haroche and J.M. Raimond, *Exploring the quantum*, Oxford University Press, Oxford, 2006. [61](#), [65](#)
- [HUB⁺2003] Klaus Hornberger, Stefan Uttenthaler, Björn Brezger, Lucia Hackermüller, Markus Arndt, and Anton Zeilinger, *Collisional decoherence observed in matter wave interferometry*, Phys. Rev. Lett. **90** (2003), 160401. [2](#)
- [JC1963] E T. Jaynes and F W. Cummings, *Comparison of quantum and semi-classical radiation theories with application to the beam maser*, Proc. IEEE **51** (1963), 89. [5](#)
- [JWR1994] D. L. Jacobson, S. A. Werner, and H. Rauch, *Spectral modulation and squeezing at high-order neutron interferences*, Phys. Rev. A **49** (1994), 3196–3200. [90](#)
- [JZK⁺2003] E. Joos, H. D. Zeh, C. Kiefer, D. Giulini, J. Kupsch, and I.-O. Stamatescu, *Decoherence and the appearance of a classical world in quantum theory*, 2nd ed., Springer, Berlin, 2003. [2](#)
- [Kle2006] H. Kleinert, *Path integrals in quantum mechanics, statistics, polymer physics, and financial markets*, 4th ed., World Scientific, Singapore, 2006. [68](#)
- [Kro1965] N. M. Kroll, *Quantum theory of radiation*, Quantum Optics and Electronics (Les Houches 1964) (C. de Witt, A. Blandin, and C. Cohen-Tannoudji, eds.), Gordon and Breach, New York, 1965, p. 1. [55](#)

BIBLIOGRAPHY

- [Lou2000] Rodney Loudon, *The quantum theory of light*, 3rd ed., Oxford University Press, 2000. [63](#)
- [Mac1892] Ludwig Mach, *Über einen Interferenzrefraktor*, Zeitschrift für Instrumentenkunde **12** (1892), 89-93. [1](#)
- [MJ1959] G. Möllenstedt and C. Jönsson, *Elektronen-Mehrfachinterferenzen an regelmässig hergestellten Feinspalten*, Z. Phys. **155** (1959), 472–474. [1](#)
- [NC2004] M. Nielsen and I. Chuang, *Quantum computation and quantum information*, 1 ed., Cambridge University Press, January 2004. [72](#)
- [Pau1927] Wolfgang Pauli, *Zur Quantenmechanik des magnetischen Elektrons*, Zeitschrift für Physik **43** (1927), 601–623. [6](#)
- [PCT1965] N. Polonsky and C. Cohen-Tannoudji, *Interprétation quantique de la modulation de fréquence*, Journal de Physique **26** (1965), no. 7, 409. [56](#), [63](#)
- [Rau1995] H. Rauch, *Towards interferometric Fourier spectroscopy*, Physica B: Condensed Matter **213-214** (1995), 830 – 832. [91](#)
- [RP1978] H. Rauch and D. Petrascheck, *Dynamical neutron diffraction and its application*, Neutron Diffraction, Springer-Verlag: Berlin Heidelberg New York, 1978, p. 303. [1](#), [77](#)
- [RSP1999] H. Rauch, M. Suda, and S. Pascazio, *Decoherence, dephasing and depolarization*, Physica B: Condensed Matter **267-268** (1999), 277 – 284. [94](#)
- [RTB1974] H. Rauch, W. Treimer, and U. Bonse, *Test of a single crystal neutron interferometer*, Phys. Lett. A **47** (1974), 369 – 371. [1](#), [2](#)
- [RZB⁺1975] H. Rauch, A. Zeilinger, G. Badurek, A. Wilfing, W. Bauspiess, and U. Bonse, *Verification of coherent spinor rotation of fermions*, Phys. Lett. A **54** (1975), 425. [2](#), [12](#)
- [SAI1990] Ady Stern, Yakir Aharonov, and Yoseph Imry, *Phase uncertainty and loss of interference: A general picture*, Phys. Rev. A **41** (1990), 3436–3448. [2](#), [90](#)
- [Sea1989] V. Sears, *Neutron optics: An introduction to the theory of neutron optical phenomena and their applications*, Oxford University Press, 1989. [77](#)

- [SH2007] Peter Sonnentag and Franz Hasselbach, *Measurement of decoherence of electron waves and visualization of the quantum-classical transition*, Phys. Rev. Lett. **98** (2007), 200402. [2](#)
- [SHK⁺1995] J. Summhammer, K. A. Hamacher, H. Kaiser, H. Weinfurter, D. L. Jacobson, and S. A. Werner, *Multiphoton exchange amplitudes observed by neutron interferometry*, Phys. Rev. Lett. **75** (1995), 3206–3209. [2](#), [5](#), [26](#), [33](#), [55](#)
- [SHK⁺2010] G. Sulyok, Y. Hasegawa, J. Klepp, H. Lemmel, and H. Rauch, *Noise-induced dephasing in neutron interferometry*, Phys. Rev. A **81** (2010), 053609. [3](#)
- [SPE⁺2000] Erik Sjöqvist, Arun K. Pati, Artur Ekert, Jeeva S. Anandan, Marie Ericsson, Daniel K. L. Oi, and Vlatko Vedral, *Geometric phases for mixed states in interferometry*, Phys. Rev. Lett. **85** (2000), 2845–2849. [78](#)
- [Sud2001] M. Suda, *Simulating Decoherence of Neutron Wave Packets in Magnetic Fields*, Fortschritte der Physik **49** (2001), 1103–1108. [9](#)
- [Sud2005] Martin Suda, *Quantum interferometry in phase space: Theory and applications*, 1st ed., Springer, Berlin, Heidelberg, 2005. [91](#)
- [Sum1993] Johann Summhammer, *Coherent multiphoton exchange between a neutron and an oscillating magnetic field*, Phys. Rev. A **47** (1993), 556–565. [2](#), [5](#), [55](#)
- [WBRs1988] H. Weinfurter, G. Badurek, H. Rauch, and D. Schwahn, *Inelastic action of a gradient radio-frequency neutron spin flipper*, Zeitschrift für Physik B Condensed Matter **72** (1988), 195–201. [5](#)
- [Wig1932] E. Wigner, *On the quantum correction for thermodynamic equilibrium*, Phys. Rev. **40** (1932), 749–759. [91](#)
- [WM1985] D. F. Walls and G. J. Milburn, *Effect of dissipation on quantum coherence*, Phys. Rev. A **31** (1985), 2403–2408. [90](#)
- [YMK1986] Bernard Yurke, Samuel L. McCall, and John R. Klauder, *SU(2) and SU(1,1) interferometers*, Phys. Rev. A **33** (1986), 4033–4054. [77](#)
- [Zeh1891] Ludwig Zehnder, *Ein neuer Interferenzrefraktor*, Zeitschrift für Instrumentenkunde **11** (1891), 275–285. [1](#)

BIBLIOGRAPHY

- [Zur1991] Wojciech H. Zurek, *Decoherence and the transition from quantum to classical*, *Physics Today* **44** (1991), 36–44. [2](#), [90](#), [94](#)
- [Zur2003] Wojciech H. Zurek, *Decoherence, einselection, and the quantum origins of the classical*, *Rev. Mod. Phys.* **75** (2003), 715–775. [2](#)